UNIVERSITY OF CALIFORNIA

Santa Barbara

Fundamental characterization of donor-acceptor Stenhouse adducts in photoactive polymers towards applications in soft photoactuation

A dissertation submitted in partial satisfaction of the

requirements for the degree Doctor of Philosophy

in Chemical Engineering

by

Sara Sandlass

Committee in charge:

Professor Michael Gordon, Chair

Professor Javier Read de Alaniz

Professor Phil Christopher

Professor Matt Helgeson

March 2025

The dissertation of Sara Sandlass is approved.

Professor Matt Helgeson

Professor Phil Christopher

Professor Javier Read de Alaniz

Professor Michael Gordon, Committee Chair

March 2025

Fundamental characterization of donor-acceptor Stenhouse adducts in photoactive polymers towards applications in soft photoactuation

by

Sara Sandlass

Acknowledgements

This work would not be possible without the constant support of my advisor, Professor Mike Gordon. Whether it's talking me off the cusp of a research-induced meltdown or covering for me when I lose track of time and forget to go to my mechatronics TA office hours, Mike has always been by my side. Of course, I can't neglect to acknowledge my unofficial co-advisor, Professor Javier Read de Alaniz, for volunteering his time and the time of his students to help me by providing a never-ending supply of DASA and making an effort to include me in the Read de Alaniz Lab. Thank you as well to the rest of the professors and students on the EFRI C3 Soft Robotics team for their technical advice and for providing laboratory supplies when 2-day shipping is too long to wait. The research funding provided primarily by the National Science Foundation's Emerging Frontiers in Research and Innovation has been instrumental in bringing this amazing team of researchers together and supporting our endeavors in soft robotics. With the current political uncertainty regarding the future of similar pioneering research grants, I hope many more generations of dedicated students and professors can experience the same level of support that we were fortunate enough to receive.

I would also like to acknowledge the fellow graduate students (now mostly alumni) that I have had the opportunity to collaborate with over the years, specifically Dr. Fritz Stricker, Professor Julie Peterson, Dr. Michèle Clerc, and Jesus Guillen Campos for their advice and mentorship on all things DASA-related. Thank you as well to my undergraduate mentees, Daniel Fragoso and AJ Jayaraman, for the time and energy they spent working on experiments that worked a little less often than I'm sure they or I would have liked them to.

For the many (many) hours he spent discussing everything from DASA to 3-D printing with me, I'm not sure this dissertation would have been completed without the support of my labmate, housemate, and friend, Visoth Lim. He's always willing to give 110% of his effort and

attention when assisting anyone coming to him for help and there are days when I'm convinced that the Gordon lab might not be functioning if Visoth wasn't there.

Finally, I owe a word of appreciation to the friends and family that have supported me outside of the lab. Specifically, fellow graduate student Cassidy Tobin for being the sister I didn't meet until my 20s. Moving across the country during the peak of a global pandemic was not easy, but Cassidy made the months spent in social isolation a period that I now look back on with fondness. Thank you as well to my two other wonderful housemates, Devon Callan and Shawn Mengel, for always being able to make me laugh. Of course, I can't forget my parents, Amy and Brian, and grandparents for constantly encouraging me to shoot for the stars even when they don't fully understand what I'm aiming for.

Curriculum Vitae

Sara Sandlass

Education

Ph.D. in Chemical Engineering — *March 2025*
University of California, Santa Barbara

Bachelor of Chemical Engineering — *May 2020*
University of Minnesota, Twin Cities

Bachelor of Science, Chemistry — *May 2020*
University of Minnesota, Twin Cities

Professional Experience

Senior Research Engineer — *April 2025*
3M (Maplewood, MN)

R&D Graduate Intern — *Summer 2024*
3M (Maplewood, MN)

R&D Intern — *Summer 2019*
Bostik, Inc. (Wauwatosa, WI)

Publications

(submitted) J. Guillen Campos, C. Tobin, **S. Sandlass**, *et al.*, "Synthesis of Photoresponsive Liquid Crystal Elastomers: A General Chemical Approach," *J. Mater. Chem. A*. (2025)

S. Sandlass and M.J. Gordon, "Design and dynamic characterization of a phototunable optofluidic lens," *Opt. Express* **32***(15)*, 26445 (2024).

J. Guillen Campos, C. Tobin, **S. Sandlass**, *et al.*, "Photoactivation of Millimeters Thick Liquid Crystal Elastomers with Broadband Visible Light Using Donor–Acceptor Stenhouse Adducts," *Adv. Mat.* **2024**, 2404932.

M. Clerc, **S. Sandlass,** *et al.*, "Visible light-responsive materials: the (photo)chemistry and applications of donor-acceptor Stenhouse adducts in polymer science," *Chem. Soc. Rev.* **52**, 8245-8294 (2023)**.**

S. Sandlass, *et al*, "Effect of polymer host matrix on multi-stage isomerization kinetics of DASA photochromes," *J. Photochem. Photobio., A: Chem.* **444**, 114964 (2023).

F. Stricker, J. Peterson, **S. Sandlass**, *et al.*, "Selective control of donor-acceptor Stenhouse adduction populations using non-selective stimuli'" *Chem*. **9**(7), 1994-2005 (2023).

W. Nunn, **S. Sandlass**, *et al.*, "Hybrid Molecular Beam Epitaxy Growth of $BaTiO_3$ Films," *J. Vacuum Sc. & Tech. A* **39**, 040404 (2021).

Presentations

UCSB ChE Graduate Student Symposium (presentation) *September 2024*
Title: Leveraging the interdependence of light, heat, and force in photoactive soft materials for photomechanical sensing and actuation

3rd International Forum on Energy & Informatics *December 2023*
Title: Analyzing the Isomerization Kinetics of DASA Photochromes in Polymers for Applications in Soft Photoactuation

UCSB ChE Graduate Student Symposium (poster) *September 2023*
Title: Unique Three State Isomerization Kinetics of DASA Photochromes in Polymers

UCSB ChE First Year Graduate Student Symposium (presentation) *September 2021*
Title: Measuring Photomechanical Response in Soft Actuators Using Harmonic Oscillator Dynamics

Emerging Frontiers in Research and Innovation (EFRI) Workshop (poster) *August 2021*

Abbreviations

DASA	Donor-acceptor Stenhouse adduct (photoswitch)
A/B/B'/C	DASA isomers with different triene backbone conformations (*EEZ/EEE/EZE/closed)*
DASA 1/2/3	DASA based on the generation 1, 2, or 3 architectures
MC	Merocyanine (photoswitch)
SP	Spiropyran (photoswitch)
DAE	Diarylethene (photoswitch)
PDMS	Poly(dimethyl siloxane)
PU	Polyurethane
PMA	Poly(methyl acrylate)
PMMA	Poly(methyl methacrylate)
PEMA	Poly(ethyl methacrylate)
PBMA	Poly(butyl methacrylate)
PHMA	Poly(hexyl methacrylate)
LCE/LCP/LCN	Liquid crystal elastomer/polymer/network (analogous)
PES	Potential energy surface
CI	Conical intersection
PSS	Photostationary state
PTSS	Photothermal stationary state
DFT	Density functional theory
COGEF	Constrained geometries simulate external force
FMPPS	Frequency modulated pump probe spectroscopy
PD	Photodiode
PRM	Photoresponsive molecule

Abstract

Fundamental characterization of donor-acceptor Stenhouse adducts in photoactive polymers towards applications in soft photoactuation

by

Sara Sandlass

Polymeric materials that display photoresponsive properties are at the core of many diverse research fields, including optical sensing, photoactuation, photopharmacology, optical data storage/transmission, and surface/interface engineering. To synthesize these “smart” materials, a polymer host is embedded with a photosensitizing agent that absorbs the incident radiation and converts this energy into a combination of thermal and chemical bond energy through nonradiative relaxation to drive a change in the chemical or physical properties of the chromophore/polymer system. Organic photoswitches are a class of chromophores that are well suited for this particular application because they undergo reversible absorption-induced isomerization, resulting in conformational changes that can be leveraged into macroscopic structural responses when exposed to light.

Donor-acceptor Stenhouse adducts, or DASAs, are a class of organic photoswitches that are ideal for photoactive material applications because they are visible light active ($\varepsilon_{\lambda max}$ ~ 100,000 $M^{-1}cm^{-1}$), become transparent when irradiated (i.e., negatively photochromic), are kinetically and optically tunable through facile synthetic modifications, and can respond to multiple orthogonal stimuli simultaneously including light, heat, polarity, pH, hydration, ionic strength, and stress. These unique stimuli responsive properties arise from the mechanism of DASA photoswitching, which proceeds through an initial actinic (photochemical) step, followed by a series of thermal isomerizations occurring on the ground state potential energy surface (PES). This ground state PES is highly susceptible to the influence of external stimuli and to

interactions between DASA and the host polymer, presenting both an opportunity for enhanced functionality and a fundamental challenge to characterize and control.

This work addresses the challenge of designing and implementing photoactive polymers from both a fundamental and applied perspective. The fundamental exploration focuses primarily on quantifying how polarizing and viscosity-driven environmental interactions shape the photoswitching kinetics and optical properties of DASA in polymers by leveraging a range of spectroscopic techniques. A novel optical technique called frequency modulated pump probe spectroscopy, or FMPPS, was developed in this work and combined with UV-Vis and polarized light absorption spectroscopy to measure dynamic processes such as photoswitching and stress-induced chromophore alignment. These improvements make it possible to measure the environmental sensitivity of the metastable intermediate isomer of DASA, even though this species is often too unstable to accumulate in concentrations detectable by standard methods (< 0.05 a.u.). Zooming out from the molecular level to the macroscopic scale, this work concludes by demonstrating two different applications in light powered actuation for photoresponsive polymers that are relatively simple in their chemical makeup, the first being a photothermally actuated fluid lens and the second being a DASA-based photothermally actuated bilayer cantilever. These examples aim to demonstrate that while molecular level fundamental insights are valuable for designing novel photoresponsive materials, engineering optimization is responsible for taking these materials from conceptual to functional.

Table of Contents

Chapter 1

The photochemistry of donor-acceptor Stenhouse adducts and applications in photoactive functional materials

Adapted from the following publication:

1. Clerc, M.; Sandlass, S.; Rifaie-Graham, O.; Peterson, J.A.; Bruns, N.; Read de Alaniz, J.; Boesel, L.F., *Chem. Soc. Rev.*, **52**, 8245-8294 (2023).

1.1. Photoactive functional materials powered by organic photoswitches

Polymeric materials that exhibit stimuli responsive changes in their physical or chemical properties are at the core of research endeavors in soft actuation[2,3], sensing, triggerable molecule release for pharmacology[4] and reaction engineering, data storage/transmission [5], and engineered surface/interface chemistry[3]. These “smart” materials have been synthesized to respond to various stimuli including mechanical stress, heat, pH, adsorption of small molecules, and electric/magnetic fields. One stimulus of particular interest is light because it is ubiquitous in nature, readily generated with modern laser/LED technologies, and offers spatiotemporal resolution in wavelength, intensity, polarization, etc. down to the diffraction limit. In addition, optical signals can be transmitted virtually instantaneously (relative to the material response time) over expansive distances with minimal attenuation and are considered a largely noninvasive stimulus from roughly 650 to 900 nm for controlling biological processes using photoactive therapeutics [6].

To synthesize photoactive functional materials, a polymer host is embedded with a photosensitizing agent, typically an organic chromophore, that absorbs the incident radiation, is excited to a higher energy electronic state, and subsequently relaxes back to the ground state through a combination of radiative and nonradiative processes. During nonradiative relaxation, energy from the absorbed photons is converted into a combination of thermal and chemical bond energy to drive a change in the chemical or physical properties of the chromophore/polymer system. The type of material response depends on the nature of the chromophore and host polymer as well as forces arising from their interaction, and may include a change in electronic properties [7,8], membrane permeability[9,10], optical properties, phase[11], crystal order parameter, surface energy[12–14], mechanical properties[15,16], and/or strain state[3].

Organic photoswitches are a class of organic chromophores that are uniquely well suited for photoresponsive material applications because, unlike traditional, non-isomerizing chromophores, they undergo reversible absorption-induced conformational changes, including E/Z isomerization and/or decyclization, that can be leveraged into macroscopic structural responses. The most common organic photoswitches used in photoresponsive polymers include azobenzene, spiropyran/merocyanine (SP/MC), diarylethene (DAE), hydrazone, and donor-acceptor Stenhouse adducts (DASA), and each has a different isomerization mechanism, absorbance wavelength (Fig. 1.1), dipole strength, hydrogen bonding affinity, chemical compatibility, and synthetic tunability. These unique characteristics determine how the photoswitch interacts with its environment to enable different stimuli responsive properties. For example, the dipole moment of SP increases by approximately 8-15 Debye upon photoisomerization to MC[17,18] and enables applications in photoactuation[19,20], photocontrolled (de)-wetting/adhesion[13,21,22], and photoinduced transport of small molecule/ions[23]. Conversely, cis-trans isomerization of azobenzene is associated with a significant (39%[24]) increase in the end-to-end length of the molecule, thereby facilitating photocontrol over the structure/function of azo-functionalized biomolecules, photoactuation of azo-functionalized liquid crystal elastomers (LCEs/LCPs/LCNs)[25–27], and mechanochromism of azobenzene in polymers[28].

Photoswitches are often susceptible to interacting with other orthogonal stimuli that couple to the photoswitch potential energy surface (PES) including mechanical stress, heat, polarity, and pH. By leveraging these interactions, stimuli responsive materials are possible that expand beyond linear logic to mimic the highly selective ways that nature uses to regulate biological processes. For example, researchers in the Sottos lab at the University of Illinois found that the application of tensile strain across a bulk polyurethane (PU) film conjugated to a MC photoswitch resulted in a slower rate of photochemical isomerization from fluorescent

merocyanine (MC) to colorless SP under irradiation. [29] Alternatively, Dong et al. embedded a multi-responsive dye called DASA (donor-acceptor Stenhouse adduct) in a polymer gel and subjected the material to a sequence of light, heat, and water stimuli that interacted with the dye to reveal an encrypted message only when the stimuli were introduced in the correct order. [30] A different example of multi-responsive DASA isomerization was demonstrated by Wang et al. by replacing the donor group of DASA with a crown ether to promote orthogonal, reversible isomerization pathways to the cyclic, non-absorbing enolate and keto isomers of DASA when exposed to light/heat and crown ethers/metal ions, respectively.[31]

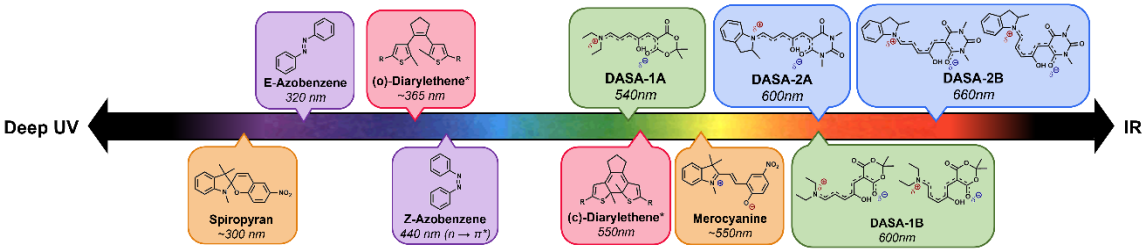

Fig. 1.1. Absorbances of selected common organic photoswitches. Color is used to indicate photoisomers of the same molecule.

1.2. Mechanistic description of photoswitching

Depending on the type of photoswitch, the complete photoswitching mechanism may consist of a single actinic (i.e. photochemically activated) step or a sequence of elementary steps initiated by an initial actinic step and proceeded by a combination of thermal and/or photochemical isomerizations. Mechanistically, photoisomerization is unique from thermal isomerization because the former is described in the context of a conical intersection instead of a vibrational energy barrier. The conical intersection is a point of degeneracy between the S_1 excited state potential energy surface (PES) and the S_0 ground state PES (Fig. 1.2) defined within the space of the molecule's internal coordinate (**q**). When the excited state isomer passes through the conical intersection (CI), energy from the absorbed photons is converted into nuclear kinetic energy that is concentrated in one or more vibrational modes for a short time before redistributing throughout the molecule. This is called vibronic coupling and allows

the molecule to explore configurations that may be otherwise thermally inaccessible, including those requiring bond scission or isomerization about a bond with significant π character (E/Z isomerization). The likelihood of the molecule sampling a productive configuration that yields a distinct stable or metastable isomer following photoexcitation (green pathway in Fig. 1.2) is reflected in the photochemical quantum efficiency.

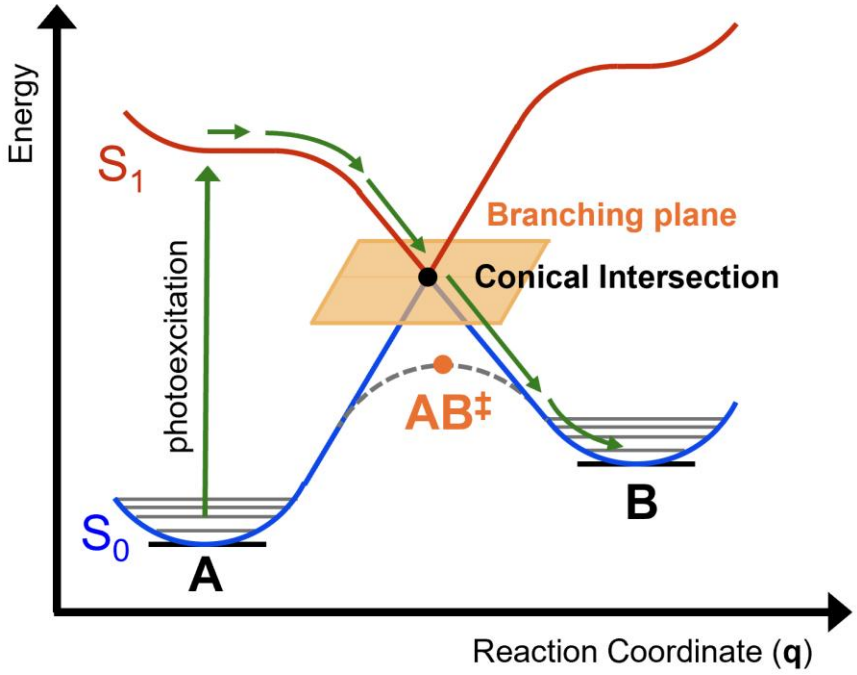

Fig. 1.2. Conical Intersection in organic photochemistry. Upon photoexcitation, isomer **A** is promoted to the excited state PES, S_1, from the ground state PES, S_0. During relaxation, **A** passes through the conical intersection where it can either return to vibrationally excited **A** or isomerize to form **B**. The branching plane is the subspace of **q** that contains the intersection and reflects the nuclear coordinates about the intersection.

The process of photoisomerization necessarily results in a change in the absorption spectra of the molecule (photochromism) that can be observed by eye or with the use of UV-Vis spectroscopy. When the peak absorbance wavelength shifts to shorter wavelengths after irradiation, photoswitching is negatively photochromic. When the peak absorbance wavelength shifts to longer wavelengths after irradiation, the photoswitch is positively

photochromic. Subsequent thermal isomerizations may result in the peak absorbance wavelength shifting again before the final, thermally stable photoproduct isomer is generated. In this case, the photoswitch's chromism is typically defined by the net change in absorbance between the initial and final state after complete isomerization. Positive photochromism is more common and is observed in spiropyran (SP), azobenzene, and hydrazone photoswitches. Negatively photochromic photoswitches include indigos, DASAs, and Stenhouse salts (a close relative of DASA).

The conical intersection typically also provides a route through which the photoproduct can photochemically revert back to the thermodynamically favored isomer. However, the thermal energy barrier is often lower in the reverse process and may be accessible in the ground state under experimental conditions for certain photoswitches. When this is the case, the photoswitch is classified as P/T-type reversible. Examples of P/T-type photoswitches include some azobenzenes, SPs, and hydrazones. Photoswitches that do not have an energetically accessible reverse isomerization pathway in the ground state are classified as P-type reversible and include stilbenes, diarylethenes, and thiophenefulgides. Photoswitches that are strictly thermally reversible are called T-type photoswitches and include DASAs and Stenhouse salts. When the forward and reverse isomerizations occur simultaneously under irradiation, photoswitching occurs until an equilibrium state is attained, the photostationary state (PSS). When this equilibrium is temperature dependent, it is referred to as the photothermal stationary state (PTSS).

This mechanistic description for photochemical isomerization fails to provide a basis for quantum yields that are wavelength dependent because Kasha's rule dictates that all molecules must luminesce or photoisomerize from the lowest energy excited state. As a result, the wavelength of light used to promote the transition should have no correlation with the efficiency of the subsequent quantum event because vibrational relaxation occurs prior to

isomerization or luminescence. If a dependence on wavelength is observed, it is likely the result of multiple competing electronic transitions with similar excitation energies or may indicate intersystem crossing to the triplet state, where the efficiency of this process is a function of vibrational level of the excited state molecule.[32] Wavelength dependent quantum yields have been reported for a number of photochemical reactions, but the underlying basis is often unclear. [33]

1.3. Donor Acceptor Stenhouse adducts (DASAs)

Donor-Acceptor Stenhouse Adducts, or DASAs (see Fig. 1.3), are a class of organic photoswitches that are especially well suited to applications in stimuli responsive materials because they are visible light active ($\varepsilon_{\lambda max}$ ~ 100,000 $M^{-1}cm^{-1}$)[34], negatively photochromic, kinetically and optically tunable through facile synthetic modifications, and respond to multiple orthogonal stimuli simultaneously including light, heat, polarity[35], pH[36], hydration[30,37], ionic strength[38], and stress[39–41]. Discovered in 2014 by the Read de Alaniz group at UCSB, DASA was originally based on either a barbituric or Meldrum's acid activated furan acceptor and an alkylamine donor and offered minimal synthetic control over the primary absorbance wavelength and could only switch in nonpolar solvents like toluene.[34]

The second generation of DASA was introduced in 2016 and replaced the alkylamine donor with various aniline derivatives to tune the peak absorbance wavelength between 582 nm and 669 nm. Unlike the first generation of DASA, the second generation provided enhanced solvent compatibility, switching in both polar and nonpolar solvents, and was reversibly switchable

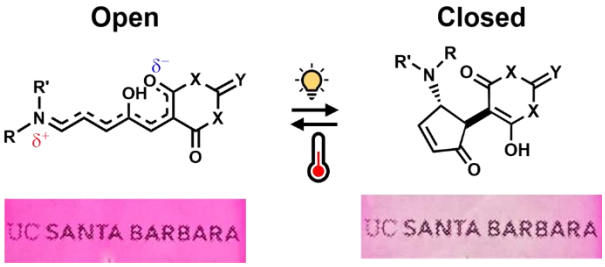

Fig. 1.3. Under irradiation, DASA isomerizes from a brightly colored open conformation to a non-absorbing closed form. Isomerization back to the open form occurs thermally in the dark.

when blended into poly(methyl methacrylate) (PMMA), poly(ethyl methacrylate) (PEMA), and poly(butyl methacrylate) (PBMA)[39]. However, the percentage of open (**A**) form DASA at equilibrium in the dark was low, ranging between 2% and 70% in dichloromethane for the different aniline donor derivatives.[42] This motivated the development of a third generation of DASA based on a carbon acid acceptor instead of Meldrum's or barbituric acid, which retained the wavelength tunability and solvent/polymer compatibility of the second-generation while improving the dark equilibrium to between 75% and > 95% of the open triene (**A**) form. In addition, open form thermal recovery in solution was much faster for third generation DASA, dropping from several hours to minutes or less.[43]

Accessing DASA photoswitching in polymers is crucial for the design of stimuli responsive materials for applications requiring spatial resolution (photopatterning, chemo- and temperature sensing), mechanical robustness (soft actuation), and activation in protic solvents, like water, where the **A** isomer is typically thermally unstable, resulting in irreversible photoswitching unless DASA is encapsulated in lipid lysosomes[44,45], polymer micelles[46], or vesicles[47].

1.3.1. Mechanism of DASA photoswitching

Unlike photoswitches like azobenzene and stilbene that isomerize in a single concerted step, DASA photoswitching from the thermodynamically favored, absorbing isomer (**A**) to a set of non-absorbing, closed form isomers (**C**) proceeds through an initial actinic E/Z isomerization followed by a series of thermal isomerizations. Primarily in the case of first generation DASAs, the thermal ring closing step to generate the closed form isomers is strongly rate limiting and allows for the accumulation of two intermediate metastable photoproduct isomers (**B** and **B'**). While these intermediates are spectroscopically

indistinguishable from one another in the visible regime, they appear as a 50 nm red shifted hump off of the primary absorption peak of **A** (see Fig. 1.4).

A few years after the initial discovery of DASA, di Donato et al. observed that the irradiation of **B/B'** at low temperatures (233 K) results in photochemical isomerization back to **A**.[48] Several years later, Stricker et al. leveraged this photochemical reversion pathway to control the rate of **B/B'** to **C** photoswitching by modulating the relative intensities of two light sources, one addressing **A** and the other targeting **B/B'**. To avoid the need for low temperatures to increase the thermal lifetime of **B/B'**, Stricker et al. used targeted steric modifications to stabilize **B/B'** and allow these intermediates to accumulate during photoswitching in high enough concentrations to be addressable photochemically.[49] The mechanism of DASA photoswitching is illustrated schematically in Fig. 1.5.

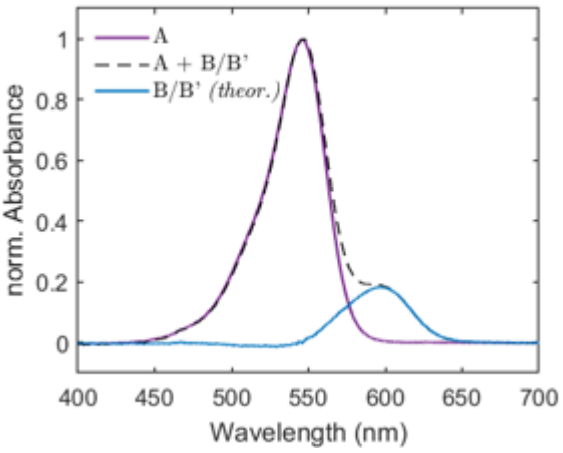

Fig. 1.4. Absorbance profiles for **A** (purple) and theoretical **B/B'** (blue) DASA isomers in toluene. **B/B'** absorbance estimated by subtracting purple curve from dashed curve measured after irradiation of **A** for 5 sec.

In addition to intramolecular sterics, intermolecular interactions have a significant impact on the PES of DASA. For example, polar protic solvents (e.g., water, methanol) are known to result in irreversible switching from **A** to **C** by disrupting the hydrogen bonding between the triene backbone hydroxyl and the carbonyl of the acceptor.[30,37,50] Viscosity, e.g., in polymers, also affects the energetics of DASA isomerization, slowing the rates of photoswitching and thermal recovery.[39,41,51] To design DASA-based materials that display optimal switching kinetics within a particular environment, it is crucial to understand how the

structure of DASA and the chemical/mechanical properties of the host environment serve to disrupt or promote individual steps within the complex photoswitching pathway.

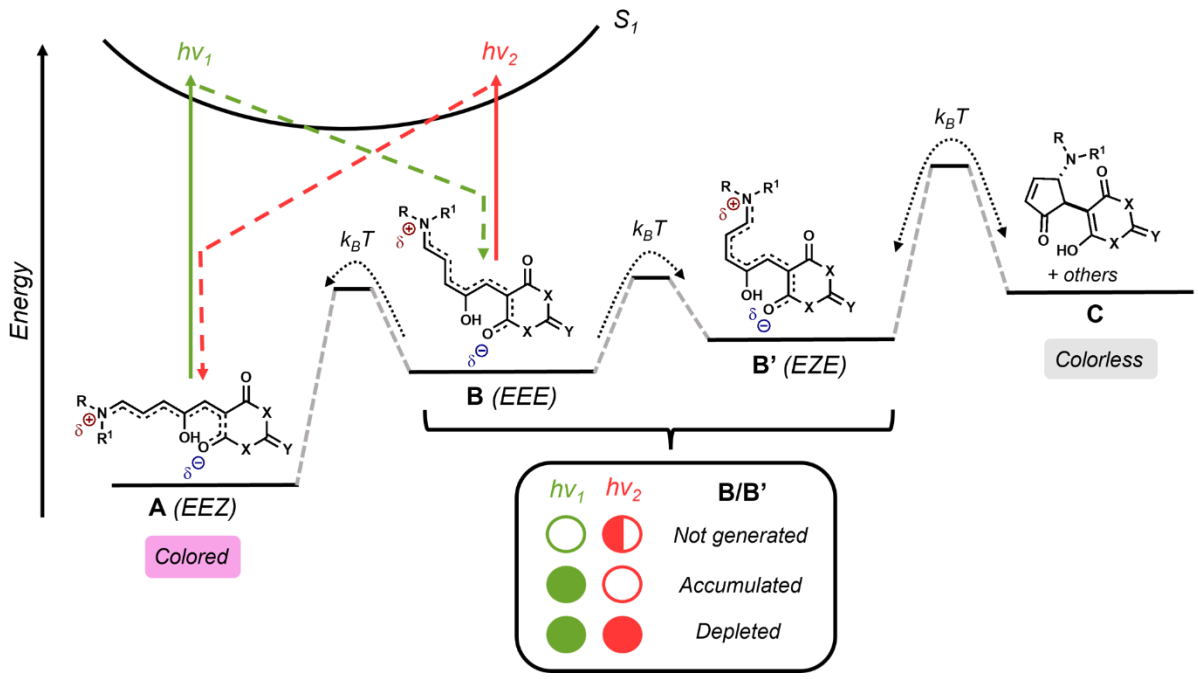

Fig. 1.5. Mechanism of DASA photoisomerization showing the effect of dual wavelength irradiation of **A** and **B**. When the green light is off, B/B' is not generated. When the green light is on and the red light is off, **B/B'** accumulates and proceeds thermally to **B'** and **C**. When the red and green lights are both on, **B/B'** rapidly reforms **A** photochemically instead of isomerizing to **B'**. Bond orientations (*E* vs. *Z*) within the conjugated system are included to distinguish the relevant isomers. Reproduced with permission from ref. 52.

While various experimental and computational studies have helped to provide insight into the mechanism and sensitivity of DASA photoswitching, the vastly different time scales for the actinic (ps) and thermal isomerizations (ms to hours), combined with the inability to observe closed form isomers using visible light spectroscopy, make it impossible to resolve the entire photoswitching process with a single technique. To understand DASA photoswitching in its entirety, different techniques are used to study different subsets of the photoswitching process, and the results are stitched together to construct a comprehensive description of photoswitching. For example, ultrafast pump-probe UV-Vis absorption spectroscopy is used to study the rapid photochemical isomerizations of **A** and **B** because the

time resolution of this technique (~ ps) allows these steps to be temporally isolated from the slower thermal isomerizations.[48,51,53] Conversely, FTIR spectroscopy is well suited to measuring thermal isomerizations between the different closed form isomers contained in **C** because these isomers have no absorbance in the UV-Vis spectral region and they isomerize on a time scale that is compatible with the scan rate of FTIR (~ s).[51,54] Traditional pump probe UV-Vis absorbance spectroscopy is often used to measure the overall photoswitching and thermal recovery kinetics (assuming the molar absorptivity of **A** is known), but is difficult to perform passively, which is crucial measuring thermal isomerizations of photochemically active species.[49,51,53,55,56] Traditional UV-Vis may also be suitable for measuring the isomerization kinetics of **B/B'** in select systems that support a large enough **B/B'** population during photoswitching to exceed the resolution limit of the spectrophotometer.[49,51,53] Additional techniques that have helped to provide insight into the mechanism/structure of DASA include mass spectrometry[57], x-ray crystallography[34,35,38,56,58], and ^{1}H NMR[55,56,59]. Computational tools (DFT/TD-DFT[31,55,60], CASSCF[49,61,62], molecular dynamics[31,63,64]) have also been valuable in proposing likely isomerization mechanisms and providing theoretical explanations for experimental observations.

Despite the diversity of techniques available to study the isomerization kinetics of DASA, relatively few are suitable for studying DASA isomerization in polymers because the structural complexity of polymers makes it difficult to isolate the contribution of dilute DASA molecules from the baseline signal of the polymer matrix in FTIR and NMR. For this reason, time dependent UV-Vis spectroscopy has been used exclusively to experimentally study DASA photoswitching in solid polymer matrices, but may be complicated due to variabilities in surface quality and film thickness introduced during film processing, light scattering, thin film interference, and anisotropy introduced by the lack of diffusion in these media. In addition, it can be difficult to determine the exact molar absorptivity of **A** in polymers because this

calculation requires the ratio of **A** to **C** at thermal equilibrium, which is typically measured in solution using ^{1}H NMR. In glassy polymers, the thermal isomerization kinetics are exceptionally slow, making it difficult to attain a true equilibrium to perform this measurement. Furthermore, photoswitch functionalized liquid crystal elastomers (LCEs, also referred to as liquid crystal networks or polymers— LCNs or LCPs), which currently dominate the photoactuation field, make it particularly difficult to measure intrinsic photoisomerization kinetics because the photoswitch is confined anisotropically, resulting in photoswitching kinetics that depend on the polarization and incidence angle of light.[65]

Expanding the capabilities of various spectroscopic and analytical tools to be suitable over a broad range of concentrations, wavelengths, time scales, and sample types (solution vs. solid) is crucial to understanding the effects of various factors, both internal (DASA-DASA and DASA-host interactions) and external (light, heat, polarity, pH, mechanical stress), on the potential energy landscape of DASA. By leveraging these insights, the complexity and sensitivity of DASA can transform from an obstacle into an opportunity for enhancing its stimuli responsive properties and enabling multi-addressable reactivity.

1.3.2. Thermally sensitive DASA photochemistry

The thermal reversibility of DASA photoswitching and the non-absorbing nature of the photoproduct presents both a challenge and an opportunity for dynamically controlling the absorbance state of DASA using both light and heat. One such opportunity is as a molecular thermochromic sensor, which Mason and Whittaker demonstrated by embedding DASA in its closed, non-absorbing state in a polybutadiene rubber and subjecting the sample to a high shear impact event.[66] During impact, frictional heating resulted in a portion of the DASA molecules isomerizing to the absorbing state and the resulting absorbance profile was used to generate a map of the maximum temperature attained during impact (Fig. 1.6.a). In addition

to affecting the thermodynamics of DASA isomerization, heat has also been found to indirectly affect the kinetics of DASA isomerization by altering the mechanical properties of the host polymer. This effect is often significant in amorphous polymers when comparing the rates of photoswitching and thermal recovery above and below the parent polymer glass transition temperature (Fig. 1.6.b).[67]

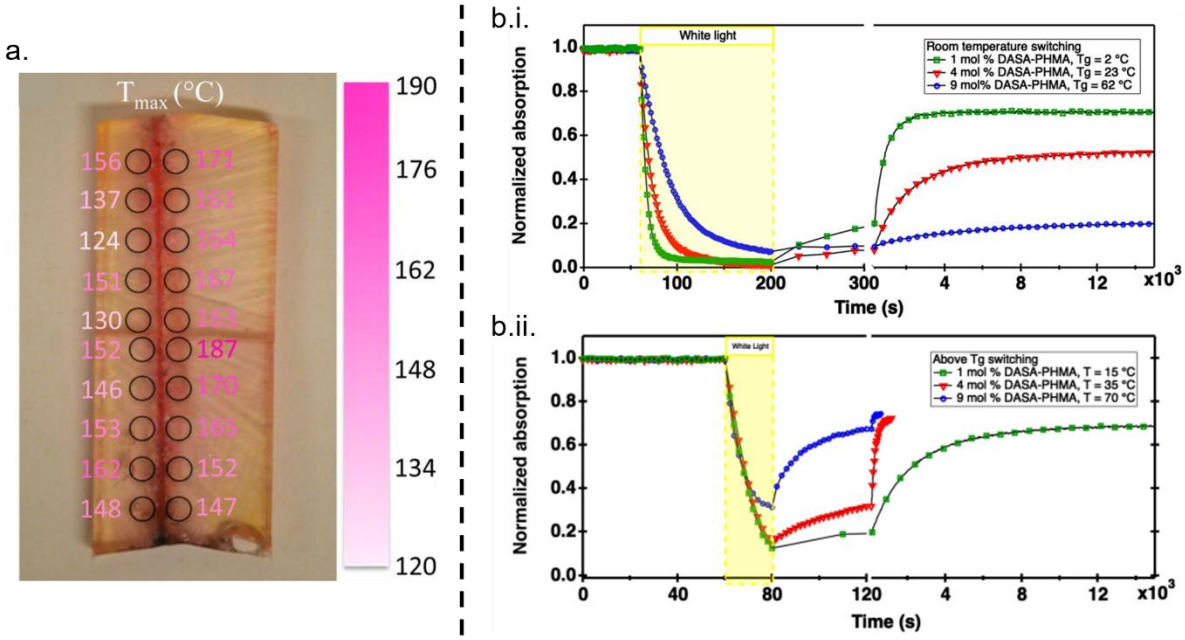

Fig. 1.6. (a) Temperature mapping from the thermally coloration of DASA in polybutadiene rubber following impact with a 30 cal. bullet. Adapted with permission from ref. 66. Copyright 2016 AIP Publishing. (b) Photoswitching and thermal recovery of DASA pendant conjugated to PHMA at room temperature (top, i) and above the host polymer glass transition temperature (bottom, ii). Below T_g, polymers with a higher glass transition temperature show slower photoswitching when irradiated with white light (175 mW/cm^2, yellow shaded). Above T_g, this matrix dependence in the rate of photoswitching goes away. In addition, heating above T_g results in faster thermal open form recovery. Adapted with permission from ref. 67. Copyright 2022 American Chemical Society.

Heat is also generated as a secondary stimulus when DASA is switched with higher light intensities due to photothermal heating. In theory, this phenomenon has the potential to introduce non-linearity in the rate of photoswitching as a function of light intensity but has not been observed in practice, likely because the material platforms that support the greatest amount of photothermal heating are also typically associated with the slowest thermal recovery kinetics (e.g., glassy polymers).

1.3.3. Mechanically sensitive DASA photochemistry

Under the effects of mechanical force, the conical intersection tilts if some component of applied force is nonzero in the subspace of **q** that contains the intersection, called the branching plane (see Fig. 1.2).[68] This tilting results in a change in the quantum efficiency of isomerization. In addition, the force modifies both the ground and excited state PES, shifting the ground state equilibrium geometry and the thermal barriers for isomerization.[68] When the applied mechanical force can be represented as a simple force pair applied across two different substitution positions, DFT calculations like COGEF (constrained geometries simulate external force) can be used to model the ground and excited state PES and estimate the mechanochemical reactivity of different molecules.[68] However, the mechanical forces experienced by isomerizing photoswitches in polymers are much more difficult to computationally model. As a result, experimental observations are required to provide the necessary insight into the effects of mechanical confinement on photoswitching.

During isomerization, DASA undergoes a significant change in molecular geometry. As a result, the quantum yield(s) and thermal isomerization rate constants of DASA are strongly influenced by mechanical confinement in viscous solvents and solid polymers. These non-polarizing forces impede the molecular motion necessary to create free volume and accommodate the spatial needs of isomerization. For example, Lerch et al. observed less efficient DASA **A** to **B** photoisomerization in DMSO and in a 60 % by volume mixture of glycerol in DMSO compared to methanol, which has a significantly lower viscosity but is chemically similar in its hydrogen bonding character and polarity.[51] Mechanical confinement effects also occur as a result of aggregation, where the strong dipole moment and conjugated nature of DASA encourage nearby molecules to stack together in a head to head (H aggregation) or heat to tail (J aggregation) configuration.

In addition to mechanical confinement forces arising spontaneously from DASA-DASA and DASA-host interactions, intentional confinement may be used as a way to encapsulate or stabilize DASA for a particular application. For example, using a metal organic framework (MOF) to encapsulate DASA has been shown to enable isomerization in the solid (powder) state and provide a method to functionalize PDMS with DASA by preventing DASA from being reduced by the platinum catalyst used to crosslink the PDMS.[69] Another study used supramolecular encapsulation of DASA to mechanically prevent cyclization to the non-absorbing closed form in aqueous environments.[70] A schematic overview of the different sources of mechanical confinement is provided in Fig. 1.7.

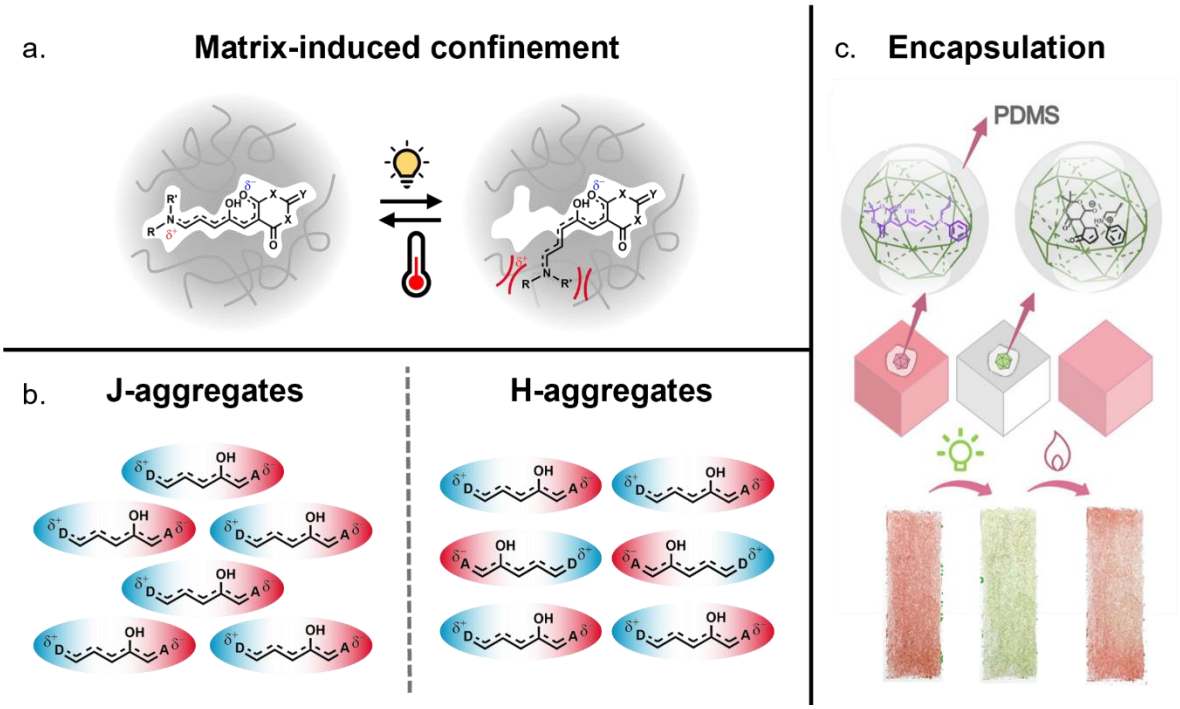

Fig. 1.7. Types of mechanical confinement in polymers. (a) Matrix-induced confinement arises from the limited mobility of polymer chains in the immediate vicinity of the photoswitch. (b) Aggregation of photoswitches occurring either face to face (H-aggregates) or head to tail (J aggregates). (c) Intentional encapsulation in higher order structures, including in MOFs dispersed in a PDMS network, as is shown here. Adapted from ref. 69, licensed under CC BY-NC-ND. Adaptations made with author permission.

While the difficulty of measuring the step-wise isomerization kinetics of DASA in polymer films has generally resulted in our understanding of these systems lagging behind our understanding of solution-based systems, recent studies have observed substantially

slower rates of photoswitching and thermal recovery of DASA in glassy polymer films below their glass transition temperature compared to solution (see Fig. 1.6.b).[10,41,71] This result is also observed for similar photoswitches with a significant change in geometry during isomerization, including azobenzene [72–75], stilbene [76], and indigo [77]. In the specific case of azobenzene, an interesting phenomenon has been identified where the trans-to-cis photoisomerization occurs with two distinct kinetic regimes as a function of irradiation time in viscous environments that have some degree of microheterogeneity (Fig. 1.8). An example of one such environment is glycerol in DMSO, where the polymer chains tend to aggregate and the efficiency of photoisomerization is significantly different between the aggregate and solution phases.[75]

Similar biphasic kinetics have been observed for azobenzene in glassy polycarbonate films where microheterogeneity introduced during vitrification resulted in a distribution in the local free volume created to accommodate the photoswitch.[74] As a result, the azobenzene reaction sites exhibited two distinct kinetic behaviors: the site was considered freely mobile if the local free volume exceeded the threshold volume needed to accommodate isomerization and diffusion-controlled if the local free volume did not exceed this critical value. In the diffusion-controlled regime, the polymer

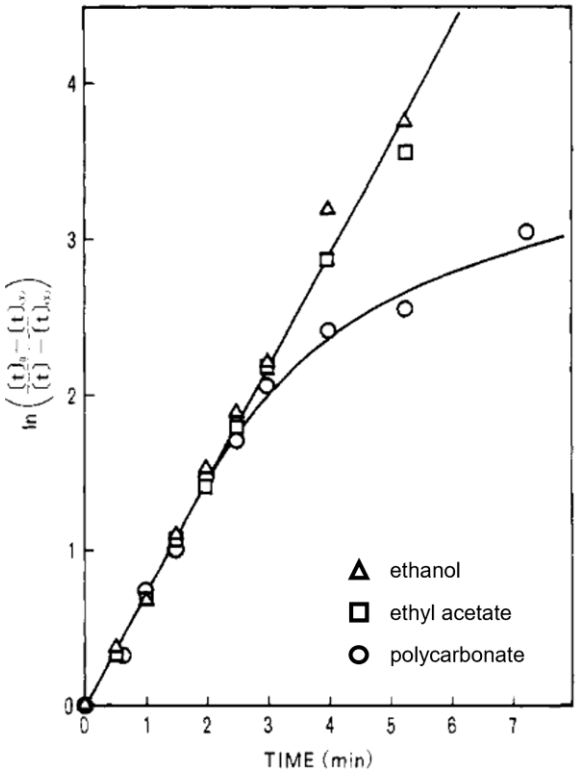

Fig. 1.8. First order plots for the trans-to-cis photoisomerization of azobenzene in ethanol, ethyl acetate and polycarbonate showing a deviation from first order kinetics in polycarbonate. Adapted with permission from ref. 74. Copyright 1989 American Chemical Society.

chain dynamics controlled the isomerization kinetics by affecting the local rate of density fluctuations about the critical free volume required for isomerization. Interestingly, azobenzene trans-to-cis photoisomerization shows a steep transition between these two kinetic regimes at 288 K despite the polymer free volume distribution being broad and continuous. This is because glassy polycarbonate has slow chain dynamics resulting in slow local density fluctuations relative to the measurement time scale (~ min) about the critical free volume needed for isomerization. As the temperature increases from 4 K to 288 K (the T_g of polycarbonate is approximately 450 K), larger density fluctuations in the polymer occur over the measurement time scale, resulting in the appearance of a more continuous transition between the freely mobile and diffusion limited kinetic regimes. A model describing the rate of azobenzene photoisomerization as a function of the relevant properties of the host polymer is provided by Mita et al.[74]

Thermal cis-to-trans isomerization of azobenzene has also been observed to deviate from first order kinetics in polymers. Two explanations have been proposed for this phenomenon. The first explanation was proposed by Eisenbach and attributes the slower thermal cis-to-trans isomerization at long times (~ minutes) after ceasing UV irradiation to relaxation of the polymer chains, erasing the free volume created initially to accommodate the trans isomer.[78] The second explanation, proposed by Paik and Morawetz, attributes the slower thermal cis-to-trans isomerization at long times to a spatial rather a temporal artifact as a result of the cis isomer being destabilized by elastic forces locally where photochemical trans-to-cis isomerization was diffusion controlled.[79] In addition to affecting the thermal cis-to-trans isomerization of azobenzene in polycarbonate, this phenomenon has also been observed for different azobenzene derivatives in various polymethacrylates[78–80] and PS[81]. With the bulk of these studies being performed on azobenzene, which has slow thermal recovery kinetics (~ minutes), it is unclear whether these unique photoisomerization and thermal recovery kinetics

occur in other photoswitches, like DASA, that thermally revert on a time scale that is more competitive with the chain relaxation timescales of rubbery polymers like PBMA and PHMA. The primary reason for this gap in knowledge is practical: measuring the step-wise isomerization kinetics of photoswitches like DASA is challenging due to their rapid thermal isomerizations and complex photoswitching mechanisms.

While the mechanical forces associated with confinement of DASA in polymeric environments are a dominant mechanism for shifting the energetics of isomerization, these forces cannot be modulated through the application of bulk external stress. As a result, we cannot use mechanical force as a stimulus to trigger a change in the physical or chemical properties of a DASA-containing material. To accomplish this, DASA must be incorporated into the backbone of the parent polymer or added as a crosslink between adjacent polymer chains. Compared to other photoswitches, this is more difficult to synthetically access because the conjugated backbone of the open form isomers (**A** and **B/B'**) is highly susceptible to reduction by the catalysts used in polymerization and crosslinking. This was partially circumvented by Robb and coworkers by incorporating a comparatively inert mechanochemically active DASA precursor into the polymer backbone of poly(methyl acrylate) (PMA), and using mechanical force initially to convert the precursor via retro cycloaddition into the activated furan acceptor which was subsequently converted to DASA after treating the sample to a secondary amine donor.[40] Upon the formation of DASA, a characteristic visible absorbance peak was observed and this absorbance was spatially correlated with the maximum stress attained during mechanical activation. This example of mechanically induced DASA formation was irreversible, unlike other mechanochromic material platforms, including SP in PU[82] and PMMA[83]; naphthopyran in PDMS [84] (Fig. 1.9.a); and azobenzene in PDMS[28] (Fig. 1.9.b). To enable reversible DASA photoactivation in the

future, less reactive cross-linking chemistries (e.g., urethane bonding in polyurethane) should be explored that are compatible with DASA integration.

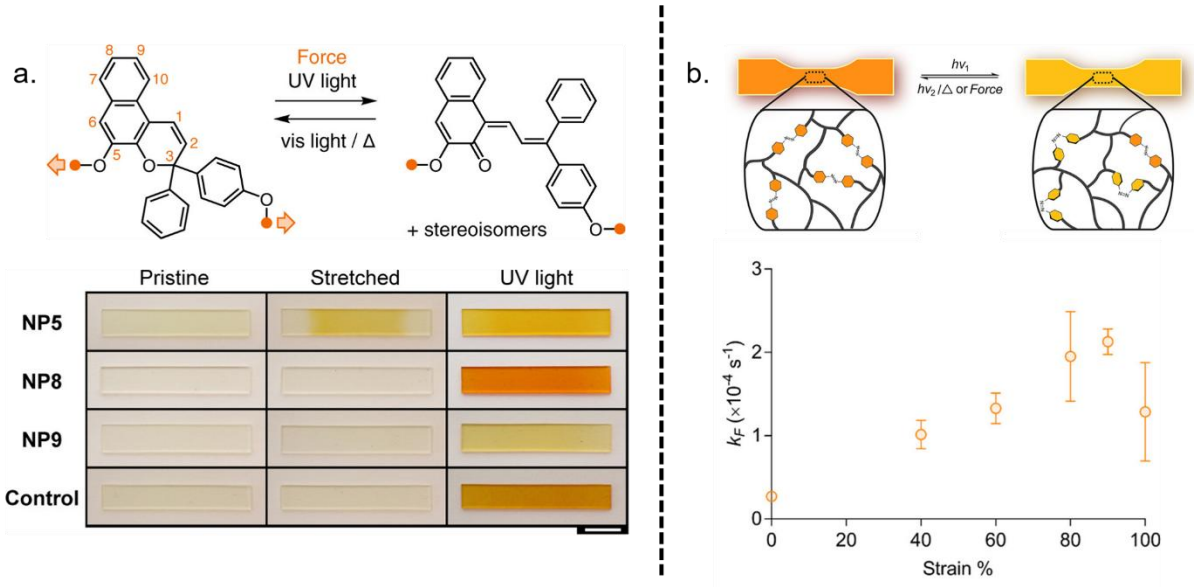

Fig. 1.9. (a) Mechanophoric isomerization of naphthopyran to merocyanine in PDMS. This isomerization can also be promoted photochemically using UV light and results in the material turning from transparent to orange. Only sample NP5 (pictured, top) displayed a mechanochromic response under tensile stress. When the force handle was moved from carbon 5 to carbons 8 (NP8) or 9 (NP9), no mechanophoric isomerization was observed. Scale bar = 1 cm. Adapted with permission from ref. 84. Copyright 2016 American Chemical Society. (b) Mechanically accelerated cis-to-trans isomerization (k_F) of azobenzene in PDMS under tensile strain. Adapted with permission from ref. 28. Copyright 2019 American Chemical Society.

1.3.4. Chemically sensitive DASA photochemistry

In addition to mechanical (non-polarizing) effects, the ground and excited state PESs are susceptible to the effects of inter- and intra- molecular polarizing interactions (e.g., dipole-dipole, dipole-induced dipole, hydrogen bonding, ion-dipole). While the role of chemical interactions can be difficult to distinguish from other matrix-induced effects, including mechanical confinement, less polar polymers are generally associated with a larger percentage of open form at equilibrium[41] and red-shifted open form absorbances[38]. These results are in line with solution-based studies, indicating that the effects of polarizing interactions and mechanical confinement can be separated by studying freely diffusing DASA

in chemically analogous solvents. The different types of polarizing specific and non-specific interactions are summarized in Fig. 1.10.

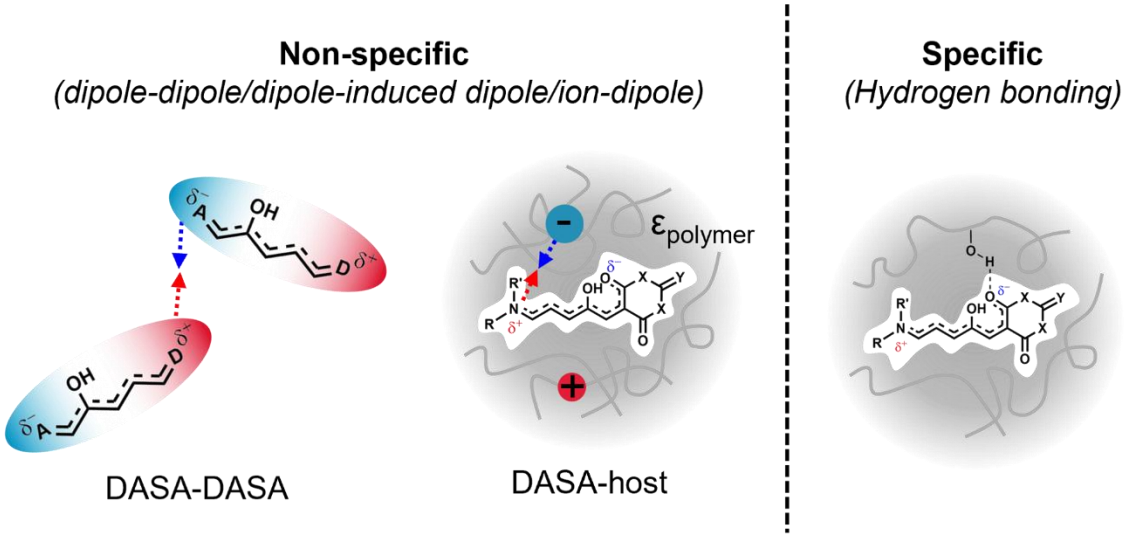

Fig. 1.10. Types of polarizing DASA-DASA and DASA-host interactions that affect absorbance and energetics of photoswitching including non-specific (dipole-dipole, dipole-ion, etc.) and specific (hydrogen bonding).

Depending on the degree of charge separation between the donor and acceptor in the open and closed isomers, polarizing intermolecular interactions affect the kinetics of photoswitching, dark equilibrium, and photostationary state differently. For example, first generation DASAs, which have a high degree of charge separation, show limited photoswitching in polar solvents[34] and in solvents modified with the addition of an ionic liquid[38]. Conversely, second generation DASAs are more neutral and are less affected by changes in solvent polarity[35,42] and ionic strength[38]. To help explain these observations, Feringa and colleagues used ultra-fast UV-Vis absorption spectroscopy to study the effect of solvent polarity on the rate and yield of the initial actinic **A** to **B** isomerization. They observed that solvent polarity had a minimal effect on the actinic step for select first and second generation DASAs, implying that solvent polarity primarily only affected the thermal isomerization barriers and the free energies of the isomers.[51]

Third generation DASAs, which are similar to the first generation in their degree of charge separation, show faster thermal recovery and a PSS enriched in the open (absorbing) form as ionic strength of the solvent is increased.[38] While third generation DASAs show reversible photoswitching in more polar solvents than first generation DASAs, a thorough study on the effect of solvent polarity on the rates of photoswitching and thermal recovery has not been performed.

These studies aimed at understanding the solvent dependence of DASA help to explain the previously observed concentration dependence in the rate of photoswitching for third generation DASA in solution. Owing to the strong dipole moment of DASA in both the open and closed forms (μ_{DASA} ~ 15 D)[60], high concentrations of DASA in solution effectively raise the solvent dielectric, resulting in the same open form enrichment in the PSS and slower thermal recovery that is observed in solvents with higher ionic strength. These concentration-dependent kinetics were not observed for second generation DASAs in solution, which is in line with their limited sensitivity to solvent polarity.[38] Interestingly, these concentration-dependent kinetics were also observed for third generation DASA in solid PMMA (10^{-1} M – 10^{-3} M), where the polymer matrix should be able to screen the effects of DASA-DASA interactions by preventing the free diffusion of DASA.[71] The reason for these concentration dependent kinetics in PMMA remains unknown.

Hydrogen bonding between DASA and its environment plays a significant role in determining the relative stability of the open and closed form isomers by disrupting the hydrogen bonding between the triene backbone hydroxyl and the carbonyl of the acceptor (see Fig. 1.3).[50,85] Recently, Peterson, et al. demonstrated reversible DASA photoswitching in polar protic solvents by tethering the donor amine nitrogen to the adjacent carbon in the triene backbone. This modification limited irreversible isomerization from **A** to **C** in the dark, but photoswitching was slow (500 s) and was not demonstrated in a purely aqueous solution.[50]

Typically, reversible effective photoswitching in polar protic solvents requires the stabilization of DASA in a polymer micelle or vesicle and continued efforts are necessary to enable reversible photoswitching of solvated DASA in aqueous environments for applications in biomedical technology and photopharmacology.

One additional type of chemical interaction with the potential to modulate the optical properties and photoswitching kinetics of DASA are aggregation-induced DASA-DASA interactions (see Fig. 1.7.b). Unlike the comparatively long-range dipolar DASA-DASA interactions responsible for the concentration-dependent photoswitching in solution, π-π stacking, facilitated by dipolar interactions, result in limited molecular mobility and impede photoswitching in the neat crystalline state[71] and in certain polymers that support aggregation[71]. For example, Lui, et al. observed absorption peak broadening and enhancement of the 0-1 vibronic feature with increasing concentrations of third generation DASA (10^{-1} M – 10^{-4} M) in polystyrene (PS), suggesting the presence of H-aggregates. Aggregation was not observed at similar concentrations in PMMA, toluene, or chloroform. [71]

1.4. Applications for polymeric photoactive materials in actuation

Among the diverse applications for photoactive soft materials, the potential to use these materials for converting light energy into mechanical work is particularly intriguing. This process is referred to as photoactuation and relies on interactions between an organic chromophore and a polymer host to convert energy from absorbed photons into a combination of heat and work. While traditional actuators perform work through the translation/rotation of rigid components, soft actuation occurs as a result of internal stresses generated within a deformable body. This allows these soft actuators to deform as a continuum, navigating tortuous and/or unfamiliar terrain with ease.[86]

Developing soft actuators that mimic the dexterity of their biological analogs (e.g., octopus tentacle, mammalian tongue) requires a high degree of spatiotemporal control over the distribution of local stresses generated during actuation. With the majority of soft actuators developed to date are powered pneumatically, modulating the fluid pressure at different locations within the actuator body to control its deformation requires a highly engineered network of fluid control elements (e.g., valves, tubes, compressors). By relying on light to power actuation instead, far greater spatial resolution is possible using mirrors, lenses, lightguides, and masks. While this resolution is nominally limited by the diffraction limit (~ 200 nm), converting the absorbed light into work typically occurs with less-than-perfect spatial fidelity depending on the mechanism of actuation. In practice, however, the spatial resolution achievable with photoactuation is still far superior to that of pneumatic actuation (mm[87,88]-m[88]). In addition to providing better spatial resolution, light is advantageous as a mechanism to control actuation because it can be delivered instantaneously (relative to the actuator response time), is continuously variable in multiple dimensions (wavelength, intensity, polarization, etc.), and is present in abundance as sunlight in nature.

1.4.1. Photoactuation mechanisms

1.4.1.1 Photothermal actuation

In the vast majority of light-powered soft actuators, force generation does not proceed directly by photomechanical conversion. Rather, actuation occurs thermomechanically and relies on the initial conversion of light into heat by embedded photothermal agents, including graphene nanostructures[89], gold nanoparticles[90–92], and/or organic dyes[93–95]. One example of photothermal actuation driving a phase change was demonstrated by Suzuki and Tanaka in 1990 where they used chlorophyllin photothermal absorbers to heat a poly(n-isopropylacrylamide) (PNIPAAm) hydrogel through its lower critical solution temperature,

resulting in the network contracting by expelling water.[96] More recently, photothermal actuation of a liquid crystal elastomer (LCE/LCP/LCN) was demonstrated by Lahikainen et al. using diarylethene (DAE) as the photothermal absorber.[94] Upon heating the LCE above the nematic to isotropic transition temperature, the film bent by 17° after 10 seconds of irradiation as a result of the twist alignment of the LCE crystal units (mesogens) in the nematic phase. To maximize the rate of photothermal heating, a combination of visible and UV light was used to drive DAE isomerization in the forward and reverse directions simultaneously. Simple single phase photothermal bilayer bending actuators (Fig. 1.11) have also been widely reported on, primarily because the deformation of these structures is well described by Timoshenko's bimetal thermostat model (Fig. 1.11.a)[97]

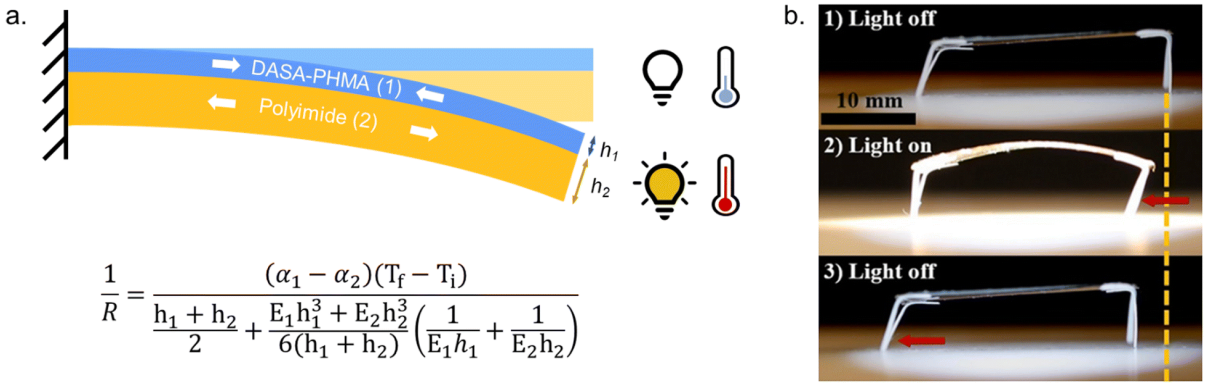

Fig. 1.11. Photothermal DASA–polymer film actuators. (a) Schematic illustration of photothermal bilayer actuation (top) with a DASA functionalized PHMA active layer (*cf.* Fig. 1.6). The radius of curvature (R) achieved upon photothermal heating from temperature T_i to T_f is defined according to the thermal bilayer beam bending equation (bottom) in terms of the elastic modulus (E), thickness (h), and thermal expansion coefficient (α) of each layer. Converging and diverging white arrows indicate the layers in compressive and tensile stress, respectively. Beam deflection occurs towards the layer in tensile stress, in this case, polyimide ($\alpha_2 < \alpha_1$). Reproduced from ref. 1. (b) Demonstration of a DASA-powered photothermal crawler based on the bilayer bending principle in (a). Figure adapted with permission from ref. 93. Copyright 2020, American Chemical Society.

Photothermal actuation is well suited for applications that benefit from faster, more energy efficient actuation and a simpler construction compared to actuation via direct photomechanical conversion. However, the heat transfer effects associated with photothermal

actuation make it challenging to establish and maintain steep thermal gradients, limiting the deformation to constant curvature or requiring that the deformation profile be pre-programmed into the actuator. While the theoretical Carnot limit ($\eta = 1 - T_C/T_H$) sets the upper bound on the photothermal actuation efficiency, the efficiency of photothermal actuation is often orders of magnitude lower in practice.[98–100] This is likely due to the impracticality of performing work adiabatically and independently controlling the stress and strain of a soft structure.

1.4.1.2 Photochemical actuation

For applications requiring a high degree of control over the local strain state and/or non-constant curvature deformation profiles, direct photomechanical conversion is possible with the use of organic photoswitches that isomerize under irradiation to generate macroscopic strain. This process is called photochemical actuation and typically requires an aligned material to transduce the molecular level motion into macroscopic work, either a crystal[101] or an LCE that undergoes a macroscopic phase change driven by photoswitching. Photochemical actuation is also possible in crosslinked polymer gels, where photoisomerization causes the gel to either contract or expand by dispelling or taking up solvent, respectively. This photoinduced swelling or deswelling occurs either through a change in the network hydrophilicity via an isomerization induced change in pH, dipole moment, and/or hydrogen bonding affinity[19,20], or through isomerization-induced (de-)crosslinking using guest host complexes that require a specific photoswitch geometry for complexation[15].

The unrivaled spatial control of photochemical actuation was demonstrated in 2003 using polarized light to control the deformation of an azobenzene loaded polydomain LCE. In this example, the polarization of the light was manipulated to selectively drive isomerization in micron-scale domains oriented along the polarization axis of the light.[102] Isomerization disrupted the local packing of the mesogens and induced a nematic-to-isotropic phase

transition that caused the film to bend along the alignment axis of the activated domains. In addition to providing robust spatial control, direct photomechanical conversion provides an avenue for photoactuation in environments that do not support efficient photothermal heating (e.g., underwater). To demonstrate this, Sartori et al. used photochemical actuation of an azo-loaded LCE to mimic the underwater swimming motion of the ephyra jellyfish, using UV light to deflect the actuator tentacles (lappets) downwards for a power stroke and visible light to return the tentacles back to their neutral position.[26]

Photochemical actuation typically requires strictly thin film geometries because actuation is highly localized to the irradiated surface. In thicker films, bending or twisting actuation is observed instead of uniaxial contraction because of the stress gradient over the sample thickness. In addition to geometric constrains, photochemical actuation efficiencies (10^{-6}-10^{-1} %)[25,103,104] are typically orders of magnitude lower than the theoretical limit (~ 10%), which is derived by assuming a quantum yield of unity and perfectly efficient molecular to macroscopic force transduction.[105] This is a consequence of mechanical confinement in polymers lowering the quantum efficiency of isomerization[100] and non-optimal thermodynamic properties of the host polymer that result in only a small fraction of the molecular level work being converted into macroscopic work.

1.4.2. Photoactuation powered by DASA

Despite the advantages afforded by light over other means of actuation, there are few examples of commercially viable photoactuated devices. This is primarily a consequence of the low power and efficiency associated with the conversion of light to work and the need for thin film actuator geometries. DASA presents a unique opportunity to expand the capabilities of existing photoactuators for several reasons. One such reason is that the photoproduct isomer is non-absorbing unlike other photoswitches, like azobenzene. This allows for

actuation in thicker materials because the penetration depth of light can be significantly greater. DASA also has the potential to work as a molecular motor because it undergoes a large reduction in end-to-end distance during photoswitching (approx 3.8 Å or 52%)[56]. In addition, the multi-responsive nature of DASA further allows light to be combined with other stimuli (e.g., pH, water, heat, mechanical stress, etc.), allowing for the integration of sensing and actuation with a single species. Finally, DASA is unique for its multi-chromic properties, which allow the relative rates of photoswitching and photothermal heating to be controlled independently by modulating the wavelength of light used to control the actuator (see Sec. 1.3.1). Depending on the mechanism of actuation (photothermal/photochemical), these processes may result in significant energy loss during actuation, and the ability to control them could increase the actuator efficiency and power output.

To date, the only example of DASA-powered photoactuation is the bilayer bending photothermal actuator pictured in Fig. 1.11.b. In this example, the rate of photothermal heating and the resulting bending angle was controlled using optical history, specifically the time of irradiation, which cannot be tuned dynamically. Additionally, the only possible mode of actuation was constant curvature bending deformation. Developing photoactuators that fully utilize DASA's unique photophysical properties requires a better understanding of how the rates of photoswitching and thermal recovery in polymers can be tuned by controlling the strength of inter- and intramolecular forces. By combining a fundamental exploration of the unique features of DASA photochemistry in polymers with the development of novel DASA-compatible polymerization and/or cross-linking strategies, we can begin to construct complex macromolecular architectures (e.g., LCEs, photoswitchable functionalized crosslinks) that support alternative mechanisms of photoactuation beyond single phase thermal expansion. In addition, we can leverage these fundamental insights to make targeted modifications to the

DASA architecture and/or host polymer to stabilize **B/B'** and enable dual wavelength photoswitching control in solid polymers and polymer-based actuators.

1.5. Overview

This thesis is divided into two main areas of study that are discussed in detail over the next several chapters. The first area focuses on DASA from a fundamental perspective as a stimuli responsive agent for imparting photoactive properties to polymers, specifically focusing on the role that the environment plays in controlling the optical properties and isomerization kinetics of DASA. To facilitate this effort, a new spectroscopic technique called frequency modulated pump probe spectroscopy, or FMPPS, is introduced to perform time resolved UV-Vis absorption spectroscopy and differential polarized light absorption spectroscopy. In chapter 2, the technique is described and employed to understand the role of polarity on the PES of DASAs with different amounts of charge separation by measuring **B/B'** during photoswitching. In chapter 3, FMPPS is used again to quantify the role of mechanical confinement on the PES of DASA by measuring the thermal and photochemically accelerated isomerization kinetics of **B/B'** in two different polymers and a toluene solution. The observed confinement effects are specifically discussed for their role in determining the ability of DASA-functionalized amorphous polymers to support the dual wavelength photoswitching control demonstrated previously in solution by Stricker et al. (see Section 1.3.1).[49] This fundamental exploration concludes with chapter 4, which focuses on the effect of anisotropic confinement on the optical anisotropy of chromophore-functionalized LCEs. In pursuit of this, a modified version of FMPPS is introduced to dynamically measure the optical anisotropy of a DASA-integrated LCE during compressive stress.

The second area of study explored in this thesis relates to the application of photoactive polymers in photothermal actuation. This topic is discussed in chapter 5, which

demonstrates photothermal actuation of a focus tunable fluid lens and a mechanically oscillating DASA-based polymeric cantilever.

1.6. References

(1) Clerc, M.; Sandlass, S.; Rifaie-Graham, O.; Peterson, J. A.; Bruns, N.; Read de Alaniz, J.; Boesel, L. F. Visible Light-Responsive Materials: The (Photo)Chemistry and Applications of Donor–Acceptor Stenhouse Adducts in Polymer Science. *Chem Soc Rev* **2023**. https://doi.org/10.1039/D3CS00508A.

(2) Zhao, Y.; Hua, M.; Yan, Y.; Wu, S.; Alsaid, Y.; He, X. Stimuli-Responsive Polymers for Soft Robotics. *Annu Rev Control Robot Auton Syst* **2022**, *5* (1), 515–545. https://doi.org/10.1146/annurev-control-042920.

(3) Ryabchun, A.; Li, Q.; Lancia, F.; Aprahamian, I.; Katsonis, N. Shape-Persistent Actuators from Hydrazone Photoswitches. *J Am Chem Soc* **2019**, *141* (3), 1196–1200. https://doi.org/10.1021/jacs.8b11558.

(4) Chen, H.; Zhao, Y. Applications of Light-Responsive Systems for Cancer Theranostics. *ACS Appl Mater Interfaces* **2018**, *10* (25), 21021–21034. https://doi.org/10.1021/acsami.8b01114.

(5) Zhuang, Y.; Ren, X.; Che, X.; Liu, S.; Huang, W.; Zhao, Q. Organic Photoresponsive Materials for Information Storage: A Review. *Advanced Photonics* **2020**, *3* (01). https://doi.org/10.1117/1.ap.3.1.014001.

(6) Szymański, W.; Beierle, J. M.; Kistemaker, H. A. V.; Velema, W. A.; Feringa, B. L. Reversible Photocontrol of Biological Systems by the Incorporation of Molecular Photoswitches. *Chemical Reviews*. August 14, 2013, pp 6114–6178. https://doi.org/10.1021/cr300179f.

(7) Orgiu, E.; Crivillers, N.; Herder, M.; Grubert, L.; Pätzel, M.; Frisch, J.; Pavlica, E.; Duong, D. T.; Bratina, G.; Salleo, A.; Koch, N.; Hecht, S.; Samorì, P. Optically Switchable Transistor via Energy-Level Phototuning in a Bicomponent Organic Semiconductor. *Nat Chem* **2012**, *4* (8), 675–679. https://doi.org/10.1038/nchem.1384.

(8) Zhang, H.; Hui, J.; Chen, H.; Chen, J.; Xu, W.; Shuai, Z.; Zhu, D.; Guo, X. Synergistic Photomodulation of Capacitive Coupling and Charge Separation Toward Functional Organic Field-Effect Transistors with High Responsivity. *Adv Electron Mater* **2015**, *1* (9). https://doi.org/10.1002/aelm.201500159.

(9) Xie, X.; Crespo, G. A.; Mistlberger, G.; Bakker, E. Photocurrent Generation Based on a Light-Driven Proton Pump in an Artificial Liquid Membrane. *Nat Chem* **2014**, *6* (3), 202–207. https://doi.org/10.1038/nchem.1858.

(10) Rifaie-Graham, O.; Ulrich, S.; Galensowske, N. F. B.; Balog, S.; Chami, M.; Rentsch, D.; Hemmer, J. R.; Read De Alaniz, J.; Boesel, L. F.; Bruns, N. Wavelength-Selective Light-Responsive DASA-Functionalized Polymersome Nanoreactors. *J Am Chem Soc* **2018**, *140* (25), 8027–8036. https://doi.org/10.1021/jacs.8b04511.

(11) Zhou, H.; Xue, C.; Weis, P.; Suzuki, Y.; Huang, S.; Koynov, K.; Auernhammer, G. K.; Berger, R.; Butt, H. J.; Wu, S. Photoswitching of Glass Transition Temperatures of

Azobenzene-Containing Polymers Induces Reversible Solid-to-Liquid Transitions. *Nat Chem* **2017**, *9* (2), 145–151. https://doi.org/10.1038/NCHEM.2625.

(12) Ming, Z.; Hua, X.; Xue, Y.; Lin, Q.; Bao, C.; Zhu, L. Visible Light Controls Cell Adhesion on a Photoswitchable Biointerface. *Colloids Surf B Biointerfaces* **2018**, *169*, 41–48. https://doi.org/10.1016/j.colsurfb.2018.04.062.

(13) Gately, T. J.; Li, W.; Mostafavi, S. H.; Bardeen, C. J. Reversible Adhesion Switching Using Spiropyran Photoisomerization in a High Glass Transition Temperature Polymer. *Macromolecules* **2021**, *54* (20), 9319–9326. https://doi.org/10.1021/acs.macromol.1c01262.

(14) Mostafavi, S. H.; Li, W.; Clark, K. D.; Stricker, F.; Alaniz, J. R. De; Bardeen, C. J. Photoinduced Deadhesion of a Polymer Film Using a Photochromic Donor-Acceptor Stenhouse Adduct. *Macromolecules* **2019**, *52* (16), 6311–6317. https://doi.org/10.1021/acs.macromol.9b00882.

(15) Takashima, Y.; Hatanaka, S.; Otsubo, M.; Nakahata, M.; Kakuta, T.; Hashidzume, A.; Yamaguchi, H.; Harada, A. Expansion-Contraction of Photoresponsive Artificial Muscle Regulated by Host-Guest Interactions. *Nat Commun* **2012**, *3*. https://doi.org/10.1038/ncomms2280.

(16) Kathan, M.; Kovaříček, P.; Jurissek, C.; Senf, A.; Dallmann, A.; Thünemann, A. F.; Hecht, S. Control of Imine Exchange Kinetics with Photoswitches to Modulate Self-Healing in Polysiloxane Networks by Light Illumination. *Angewandte Chemie International Edition* **2016**, No. 55, 13882–13886. https://doi.org/10.1002/ange.201605311.

(17) Levitus, M.; Glasser, G.; Neher, D.; Aramendla, P. F. Direct Measurement of the Dipole Moment of a Metastable Merocyanine by Electromechanical Interferometry. *Chem Phys Lett* **1997**, *277*, 118–124.

(18) Bletz, M.; Pfeifer-Fukumura, U.; Kolb, U.; Baumann, W. Ground-and First-Excited-Singlet-State Electric Dipole Moments of Some Photochromic Spirobenzopyrans in Their Spiropyran and Merocyanine Form. *Journal of Physical Chemistry A* **2002**, *106* (10), 2232–2236. https://doi.org/10.1021/jp012562q.

(19) Ziółkowski, B.; Florea, L.; Theobald, J.; Benito-Lopez, F.; Diamond, D. Self-Protonating Spiropyran-Co-NIPAM-Co-Acrylic Acid Hydrogel Photoactuators. *Soft Matter* **2013**, *9* (36), 8754–8760. https://doi.org/10.1039/c3sm51386f.

(20) Li, C.; Iscen, A.; Palmer, L. C.; Schatz, G. C.; Stupp, S. I. Light-Driven Expansion of Spiropyran Hydrogels. *J Am Chem Soc* **2020**, *142* (18), 8447–8453. https://doi.org/10.1021/jacs.0c02201.

(21) Rosario, R.; Gust, D.; Hayes, M.; Jahnke, F.; Springer, J.; Garcia, A. A. Photon-Modulated Wettability Changes on Spiropyran-Coated Surfaces. *Langmuir* **2002**, *18* (21), 8062–8069. https://doi.org/10.1021/la025963l.

(22) Zhao, L.; Seshadri, S.; Liang, X.; Bailey, S. J.; Haggmark, M.; Gordon, M.; Helgeson, M. E.; Read de Alaniz, J.; Luzzatto-Fegiz, P.; Zhu, Y. Depinning of Multiphase Fluid Using Light and Photo-Responsive Surfactants. *ACS Cent Sci* **2022**, *8* (2), 235–245. https://doi.org/10.1021/acscentsci.1c01127.

(23) Khairutdinov, R. F.; Hurst, J. K. Photocontrol of Ion Permeation through Bilayer Membranes Using an Amphiphilic Spiropyran. *Langmuir* **2001**, *17* (22), 6881–6886. https://doi.org/10.1021/la010756r.

(24) Yu, Y.; Ikeda, T. Alignment Modulation of Azobenzene-Containing Liquid Crystal Systems by Photochemical Reactions. *Journal of Photochemistry and Photobiology C: Photochemistry Reviews*. December 31, 2004, pp 247–265. https://doi.org/10.1016/j.jphotochemrev.2004.10.004.

(25) Serak, S.; Tabiryan, N.; Vergara, R.; White, T. J.; Vaia, R. A.; Bunning, T. J. Liquid Crystalline Polymer Cantilever Oscillators Fueled by Light. *Soft Matter* **2010**, *6* (4), 779–783. https://doi.org/10.1039/b916831a.

(26) Sartori, P.; Yadav, R. S.; del Barrio, J.; DeSimone, A.; Sánchez-Somolinos, C. Photochemically Induced Propulsion of a 4D Printed Liquid Crystal Elastomer Biomimetic Swimmer. *Advanced Science* **2024**, *11* (25). https://doi.org/10.1002/advs.202308561.

(27) Lahikainen, M.; Zeng, H.; Priimagi, A. Reconfigurable Photoactuator through Synergistic Use of Photochemical and Photothermal Effects. *Nat Commun* **2018**, *9* (1). https://doi.org/10.1038/s41467-018-06647-7.

(28) Lin, Y.; Hansen, H. R.; Brittain, W. J.; Craig, S. L. Strain-Dependent Kinetics in the Cis-to-Trans Isomerization of Azobenzene in Bulk Elastomers. *Journal of Physical Chemistry B* **2019**, *123* (40), 8492–8498. https://doi.org/10.1021/acs.jpcb.9b07088.

(29) Kim, T. A.; Beiermann, B. A.; White, S. R.; Sottos, N. R. Effect of Mechanical Stress on Spiropyran-Merocyanine Reaction Kinetics in a Thermoplastic Polymer. *ACS Macro Lett* **2016**, *5* (12), 1312–1316. https://doi.org/10.1021/acsmacrolett.6b00822.

(30) Dong, Y.; Ling, Y.; Wang, D.; Liu, Y.; Chen, X.; Zheng, S.; Wu, X.; Shen, J.; Feng, S.; Zhang, J.; Huang, W. *Harnessing Molecular Isomerization in Polymer Gels for Sequential Logic Encryption and Anticounterfeiting*; 2022; Vol. 8. https://www.science.org.

(31) Duan, Y.; Zhao, H.; Xue, G.; Sun, F.; Stricker, F.; Wang, Z.; Mao, L.; He, C.; De Alaniz, J. R.; Zheng, Y.; Wang, D. Controlling the Isomerization of Photoresponsive Molecules through a Limiting Tautomerization Strategy. *Journal of Physical Chemistry B* **2022**, *126* (17), 3347–3354. https://doi.org/10.1021/acs.jpcb.2c02005.

(32) Menzel, J. P.; Noble, B. B.; Blinco, J. P.; Barner-Kowollik, C. Predicting Wavelength-Dependent Photochemical Reactivity and Selectivity. *Nat Commun* **2021**, *12* (1). https://doi.org/10.1038/s41467-021-21797-x.

(33) Walden, S. L.; Carroll, J. A.; Unterreiner, A. N.; Barner-Kowollik, C. Photochemical Action Plots Reveal the Fundamental Mismatch Between Absorptivity and Photochemical Reactivity. *Advanced Science* **2024**, *11* (3). https://doi.org/10.1002/advs.202306014.

(34) Helmy, S.; Leibfarth, F. A.; Oh, S.; Poelma, J. E.; Hawker, C. J.; De Alaniz, J. R. Photoswitching Using Visible Light: A New Class of Organic Photochromic Molecules. *J Am Chem Soc* **2014**, *136* (23), 8169–8172. https://doi.org/10.1021/ja503016b.

(35) Mallo, N.; Brown, P. T.; Iranmanesh, H.; MacDonald, T. S. C.; Teusner, M. J.; Harper, J. B.; Ball, G. E.; Beves, J. E. Photochromic Switching Behaviour of Donor-Acceptor

Stenhouse Adducts in Organic Solvents. *Chemical Communications* **2016**, *52* (93), 13576–13579. https://doi.org/10.1039/C6CC08079K.

(36) Cai, Y. De; Chen, T. Y.; Chen, X. Q.; Bao, X. Multiresponsive Donor-Acceptor Stenhouse Adduct: Opportunities Arise from a Diamine Donor. *Org Lett* **2019**, *21* (18), 7445–7449. https://doi.org/10.1021/acs.orglett.9b02753.

(37) Zhao, H.; Qin, X.; Zhao, L.; Dong, S.; Gu, L.; Sun, W.; Wang, D.; Zheng, Y. Invisible Inks for Secrecy and Anticounterfeiting: From Single to Double-Encryption by Hydrochromic Molecules. *ACS Appl Mater Interfaces* **2020**, *12* (7), 8952–8960. https://doi.org/10.1021/acsami.0c00462.

(38) Sroda, M. M.; Stricker, F.; Peterson, J. A.; Bernal, A.; Read de Alaniz, J. Donor–Acceptor Stenhouse Adducts: Exploring the Effects of Ionic Character. *Chemistry - A European Journal* **2021**, *27* (12), 4183–4190. https://doi.org/10.1002/chem.202005110.

(39) Ulrich, S.; Hemmer, J. R.; Page, Z. A.; Dolinski, N. D.; Rifaie-Graham, O.; Bruns, N.; Hawker, C. J.; Boesel, L. F.; Read De Alaniz, J. Visible Light-Responsive DASA-Polymer Conjugates. *ACS Macro Lett* **2017**, *6* (7), 738–742. https://doi.org/10.1021/acsmacrolett.7b00350.

(40) Overholts, A. C.; Granados Razo, W.; Robb, M. J. Mechanically Gated Formation of Donor–Acceptor Stenhouse Adducts Enabling Mechanochemical Multicolour Soft Lithography. *Nat Chem* **2023**, *15* (3), 332–338. https://doi.org/10.1038/s41557-022-01126-5.

(41) McDonough, R.; Rudgley, N.; Majewski, O.; Perkins, M. V.; Evans, R. A.; Lewis, D. A. Photochromic Performance of Donor-Acceptor Stenhouse Adducts in Polymer Binders and Solution. *ChemPhotoChem* **2022**, *6* (9). https://doi.org/10.1002/cptc.202200076.

(42) Hemmer, J. R.; Poelma, S. O.; Treat, N.; Page, Z. A.; Dolinski, N. D.; Diaz, Y. J.; Tomlinson, W.; Clark, K. D.; Hooper, J. P.; Hawker, C.; Read De Alaniz, J. Tunable Visible and Near Infrared Photoswitches. *J Am Chem Soc* **2016**, *138* (42), 13960–13966. https://doi.org/10.1021/jacs.6b07434.

(43) Hemmer, J. R.; Page, Z. A.; Clark, K. D.; Stricker, F.; Dolinski, N. D.; Hawker, C. J.; Read De Alaniz, J. Controlling Dark Equilibria and Enhancing Donor-Acceptor Stenhouse Adduct Photoswitching Properties through Carbon Acid Design. *J Am Chem Soc* **2018**, *140* (33), 10425–10429. https://doi.org/10.1021/jacs.8b06067.

(44) Jia, S.; Tan, A.; Hawley, A.; Graham, B.; Boyd, B. J. Visible Light-Triggered Cargo Release from Donor Acceptor Stenhouse Adduct (DASA)-Doped Lyotropic Liquid Crystalline Nanoparticles. *J Colloid Interface Sci* **2019**, *548*, 151–159. https://doi.org/10.1016/j.jcis.2019.04.032.

(45) Jia, S.; Du, J. D.; Hawley, A.; Fong, W. K.; Graham, B.; Boyd, B. J. Investigation of Donor-Acceptor Stenhouse Adducts as New Visible Wavelength-Responsive Switching Elements for Lipid-Based Liquid Crystalline Systems. *Langmuir* **2017**, *33* (9), 2215–2221. https://doi.org/10.1021/acs.langmuir.6b03726.

(46) Hou, W.; Liu, R.; Bi, S.; He, Q.; Wang, H.; Gu, J. Photo-Responsive Polymersomes as Drug Delivery System for Potential Medical Applications. *Molecules* **2020**, *25* (21), 542–552. https://doi.org/10.3390/molecules25215147.

(47) Rifaie-Graham, O.; Ulrich, S.; Galensowske, N. F. B.; Balog, S.; Chami, M.; Rentsch, D.; Hemmer, J. R.; Read De Alaniz, J.; Boesel, L. F.; Bruns, N. Wavelength-Selective Light-Responsive DASA-Functionalized Polymersome Nanoreactors. *J Am Chem Soc* **2018**, *140* (25), 8027–8036. https://doi.org/10.1021/jacs.8b04511.

(48) Di Donato, M.; Lerch, M. M.; Lapini, A.; Laurent, A. D.; Iagatti, A.; Bussotti, L.; Ihrig, S. P.; Medved, M.; Jacquemin, D.; Szymański, W.; Buma, W. J.; Foggi, P.; Feringa, B. L. Shedding Light on the Photoisomerization Pathway of Donor-Acceptor Stenhouse Adducts. *J Am Chem Soc* **2017**, *139* (44), 15596–15599. https://doi.org/10.1021/jacs.7b09081.

(49) Stricker, F.; Sanchez, D. M.; Raucci, U.; Dolinski, N. D.; Zayas, M. S.; Meisner, J.; Hawker, Craig. J.; Martínez, Todd. J.; Read de Alaniz, J. A Multi-Stage Single Photochrome System for Controlled Photoswitching Responses. *Nat Chem* **2022**. https://doi.org/10.1038/s41557-022-00947-8.

(50) Peterson, J. A.; Neris, N. M.; Read de Alaniz, J. Tethered Together: DASA Design towards Aqueous Compatibility. *Chem Sci* **2023**, *14* (45), 13025–13030. https://doi.org/10.1039/d3sc02835f.

(51) Lerch, M. M.; Di Donato, M.; Laurent, A. D.; Medved', M.; Iagatti, A.; Bussotti, L.; Lapini, A.; Buma, W. J.; Foggi, P.; Szymański, W.; Feringa, B. L. Solvent Effects on the Actinic Step of Donor–Acceptor Stenhouse Adduct Photoswitching. *Angewandte Chemie* **2018**, *130* (27), 8195–8200. https://doi.org/10.1002/ange.201803058.

(52) Sandlass, S.; Stricker, F.; Fragoso, D.; de Alaniz, J. R.; Gordon, M. J. Effect of Polymer Host Matrix on Multi-Stage Isomerization Kinetics of DASA Photochromes. *J Photochem Photobiol A Chem* **2023**, *444*, 114964. https://doi.org/10.1016/j.jphotochem.2023.114964.

(53) Lerch, M. M.; Wezenberg, S. J.; Szymanski, W.; Feringa, B. L. Unraveling the Photoswitching Mechanism in Donor-Acceptor Stenhouse Adducts. *J Am Chem Soc* **2016**, *138* (20), 6344–6347. https://doi.org/10.1021/jacs.6b01722.

(54) Zulfikri, H.; Koenis, M. A. J.; Lerch, M. M.; Di Donato, M.; Szymański, W.; Filippi, C.; Feringa, B. L.; Buma, W. J. Taming the Complexity of Donor-Acceptor Stenhouse Adducts: Infrared Motion Pictures of the Complete Switching Pathway. *J Am Chem Soc* **2019**, *141* (18), 7376–7384. https://doi.org/10.1021/jacs.9b00341.

(55) Peterson, J. A.; Stricker, F.; Read De Alaniz, J. Improving the Kinetics and Dark Equilibrium of Donor-Acceptor Stenhouse Adduct by Triene Backbone Design. *Chemical Communications* **2022**, *58* (14), 2303–2306. https://doi.org/10.1039/d1cc06235b.

(56) Helmy, S.; Oh, S.; Leibfarth, F. A.; Hawker, C. J.; Read De Alaniz, J. Design and Synthesis of Donor-Acceptor Stenhouse Adducts: A Visible Light Photoswitch Derived from Furfural. *Journal of Organic Chemistry* **2014**, *79* (23), 11316–11329. https://doi.org/10.1021/jo502206g.

(57) Bull, J. N.; Carrascosa, E.; Mallo, N.; Scholz, M. S.; Da Silva, G.; Beves, J. E.; Bieske, E. J. Photoswitching an Isolated Donor-Acceptor Stenhouse Adduct. *Journal of Physical Chemistry Letters* **2018**, *9* (3), 665–671. https://doi.org/10.1021/acs.jpclett.7b03402.

(58) Mallo, N.; Foley, E. D.; Iranmanesh, H.; Kennedy, A. D. W.; Luis, E. T.; Ho, J.; Harper, J. B.; Beves, J. E. Structure-Function Relationships of Donor-Acceptor Stenhouse Adduct Photochromic Switches. *Chem Sci* **2018**, *9* (43), 8242–8252. https://doi.org/10.1039/c8sc03218a.

(59) Dolinski, N. D.; Page, Z. A.; Eisenreich, F.; Niu, J.; Hecht, S.; Read de Alaniz, J.; Hawker, C. J. A Versatile Approach for In Situ Monitoring of Photoswitches and Photopolymerizations. *ChemPhotoChem* **2017**, *1* (4), 125–131. https://doi.org/10.1002/cptc.201600045.

(60) Laurent, A. D.; Medveď, M.; Jacquemin, D. Using Time-Dependent Density Functional Theory to Probe the Nature of Donor–Acceptor Stenhouse Adduct Photochromes. *ChemPhysChem* **2016**, 1846–1851. https://doi.org/10.1002/cphc.201600041.

(61) Li, Y.; Zhu, C.; Gu, F.; Liu, F. Revisiting Photocyclization of the Donor-Acceptor Stenhouse Adduct: Missing Pieces in the Mechanistic Jigsaw Discovered. *Physical Chemistry Chemical Physics* **2023**, *25* (10), 7417–7422. https://doi.org/10.1039/d2cp05143e.

(62) García-Iriepa, C.; Marazzi, M.; Sampedro, D. From Light Absorption to Cyclization: Structure and Solvent Effects in Donor-Acceptor Stenhouse Adducts. *ChemPhotoChem* **2019**, *3* (9), 866–873. https://doi.org/10.1002/cptc.201900102.

(63) Sanchez, D. M.; Raucci, U.; Martínez, T. J. In Silico Discovery of Multistep Chemistry Initiated by a Conical Intersection: The Challenging Case of Donor-Acceptor Stenhouse Adducts. *J Am Chem Soc* **2021**, *143* (48), 20015–20021. https://doi.org/10.1021/jacs.1c06648.

(64) Sanchez, D. M.; Raucci, U.; Ferreras, K. N.; Martínez, T. J. Putting Photomechanical Switches to Work: An Ab Initio Multiple Spawning Study of Donor-Acceptor Stenhouse Adducts. *Journal of Physical Chemistry Letters* **2020**, *11* (18), 7901–7907. https://doi.org/10.1021/acs.jpclett.0c02401.

(65) Stranius, K.; Börjesson, K. Determining the Photoisomerization Quantum Yield of Photoswitchable Molecules in Solution and in the Solid State. *Sci Rep* **2017**, *7*. https://doi.org/10.1038/srep41145.

(66) Mason, B. P.; Whittaker, M.; Hemmer, J.; Arora, S.; Harper, A.; Alnemrat, S.; McEachen, A.; Helmy, S.; Read De Alaniz, J.; Hooper, J. P. A Temperature-Mapping Molecular Sensor for Polyurethane-Based Elastomers. *Appl Phys Lett* **2016**, *108* (4). https://doi.org/10.1063/1.4940750.

(67) Sroda, M. M.; Lee, J.; Kwon, Y.; Stricker, F.; Park, M.; Valentine, M. T.; Read de Alaniz, J. Role of Material Composition in Photothermal Actuation of DASA-Based Polymers. *ACS Appl Polym Mater* **2022**, *4* (1), 141–149. https://doi.org/10.1021/acsapm.1c01108.

(68) Nucci, M.; Jodra, A.; Frutos, L. M. Mechano-Photochemistry. In *Theoretical and Computational Photochemistry: Fundamentals, Methods, Applications and Synergy*

with Experimental Approaches; Elsevier, 2023; pp 447–471. https://doi.org/10.1016/B978-0-323-91738-4.00018-X.

(69) Sun, F.; Xiong, X.; Gao, A.; Duan, Y.; Mao, L.; Gu, L.; Wang, Z.; He, C.; Deng, X.; Zheng, Y.; Wang, D. Fast Photochromism in Solid: Microenvironment in Metal-Organic Frameworks Promotes the Isomerization of Donor-Acceptor Stenhouse Adducts. *Chemical Engineering Journal* **2022**, *427*. https://doi.org/10.1016/j.cej.2021.132037.

(70) Payne, L.; Josephson, J. D.; Scott Murphy, R.; Wagner, B. D. Photophysical Properties of Donor-Acceptor Stenhouse Adducts and Their Inclusion Complexes with Cyclodextrins and Cucurbit[7]Uril. *Molecules* **2020**, *25* (21). https://doi.org/10.3390/molecules25214928.

(71) Lui, B. F.; Tierce, N. T.; Tong, F.; Sroda, M. M.; Lu, H.; Read De Alaniz, J.; Bardeen, C. J. Unusual Concentration Dependence of the Photoisomerization Reaction in Donor-Acceptor Stenhouse Adducts. *Photochemical and Photobiological Sciences* **2019**, *18* (6), 1587–1595. https://doi.org/10.1039/c9pp00130a.

(72) Loucif-Saibi, R.; Nakatani, K.; Delaire, J. A.; Dumont, M.; Sekkat, Z. *Photoisomerization and Second Harmonic Generation in Disperse Red One-Doped and-Functionalized Poly (Methyl Methacrylate) Films*; 1993; Vol. 5. https://pubs.acs.org/sharingguidelines.

(73) Sekkat, Z.; Morichère, D.; Dumont, M.; Loucif-Saïbi, R.; Delaire, J. A. Photoisomerization of Azobenzene Derivatives in Polymeric Thin Films. *J Appl Phys* **1992**, *71* (3), 1543–1545. https://doi.org/10.1063/1.351228.

(74) Mita, I.; Horie, K.; Hirao, K. *Photochemistry in Polymer Solids. 9. Photoisomerization of Azobenzene in a Polycarbonate Film*; 1989; Vol. 22. https://pubs.acs.org/sharingguidelines.

(75) Ta-Li Chen, D.; Morawetz, H. Photoisomerization and Fluorescence of Chromophores Built into the Backbones of Flexible Polymer Chains. *Macromolecules* **1976**, *9* (3), 463–468.

(76) Gegiou, D.; Muszkat, K. A.; Fischer, E. Temperature Dependence of Photoisomerization. VI. The Viscosity Effect. *J Am Chem Soc* **1968**, *90* (1), 12–18.

(77) Kuntze, K.; Viljakka, J.; Virkki, M.; Huang, C. Y.; Hecht, S.; Priimagi, A. Red-Light Photoswitching of Indigos in Polymer Thin Films. *Chem Sci* **2023**, *14* (10), 2482–2488. https://doi.org/10.1039/d2sc06790k.

(78) Eisenbach, C. D. Relation between Photochromism of Chromophores and Free Volume Theory in Bulk Polymers. *Berichte der Bunsengesellschaft für physikalische Chemie* **1980**, *84* (7), 680–690. https://doi.org/10.1002/bbpc.19800840714.

(79) Sook Paik, C.; Morawetz, H. Photochemical and Thermal Isomerization of Azoaromatic Residues in the Side Chains and Backbone of Polymers in Bulk. *Macromolecules* **1972**, *5* (2), 171–177.

(80) Eisenbach, C. D. Effect of Polymer Matrix on the Cis - Trans Isomerization of Azobenzene Residues in Bulk Polymers . *Die Makromolekulare Chemie* **1978**, *179* (10), 2489–2506. https://doi.org/10.1002/macp.1978.021791014.

(81) Victor, J. G.; Torkelson, J. M. On Measuring the Distribution of Local Free Volume in Glassy Polymers by Photochromic and Fluorescence Techniques. *Macromolecules* **1987**, *20*, 2241–2250.

(82) Kim, T. A.; Beiermann, B. A.; White, S. R.; Sottos, N. R. Effect of Mechanical Stress on Spiropyran-Merocyanine Reaction Kinetics in a Thermoplastic Polymer. *ACS Macro Lett* **2016**, *5* (12), 1312–1316. https://doi.org/10.1021/acsmacrolett.6b00822.

(83) Beiermann, B. A.; Davis, D. A.; Kramer, S. L. B.; Moore, J. S.; Sottos, N. R.; White, S. R. Environmental Effects on Mechanochemical Activation of Spiropyran in Linear PMMA. *J Mater Chem* **2011**, *21* (23), 8443–8447. https://doi.org/10.1039/c0jm03967e.

(84) Robb, M. J.; Kim, T. A.; Halmes, A. J.; White, S. R.; Sottos, N. R.; Moore, J. S. Regioisomer-Specific Mechanochromism of Naphthopyran in Polymeric Materials. *J Am Chem Soc* **2016**, *138* (38), 12328–12331. https://doi.org/10.1021/jacs.6b07610.

(85) Mallo, N.; Tron, A.; Andréasson, J.; Harper, J. B.; Jacob, L. S. D.; McClenaghan, N. D.; Jonusauskas, G.; Beves, J. E. Hydrogen-Bonding Donor-Acceptor Stenhouse Adducts. *ChemPhotoChem* **2020**, *4* (6), 407–412. https://doi.org/10.1002/cptc.201900295.

(86) Mcmahan, W.; Chitrakaran, V.; Csencsits, M.; Dawson, D.; Walker, I. D.; Jones, B. A.; Pritts, M.; Dienno, D.; Grissom, M.; Rahn, C. D. Field Trials and Testing of the OctArm Continuum Manipulator *. In *2006 IEEE International Conference on Robotics and Automation*; IEEE: New York, 2006; pp 2336–2341.

(87) Kang, H. W.; Lee, I. H.; Cho, D. W. Development of a Micro-Bellows Actuator Using Micro-Stereolithography Technology. *Microelectron Eng* **2006**, *83* (4-9 SPEC. ISS.), 1201–1204. https://doi.org/10.1016/j.mee.2006.01.228.

(88) Usevitch, N. S.; Hammond, Z. M.; Schwager, M.; Okamura, A. M.; Hawkes, E. W.; Follmer, S. *An Untethered Isoperimetric Soft Robot*; 2020; Vol. 5. https://www.science.org.

(89) Yang, Y.; Liu, Y.; Shen, Y. Plasmonic-Assisted Graphene Oxide Films with Enhanced Photothermal Actuation for Soft Robots. *Adv Funct Mater* **2020**, *30* (14). https://doi.org/10.1002/adfm.201910172.

(90) Ge, F.; Lu, X.; Xiang, J.; Tong, X.; Zhao, Y. An Optical Actuator Based on Gold-Nanoparticle-Containing Temperature-Memory Semicrystalline Polymers. *Angewandte Chemie - International Edition* **2017**, *56* (22), 6126–6130. https://doi.org/10.1002/anie.201612164.

(91) Mishra, S. R.; Tracy, J. B. Sequential Actuation of Shape-Memory Polymers through Wavelength-Selective Photothermal Heating of Gold Nanospheres and Nanorods. *ACS Appl Nano Mater* **2018**, *1* (7), 3063–3067. https://doi.org/10.1021/acsanm.8b00394.

(92) Sun, Z.; Yamauchi, Y.; Araoka, F.; Kim, Y. S.; Bergueiro, J.; Ishida, Y.; Ebina, Y.; Sasaki, T.; Hikima, T.; Aida, T. An Anisotropic Hydrogel Actuator Enabling Earthworm-Like Directed Peristaltic Crawling. *Angewandte Chemie - International Edition* **2018**, *57* (48), 15772–15776. https://doi.org/10.1002/anie.201810052.

(93) Lee, J.; Sroda, M. M.; Kwon, Y.; El-Arid, S.; Seshadri, S.; Gockowski, L. F.; Hawkes, E. W.; Valentine, M. T.; Read De Alaniz, J. Tunable Photothermal Actuation Enabled by Photoswitching of Donor-Acceptor Stenhouse Adducts. *ACS Appl Mater Interfaces* **2020**, *12* (48), 54075–54082. https://doi.org/10.1021/acsami.0c15116.

(94) Lahikainen, M.; Kuntze, K.; Zeng, H.; Helantera, S.; Hecht, S.; Priimagi, A. Tunable Photomechanics in Diarylethene-Driven Liquid Crystal Network Actuators. *ACS Appl Mater Interfaces* **2020**, *12* (42), 47939–47947. https://doi.org/10.1021/acsami.0c12735.

(95) Guillen Campos, J.; Tobin, C.; Sandlass, S.; Park, M.; Wu, Y.; Gordon, M.; Read de Alaniz, J. Photoactivation of Millimeters Thick Liquid Crystal Elastomers with Broadband Visible Light Using Donor–Acceptor Stenhouse Adducts. *Advanced Materials* **2024**, *36* (35). https://doi.org/10.1002/adma.202404932.

(96) Suzuki, A.; Tanaka, T. Phase Transition in Polymer Gels Induced by Visible Light. *Nature* **1990**, No. 346, 345–347.

(97) Timoshenko, S. Analysis of Bi-Methal Thermosets. *J Opt Soc Am* **1925**, No. 11, 233–255.

(98) Yang, X.; Chen, Y.; Zhang, X.; Xue, P.; Lv, P.; Yang, Y.; Wang, L.; Feng, W. Bioinspired Light-Fueled Water-Walking Soft Robots Based on Liquid Crystal Network Actuators with Polymerizable Miniaturized Gold Nanorods. *Nano Today* **2022**, *43*. https://doi.org/10.1016/j.nantod.2022.101419.

(99) Loomis, J.; Panchapakesan, B. Dimensional Dependence of Photomechanical Response in Carbon Nanostructure Composites: A Case for Carbon-Based Mixed-Dimensional Systems. *Nanotechnology* **2012**, *23* (21). https://doi.org/10.1088/0957-4484/23/21/215501.

(100) Kuenstler, A. S.; Hayward, R. C. Light-Induced Shape Morphing of Thin Films. *Current Opinion in Colloid and Interface Science*. Elsevier Ltd March 1, 2019, pp 70–86. https://doi.org/10.1016/j.cocis.2019.01.009.

(101) Al-Kaysi, R. O.; Müller, A. M.; Bardeen, C. J. Photochemically Driven Shape Changes of Crystalline Organic Nanorods. *J Am Chem Soc* **2006**, *128* (50), 15938–15939. https://doi.org/10.1021/ja064535p.

(102) Yu, Y.; Nakano, M.; Ikeda, T. Directed Bending of a Polymer Film by Light. *Nature* **2003**, *425*, 145.

(103) Xu, W.; Sanchez, D. M.; Raucci, U.; Zhou, H.; Dong, X.; Hu, M.; Bardeen, C. J.; Martinez, T. J.; Hayward, R. C. Photo-Actuators via Epitaxial Growth of Microcrystal Arrays in Polymer Membranes. *Nat Mater* **2023**, *22* (9), 1152–1159. https://doi.org/10.1038/s41563-023-01610-4.

(104) Svanidze, A.; Guo, T.; Zheng, X.; Palffy-Muhoray, P. Light-Induced Stress and Work in Photomechanical Materials. *Phys Rev E* **2021**, *103* (5). https://doi.org/10.1103/PhysRevE.103.L051002.

(105) Hugel, T.; Holland, N. B.; Cattani, A.; Moroder, L.; Seitz, M.; Gaub, H. E. Single-Molecule Optomechanical Cycle. *Science (1979)* **2002**, *296*, 1103–1106.

Chapter 2

Frequency modulated pump probe spectroscopy to measure DASA photoswitching kinetics in solution

Adapted from the following publication:

1. Stricker, F.; Peterson, J.; Sandlass, S.K.; de Tagyos, A.; Sroda, M.; Seshadri, S.; Gordon, M.J.; Read de Alaniz, J., *Chem*, **9**, 1994-2005 (2023).

This chapter discusses a new UV-Vis spectroscopic technique called frequency modulated pump probe spectroscopy (FMPPS)[1] that, when combined with traditional UV-Vis, provides a means to measure photoactive systems with greater sensitivity and accuracy than is currently possible with commercial spectrophotometers. Furthermore, the technique works with any wavelength of light, provided a suitable detector exists and the optical period of the light substantially exceeds the time scales of the processes being probed. An additional consequence of deviating from spectrally resolved detection schemes is the ability of FMPPS to resolve optical signals that vary in polarization instead of or in addition to wavelength. Together, these advantages make FMPPS well suited to study a variety of materials with interesting and dynamic optical properties.

Using FMPPS, this chapter explores the effect of solvent polarity on the potential energy surface (PES) of DASAs with different amounts of charge separation along the triene backbone. While traditional UV-Vis is suitable for measuring the absorbance of the thermodynamically favored absorbing isomer of DASA (**A**), FMPPS allows for **A** and the metastable intermediate isomers, **B** and **B'**, to be dynamically measured for three different DASAs in solvents of varying polarity. Facilitated by the insights provided by FMPPS, traditional UV-Vis, and computational DFT modelling (performed elsewhere), this chapter outlines a generalized predictive scheme that relates the degree of donor-acceptor charge separation to the resulting polarity-induced effects on the photoswitching and thermal recovery kinetics of DASA.

2.1. Background and motivation

When choosing a spectroscopic tool/method for studying the isomerization kinetics of photochromic molecules, several factors must be considered to ensure the technique is compatible with the experimental objective. These factors include temporal resolution of the

instrument, the wavelength of light used to probe the system, the type of chemical information provided by the technique, and the relative sensitivity of the measurement to the molecule of interest. For example, while NMR and FTIR can provide more chemical information than UV-Vis spectroscopy, the former techniques are often not suitable for studying photoswitches in polymers because most macromolecules are NMR and IR active. As a result, UV-Vis spectroscopy is used exclusively to study these polymer-based systems, often at the cost of practical utility and structural insight.

Another major drawback associated with using UV-Vis spectroscopy to measure photoswitching kinetics is that the wavelengths of light used to probe the state of the system may overlap with the photochemically active absorption band(s) of the molecule. This has two major consequences: the act of measurement fundamentally affects the state of the system, and the narrow bandwidth light source(s) used for excitation (i.e., pumping) may interfere with the measurement and overwhelm the detector. While the former can be mitigated by minimizing the light intensity and sample exposure time, these actions also compromise the signal to noise ratio of the measurement. The latter is specifically an issue when studying photoswitching in polymer films because, unlike a well-mixed solution, the rate of photoisomerization in a solid film has a spatial dependence as a function of distance from the irradiated surface due to the photoswitches being immobilized. As a result, the intrinsic photoisomerization kinetics can only be measured accurately when the pump and probe beams are introduced at a small angle relative to one another at the film surface. This drastically increases the likelihood of signal interference from reflectance and diffuse scattering of the pump light by the sample.

Unlike thermal isomerizations, photochemical isomerizations are difficult to kinetically model because they lack a well-defined order in the concentration of the isomerizing species.[2] As a result, non-linear fitting is required to extract the relevant photochemical quantum yields

and/or thermal isomerization rate constants for multi-step and/or thermally reversible reactions. To circumvent this problem, photochemical kinetic measurements are typically performed in the limit of total absorbance where the rate law is approximately zeroth order in the absorber concentration. However, working in this limit also means that very little light reaches the detector relative to the amount introduced to the sample (< 1%), requiring long integration/exposure times and high light intensities to accurately measure the sample absorbance. For this reason, it is theoretically optimal to perform photochemical kinetic measurements in the opposite limit, i.e., at low absorbance, where the rate law can be approximated as first order in the absorber concentration. Unfortunately, absorbances in this range cannot easily be measured by standard spectrometers because they lack the necessary sensitivity.

Together, these challenges highlight the need for a new UV-Vis spectroscopic technique that provides the improved sensitivity needed to measure photochemical processes in the low absorbance regime without compromising the temporal resolution of standard spectrophotometers (~ ms). In addition, the new technique must be compatible with optical pumping without the pump light interfering with absorbance measurement or constraining the temporal resolution of the measurement to account for mechanical beam blocks or shutters.

2.2. Frequency modulated pump probe spectroscopy (FMPPS)

To address these demands, a spectroscopic technique called frequency modulated pump probe spectroscopy (FMPPS, Fig. 2.1) was developed to facilitate the study of DASA, specifically to allow the transient **B/B'** isomeric state to be experimentally observed in real time. While the technique is inherently wavelength non-specific, light sources in the UV-Vis spectral region were used in this work because they were easy to work with and aligned well with the photochemically active absorption bands of DASA. By compromising the spectral resolution of standard spectrophotometers, FMPPS was capable of providing the improved sensitivity needed to accurately measure the absorbance of **B/B'** and permitted simultaneous measuring and optical pumping, effectively increasing the temporal resolution of existing UV-Vis techniques.

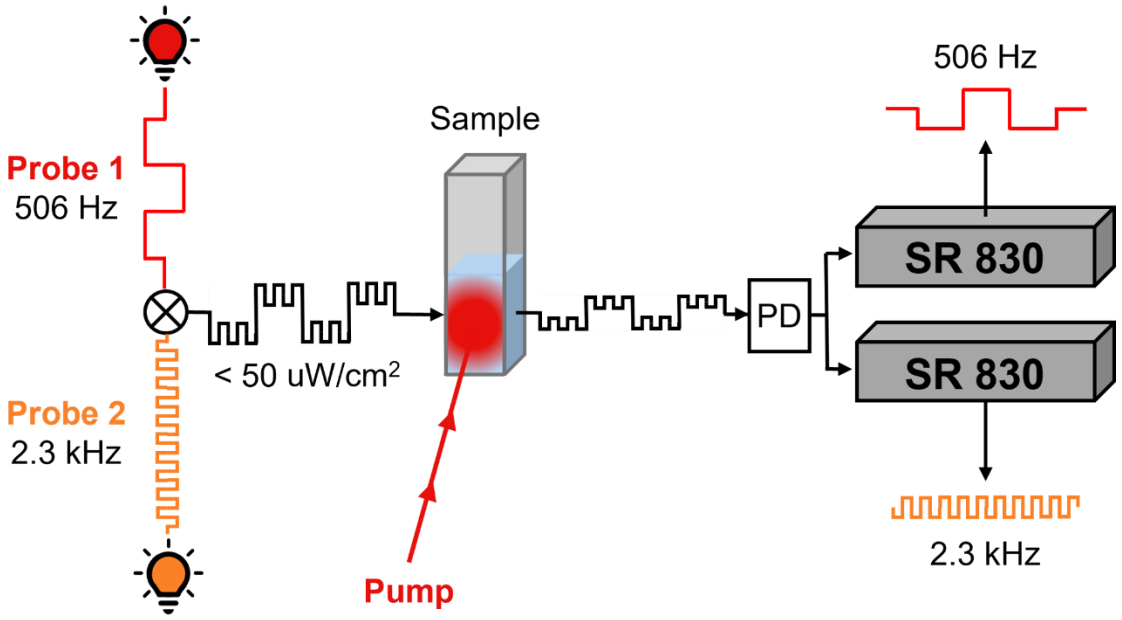

Fig. 2.1. Schematic illustration of the FMPPS technique used in this work. Two different wavelength probe beams are periodically modulated, combined, and passed through a sample cuvette. The transmitted beam intensity is measured with a photodiode (PD) and passed into two SR830 lock in amplifiers to deconvolve the transmitted intensities of each probe beam. To perform photochemical measurements, an unmodulated (continuous) pump beam is introduced at an angle relative to the probe beam. To limit diffusion effects, the entire sample area was irradiated with the pump beam.

In FMPPS, two or more light sources distinct in wavelength, polarization, and/or intensity are periodically modulated electronically or mechanically to “fingerprint” each light source with a characteristic frequency. This frequency is then used to deconvolve their respective intensities after interacting with the sample using a phase-locked wavelength indiscriminate detector. This detection scheme is inherently insensitive to all light that is not modulated at the specific frequencies that the detector is locked in to, including ambient light and stray light from the pump beam that would normally interfere with measurements performed on a spectrophotometer. As a result, this approach to performing pump-probe spectroscopy does not require a delay stage to accommodate mechanical beam flags or shutters between the pumping and probing steps, improving the effective temporal resolution of the measurement. In addition, the use of a phase-locked amplified detector makes this technique capable of accurately resolving changes in absorbance down to 0.004 a.u. at light intensities under 50 μW/cm^2.

To demonstrate how this technique can be used to gain valuable insight into the mechanism and kinetics of DASA photoswitching, FMPPS was used to track the absorbances of two narrow bandwidth probe beams as proxies for the populations of **A** and **B/B’** based on the system of equations below, where A_j and a_{ij} denote the composite absorbance of probe j and the absorbance of probe j by isomer i, respectively.

$$A_j = \sum_i a_{ij} \tag{2.1}$$

This system was fully specified for the case of two probes and two spectrally distinct absorbing isomers using Beer’s law to relate the a_{ij} for each isomer at the two probe wavelengths, $j = 1$ and $j = 2$, where ε_{ij} is the absorptivity of probe j by isomer i.

$$a_{i,2} = \frac{\epsilon_{i,2}}{\epsilon_{i,1}} a_{i,1} \tag{2.2}$$

The absorptivity ratio for isomer **A** was determined from the ratio of absorbances measured before optical pumping because **B** and **B'** were only populated under continuous photoexcitation of **A**. However, the absorptivity ratio of **B/B'** could only be quantified by selecting a probe wavelength such that one of the two $\varepsilon_{B/B',i}$ was equal to zero because these isomers were too unstable to be isolated under the experimental conditions. If an acceptable light source meeting this criteria could not be found among commercially available lasers and LEDs, the system of equations could still be solved for the absorbance of **B/B'** in terms of known quantities if one of the $\varepsilon_{A,i}$ was zero. However, in this case, the absorbance of **A** could not be isolated from **B/B'** in equation 2.1.

2.3. Resolving DASA intermediates using FMPPS to observe the effect of polarity on the PES of DASA with different amounts of charge separation

The environment polarity is known to affect the photoswitching and thermal recovery kinetics of first and second generation DASAs (*cf.* Section 1.3.4). However, no thorough study has been performed to date identifying the effect of polarity on third generation DASAs. In addition, while it has been suggested that the degree of charge separation between the donor and acceptor is responsible for the polarity dependence of DASA[3], a generalized rule describing the effect of polarity on the PES of chemically distinct DASAs has not been developed or experimentally validated. A contributing factor to the gap in understanding is the limited ability of existing spectroscopic techniques to experimentally observe **B/B'** during photoswitching due to limitations in their temporal resolution and sensitivity.

Using DFT calculations (M06-2X/def2-QZVP/SMD(cholorform)) to estimate the ground and transition state energies of **A**, **B**, **B'** and **C** for different solvent dielectrics (4.7, 7.5, 10), Stricker, Peterson, et al. found that increasing the solvent dielectric changes the PES of first, second, and third generation DASAs in a similar manner (Fig. 2.2.b).[1] They found that a higher

solvent dielectric effectively lowered the energy barrier for **B** to **A** and raised the **B** to **B'** barrier by shifting the amount of π character in the bonds associated with these two E/Z isomerizations (C_2-C_3 and C_3-C_4 in Fig. 2.2.a). In addition, they observed that the barrier for **B'** to **C** increased with increasing solvent polarity and attributed this to an increase in C_1-C_5 distance, which depended on the positions of the single and double bonds along the conjugated triene backbone in the dominant resonance contributor.

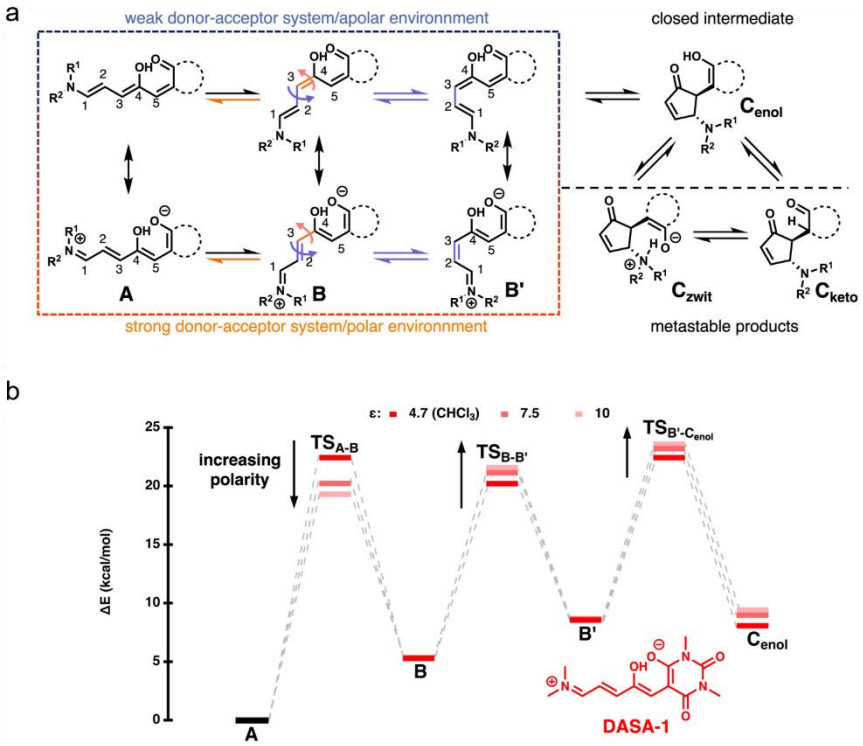

Fig. 2.2. (a) Dominant resonance conformers in non-polar (top) and polar (bottom) solvents showing the different positions of π bonds in the conjugated backbone relative to the positions of the **A/B** and **B/B'** E/Z isomerizations. (b) Effect of increasing solvent polarity on the PES of the first generation DASA structure shown at the bottom right. Reproduced from ref 1.

To understand why different DASAs respond differently to changes in solvent polarity, the energy landscapes for the three generations of DASA (DASA 1, 2, and 3 in Fig. 2.3) were modelled using DFT and compared in Fig. 2.3 to the polarity-induced changes in the PES illustrated in Fig. 2.2. In DASA 1 and 3, where the degree of charge separation between the

donor and acceptor is most significant, lower **B** to **A** and higher **B** to **B'** barriers were predicted compared to DASA 2, which has a less charge separated ground state. This should result in overall slower photoswitching in DASAs 1 and 3 by favoring **B** to **A** isomerization over **B** to **B'** and was confirmed using UV-Vis spectroscopy in dichloromethane (DCM, ε = 8.9), using acetonitrile (ACN, ε = 37.5) and diethyl ether (DEE, ε = 4.3) to increase and decrease the solvent polarity, respectively. While both DASA 1 and 3 showed slower open form recovery as solvent polarity increased, DASA 3 had a lower **B'** to **C** barrier and a more stabilized enol **C** conformer, resulting in faster photoswitching and faster thermal recovery than DASA 1. Interestingly, this resulted in DASA 3 reaching a PSS within 90 seconds of photoswitching that decreased in the open form population as the solvent polarity increased *or* decreased. This was a consequence of more polar solvents slowing down the rate of thermal recovery more significantly than they slowed the rate of photoswitching and less polar solvents speeding up the rate of photoswitching faster than they sped up the rate of thermal recovery. Conversely,

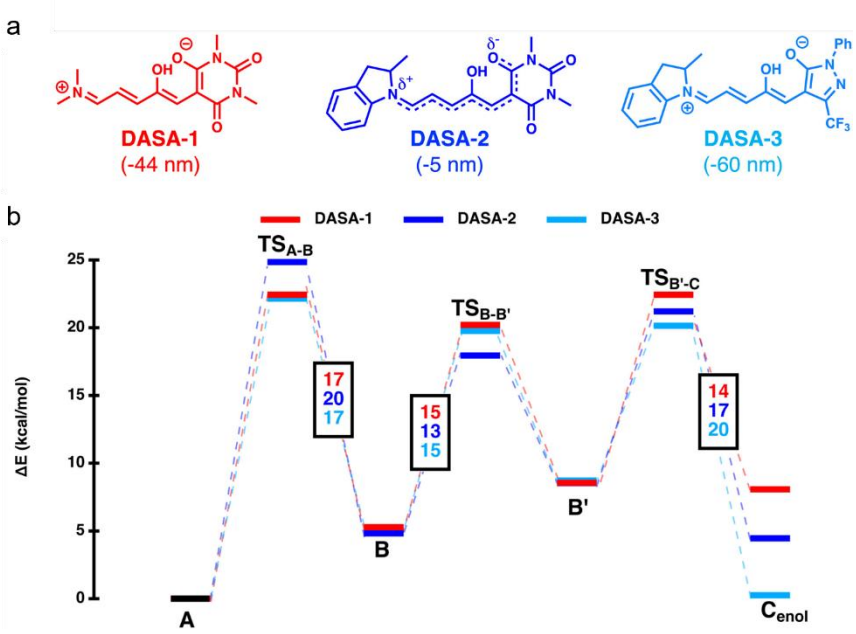

Fig. 2.3. Computed PES for first, second, and third generation DASAs with different amounts of charge separation reflected in their solvatochromic slopes (nm). Solvatochromic slopes are provided below their corresponding structures, and a more negative slope indicated a more charge separated ground state. Reproduced from ref. 1.

DASA 2 had a less charge separated ground state and showed minimal polarity dependence in the photoswitching rate, but faster open form recovery in more polar solvents. This was attributed to the high **B** to **A** thermal isomerization barrier in DASA 2 (see Fig. 2.3) rate limiting the isomerization from **C** back to **A** and decreasing as the solvent polarity increased. These results are presented in Fig. 2.4.

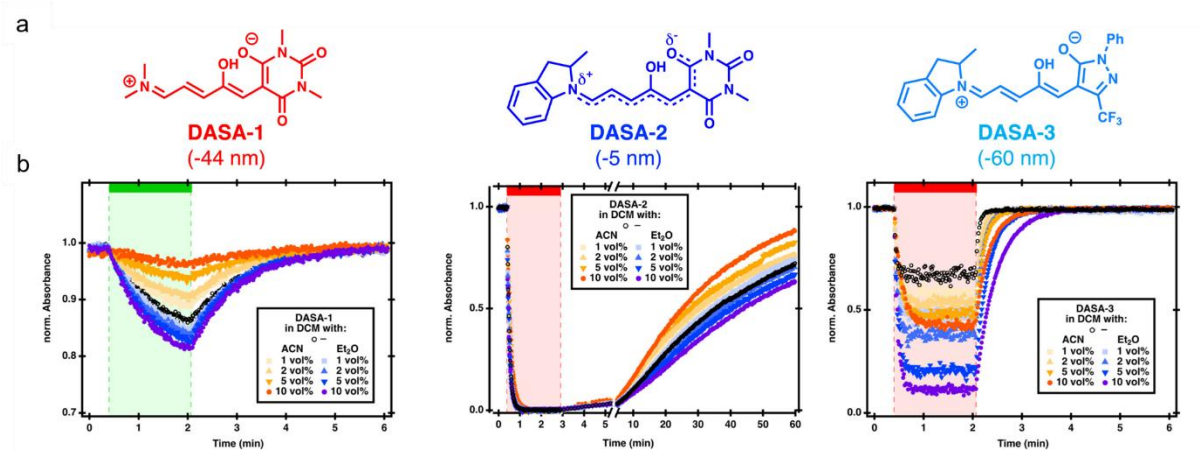

Fig. 2.4. Photoswitching and thermal recovery of DASAs 1, 2, and 3 during and after 90 s of irradiation showing the effect of increased (red/orange) and decreased (blue/purple) solvent polarity compared to pure DCM (black). Adapted from ref. 1.

To support the mechanistic explanations relating the experimental observations in Fig. 2.4 to the polarity-induced changes in the DASA PES, FMPPS was performed to measure **B/B**' during photoswitching in the same solvents as those used in Fig 2.4. For all measurements, two probe sources were used to fully specify the system of equations in equation 2.1 for two distinct absorbance states (**A** and **B/B'**). These light sources were individually modulated at 506 Hz (chopped) and 2.3 kHz (square wave gated), fiber coupled together and launched normal to a 1 mm thick x 1 cm wide glass cuvette with an active probing area 2 mm in diameter. The transmitted beam was picked up by a Thorlabs PDA36A Si Switchable Gain Detector and the output signal was passed into a pair of Stanford Research SR830 lock-in amplifiers to deconvolve the two probe amplitudes. Lock-in time constants were selected to ensure accurate signal integration over at least 5 periods; 10 ms and 3 ms on the high and low frequency modulated sources, respectively. LabVIEW data acquisition (National

Instruments BNC-2110) was used for real-time measurements at 25 Hz of the transmitted probe intensities during optical excitation and relaxation. The sampling interval was set by slower modulation frequency because its corresponding lock-in time constant was the fastest the system could respond to a discontinuous change in signal amplitude.

Optical excitation occurred by high intensity laser pumping with an active pump area 1.2 cm in diameter. This area ensured the entire sample volume was subjected to maximally uniform pump intensity because the cuvette was too small to be stirred to minimize diffusion effects in the observed photoswitching rates. The pump timing was controlled by LabVIEW with a mechanical beam flag and set to 3 s for all samples in the series. This pump duration ensured the thermal steps governing the overall DASA kinetic process could be followed without fully converting the open form to the metastable closed forms.

The modular nature of this setup allowed the pump and probe sources to be switched out easily to ensure strong overlap with the different absorption profiles of DASAs 1, 2, and 3. This series employed two laser pumping sources: a 532 nm non-polarized Nd:YAG laser (P1), and a 640 nm diode laser (P2). Three additional probe sources were required: a 620 nm LED (Pr1), a 660 nm LED with (Pr2-f), and without (Pr2) a 659 nm high pass filter and a 700 nm LED (Pr3). By splitting the pump laser beam into two lines of high and low intensities, it could simultaneously serve as a pumping and probing source. The pumping wavelength was selected to maximize DASA absorbance, while keeping to wavelengths below the **A** isomer's λ_{max} to prevent photochemical **B** to **A** isomerization. When possible, one probe source was selected to have minimal emission above the λ_{max} of **A**. This ensured that the necessary conditions for solving the system of equations in equation 2.1 were met. In the specific case of DASA 2, a light source could not be found to satisfy $\varepsilon_{B/B';j} = 0$. As a result, the absorbance of **A** could not be solved for in equation 2.1 without knowing the molar absorptivity of **B/B'** at both probe wavelengths. In this case, the absorbance of **B/B'** could still be measured by

choosing one probe wavelength to satisfy $\varepsilon_{A,j} = 0$. The pump and two probe light sources used to measure the absorbance of **A** and **B/B'** for DASAs 1, 2, and 3 along with their corresponding intensities are summarized in Table 2.1 based on the abbreviated light source naming convention indicated above. Absorbance spectra for each DASA before and after 2 s of irradiation are plotted overlaid with the probe emission profiles in the left column of Fig. 2.5.

Table 2.1. Summary of the light sources used to optically pump **A** and probe the absorbances of **A** and **B/B'** using FMPPS. An asterisk is used to indicate the probe beam that was modulated at 506 Hz. The probe sources without asterisks were modulated at 2.3 kHz.

	Pump		**Probe A**		**Probe B**	
	Light Source	Intensity (mW/cm^2)	Light Source	Intensity ($\mu W/cm^2$)	Light Source	Intensity ($\mu W/cm^2$)
DASA 1	P1	17.1	P1*	2.5	Pr1	1.8
DASA 2	P1	17.2	P2*	13	Pr2-f	21
DASA 3	P2	10.6	P2*	14.1	Pr2	3.4

The absorbances of **A** and **B/B'** normalized to the initial absorbance **A** during 3 s of irradiation are presented in the right column of Fig. 2.5. In the case of DASA 1, increasing the solvent polarity resulted in slower photoswitching, indicated by the change in the absorbance of **A** over time, and a drop in the **B/B'** population in equilibrium with **A** during switching. This aligns with the mechanistic justification used to explain the slower photoswitching and slower recovery observed in Fig. 2.4 for more polar solvents. As the **B** to **A** barrier shrinks with increasing polarity, the **A** to **B** equilibrium shifts away from **B** resulting in a reduced **B/B'** absorbance during photoswitching. A similar decrease in the **B/B'** population during photoswitching is observed for DASA 2 in more polar solvents. However, because the **B** to **A** barrier is natively much higher for DASA 2 than DASA 1 (see Fig. 2.3), we can see that an increase in polarity also results in faster equilibration between **A** and **B/B'** in DASA 2 under irradiation because the barrier for **B** to **A** isomerization is lower in more polar solvents (see

Fig. 2.2). Unfortunately, the absorbance of **B/B'** during photoswitching was too low to experimentally measure (< 0.004 a.u.) by FMPPS in the case of DASA 3. This was an expected result of the lower **B'** to **C** and **B** to **A** isomerization barriers for DASA 3 compared to DASAs 1 and 2 (see Fig. 2.3).

Leveraging these insights provided by the combination of traditional UV-Vis and FMPPS, Stricker, Peterson and coworkers demonstrated the use of polarity as a non-selective stimulus to affect the kinetics of DASA 1 (7.5 μM), 2 (15 μM), and 3 (7.5 μM) differently when co-dissolved in a toluene solution.[1] In this experiment (Fig. 2.6), light exposure resulted in photoswitching and a corresponding drop in absorbance for DASAs 1 and 3 while DASA 2 remained closed (non-absorbing) under the mild light intensities used to probe the sample absorbance because of the slower open form recovery kinetics of DASA 2 compared to DASAs 1 and 3. When the solvent polarity was increased following the addition of 15 vol% DMSO, the rate of thermal recovery slowed modestly for DASA 1, resulting in a new dark equilibrium enriched in **C** and a small drop in absorbance. In this more polar environment, the thermal recovery of DASA 3 slowed dramatically, resulting in a dark equilibrium enriched in **C** and a 94% drop in absorbance. Simultaneously, DASA 2 isomerized from **C** to **A** and adopted a new more absorbing dark equilibrium as a result of the lower **B** to **A** isomerization barrier in more polar solvents. In this new, more polar environment, light exposure resulted in reversible switching of DASA 2, but negligible switching of DASA 1 because of the lower **B** to **A** barrier in more polar solvents driving **B** back to **A** under irradiation.

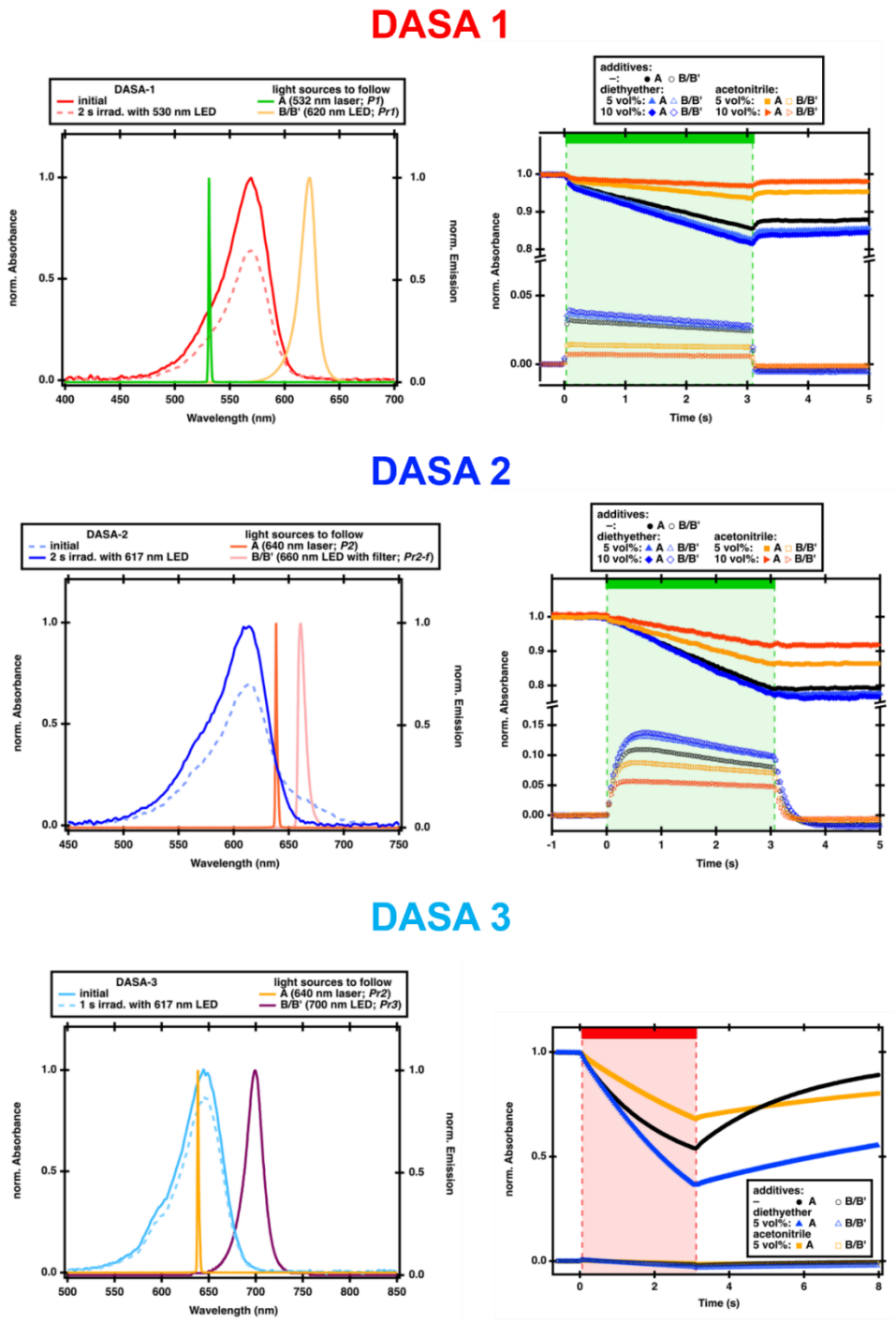

Fig. 2.5. Using FMPPS to probe **B/B'** during photoswitching. The two light sources used to measure **A** and **B/B'** using equation 2.1 are overlaid with the absorption spectra of DASAs 1, 2, and 3 before and after 1-2 s of irradiation in the left column. In the case of DASA 2, a suitable light source for measuring the absorbance of A could not be found (see Section 2.2). The absorbance of the 640 nm probe light is plotted as an approximation for the **A** population but is likely a combination of **A** and **B/B'**. Adapted from ref. 1.

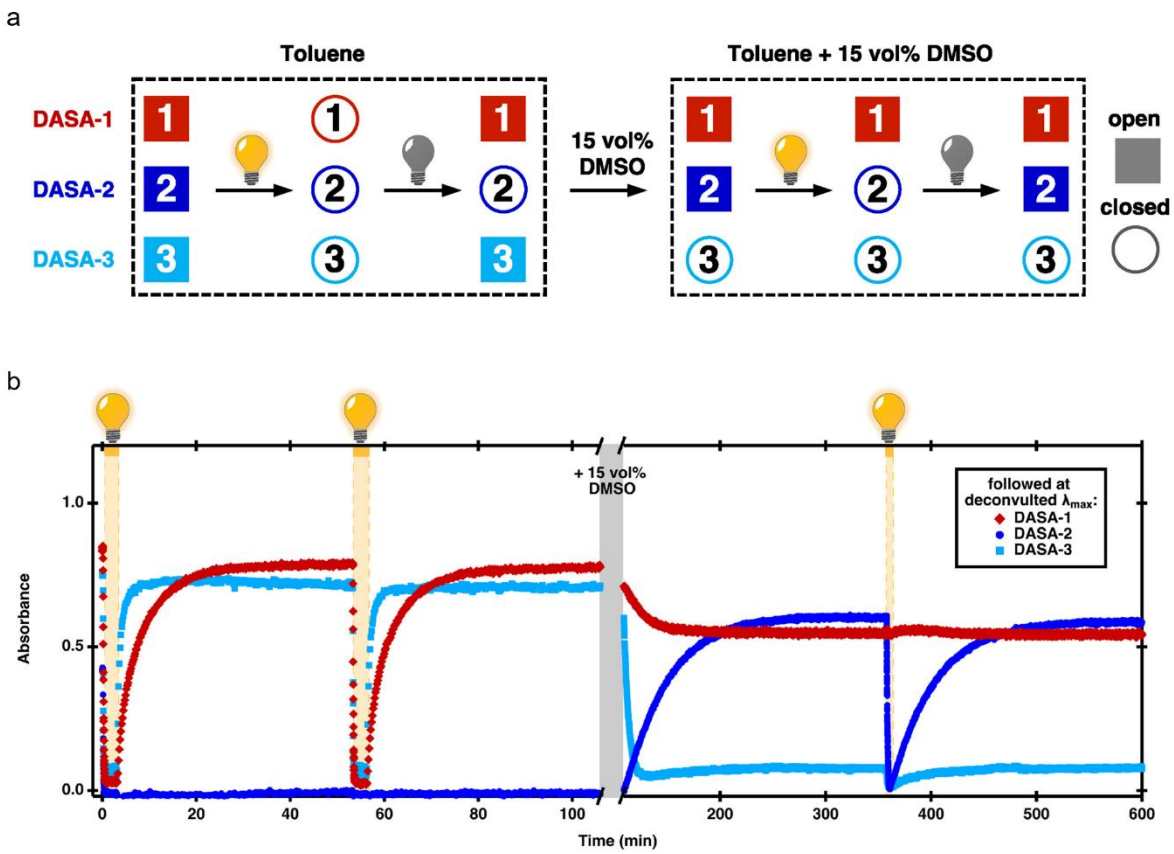

Fig. 2.6. Selective control of DASA 1, 2, and 3 populations using solvent polarity. (a) schematic diagram showing the effect of light and polarity on the dominant thermodynamically favored isomer (square = open, circle = closed). (b) Effect of light and polarity on the normalized absorbances of DASA 1, 2, and 3 co-dissolved in toluene. Adapted from ref. 1.

This demonstration, enabled by the mechanistic insights provided by a combination of FMPPS, traditional UV-Vis spectroscopy, and DFT calculations, highlights the importance of polarity as a non-selective stimulus for selectively controlling the PES of DASAs with different degrees of backbone charge separation. In addition, these experimental and theoretical techniques help to uncover a general mechanistic framework that explains the differences in the polarity sensitivity between first and second generation DASAs. This general trend is also found to hold true for third generation DASA, which had been largely unstudied in the context of solvent polarity up to this point. By extending this knowledge to DASA-functionalized polymers and other hierarchical assemblies (colloids, vesicles, etc.), a simple heuristic

argument based on the dielectric properties of the local environment and the degree of DASA charge separation can help us to separate the effects of polarity from more complex interactions to facilitate a better understanding of how these environments modify the DASA PES.

2.4. References

(1) Stricker, F.; Peterson, J.; Sandlass, S. K.; de Tagyos, A.; Sroda, M.; Seshadri, S.; Gordon, M. J.; Read de Alaniz, J. Selective Control of Donor-Acceptor Stenhouse Adduct Populations with Non-Selective Stimuli. *Chem* **2023**, No. 9, 1994–2005. https://doi.org/10.1016/j.chempr.2023.05.011.

(2) Stranius, K.; Börjesson, K. Determining the Photoisomerization Quantum Yield of Photoswitchable Molecules in Solution and in the Solid State. *Sci Rep* **2017**, *7*. https://doi.org/10.1038/srep41145.

(3) Sroda, M. M.; Stricker, F.; Peterson, J. A.; Bernal, A.; Read de Alaniz, J. Donor–Acceptor Stenhouse Adducts: Exploring the Effects of Ionic Character. *Chemistry - A European Journal* **2021**, *27* (12), 4183–4190. https://doi.org/10.1002/chem.202005110.

Chapter 3

Quantifying the effect of mechanical confinement on the isomerization kinetics of DASA in amorphous polymer films

Adapted from the following publication:

1. **Sandlass, S.**; Stricker, F.; Fragoso, D.; Read de Alaniz, J.; Gordon, M.J., Effect of polymer host matrix on multi-stage isomerization kinetics of DASA photochromes. *J. Photochem. Photobiol. A: Chem.*, **444**, 114964 (2023).

DASAs are promising candidates for next generation stimuli responsive materials. One reason for this is the unique ability of DASA to stabilize three photochemically distinct isomeric states in solution while other common photoswitches are limited to binary state distributions. Translating this ability to polymer-based systems is advantageous for applications in soft lithography, actuation, impact sensing, and photoswitching in aqueous systems. However, DASA reactivity is coupled to the molecular energetic landscape, which is known to be highly sensitive to the effects of mechanical confinement in polymers (*cf.* Section 1.3.3). To offset these matrix-induced effects, researchers require a better understanding of exactly how the forces arising from mechanical confinement affect the PES of DASA.

This chapter explores the effect of mechanical confinement on the isomerization kinetics of DASA in amorphous polymers. To facilitate this analysis, FMPPS (*cf*. Section 2.2) was used to measure the thermal and photochemically accelerated lifetimes of the intermediate isomer **B/B'** in different polymers/solvents. Interestingly, the rate of **B/B'** isomerization with and without optical excitation appear the be largely independent of the viscosity of the host environment, showing similar kinetics in toluene, rubbery poly(butyl methacrylate) (PBMA), and glassy poly(methyl methacrylate) (PMMA). However, the rate of **B/B'** formation and thus the absorbance of **B/B'** in equilibrium with **A** during photoswitching was significantly reduced as the rigidity of the host environment increased. These results align with previous observations made using ultrafast pump probe UV-Vis absorption spectroscopy[2] and provide a rationale for the negative correlation observed between the viscosity of the environment and the ability to control DASA as a multi-state photoswitch using dual wavelength control.

3.1. Introduction

With applications from consumer products to medical devices, light-responsive “smart” materials are at the forefront of research and development endeavors worldwide. While the field encompasses a broad range of chemistries, these materials all rely on some form of molecular or atomic-scale logic to impart synthetic structures with optical stimuli-responsive properties. Despite the unmatched spaciotemporal tunability of light (e.g., wavelength, intensity, and polarization), most examples of photoresponsive smart materials employ binary logic, i.e., they convert from state A to state B when the light is on and revert to A either when the light is removed (T-type) or when a secondary wavelength is introduced (P-type). Multistate (>2) photoresponsive materials have been demonstrated by combining absorbance-shifted binary switches[3–5], but the introduction of single species multistate photoswitches could enhance the device’s capacity for complex logic and improve its dynamic reconfigurability.

Recently, Stricker et al. demonstrated DASA as a rare example of a multistate photoswitch by sterically modifying a first generation DASA structure to stabilize **B** and **B’**, allowing these isomers to thermally accumulate during photoswitching in high enough concentrations to be controlled with a second wavelength of light (cf. Section 1.3.1). In addition to intramolecular forces, intermolecular forces, including those arising from chemical interactions and mechanical confinement, also affect the PES of DASA and change the amount of **B/B’** accumulated during photoswitching (cf. Section 2.3). However, unlike intramolecular forces or polarizing intermolecular interactions in solution, the effect of mechanical confinement in polymers on the PES of DASA remains poorly understood. For example, while it has been reported that the rates of photoswitching and thermal recovery increase as the polymer glass transition temperature decreases[3,6,7] (cf. Section 1.3.3), no study has successfully observed **B/B’** in an amorphous solid polymer. As a result, it is difficult

to predict whether or not the multistate reactivity demonstrated by Stricker et al. in solution is achievable in solid polymers and, if so, what types of chemical modifications may be necessary to achieve this.

In this work, the capacity for dual wavelength, multistate kinetic control of DASA is found to be diminished when physically blended into films of poly(butyl methacrylate) (PBMA) and poly(methyl methacrylate) (PMMA) compared to the native reactivity in toluene. To provide mechanistic insight into these results, FMPPS is employed to probe the rapid formation and decay kinetics of the **B**/**B'** intermediates in these varied environments. While the pseudo-equilibrium intermediate population established under irradiation of **A** is reduced in polymer blends, specifically in glassy PMMA, kinetic modeling shows that the thermal stability of **B/B'** has minimal dependence on the mechanical properties of the environment. Instead, the diminished capacity for multistate kinetic control in PBMA and PMMA can be attributed to matrix-induced effects that specifically impede the initial actinic conversion from **A** to **B**, limiting accumulation of the photochemically distinct intermediates that make DASA unique.

3.2. Methods

3.2.1. Sample preparation

The specific first generation DASA molecule used in this study (see Fig. 3.1) was synthesized and isolated according to the method in Sroda et al.[8] DASA-loaded polymer films were fabricated by casting a solution of DASA and either poly(butyl methacrylate) (PBMA, avg. 211kDa) or poly(methyl methacrylate) (PMMA, avg. 120kDa) in dichloromethane onto a glass supported polyethylene terephthalate (PET) substrate (50 μm thickness). The resulting bilayer films were peeled from their glass supports and dried in vacuum overnight. The films were cast and dried at room temperature, approximately 23 ^{o}C. Glass transition temperatures

for the polymers were measured by DSC to be 33 °C and 98 °C for PBMA and PMMA, respectively. When blended with 1 wt% of DASA, the corresponding glass transition temperatures decreased to 32 °C and 82 °C. After drying, the spatially averaged thicknesses of the DASA-loaded polymethacrylate layers were estimated to be approximately 10-15 μm, based on the known substrate surface area, the masses of the deposited polymers, and their densities. Due to the relatively low precision of the drop casting method compared to alternative manufacturing methods (e.g., spin coating, drawing), the localized film thicknesses were subject to variability of up to several microns. This degree of imprecision was deemed acceptable because the analysis performed in this study did not require a robust measure of sample dimensions. PBMA and PMMA were purchased from Sigma Aldrich and the PET films were from McMaster Carr.

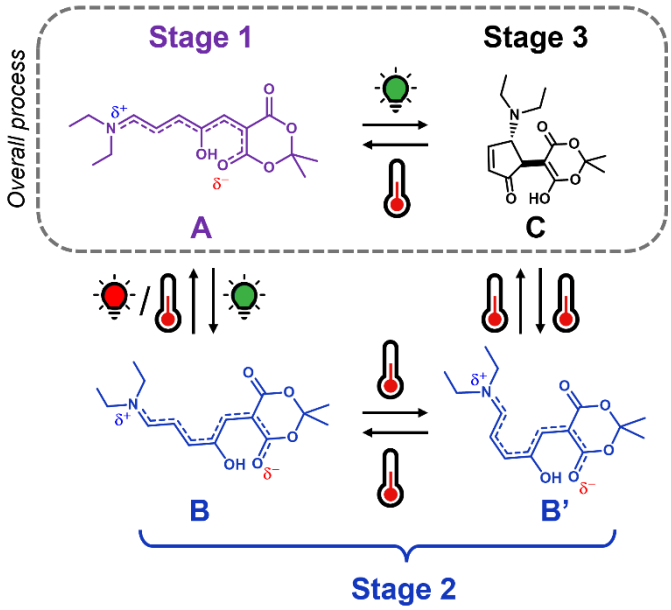

Fig. 3.1. Structure for the first generation DASA molecule used in this study and the proposed 3 stage mechanism of photoswitching.

3.2.2. Spectroscopic characterization

Broadband transmission measurements were performed with an Ocean Optics USB4000 UV-Vis spectrometer from approximately 300 nm-800 nm using a fiber-coupled

deuterium halogen broadband probe light (Mikropack DH-2000-BAL) and LabVIEW-controlled data acquisition. The **A** and **B**/**B'** isomers were optically pumped with a fiber-coupled 532 nm Nd:YAG laser (Q-BAIHE), outfitted with cleanup optics to remove residual infrared radiation, and a pair of 620 nm LEDs (Cree XLamp in color red-orange), respectively. The LEDs were angled and focused to intersect at the sample surface for maximum power, and the LED current loads were metered with a power supply. A solenoid-powered beam flag was used to control the 532 nm beam exposure time while the 620 nm LEDs were electrically gated. Both were controlled using LabVIEW (National Instruments BNC-2110). Every 5 s, optical pumping was paused for approximately 70 ms before collecting transmission spectra. Signal integration was performed over the subsequent 30 ms before resuming irradiation. The initial 70 ms delay time was necessary to accommodate the mechanical delay of the 532nm beam flag, preventing contamination of the transmission measurement with scattered pump light. Emission profiles for the photoexcitation sources are overlaid with the **A** absorption profiles for DASA in toluene, PBMA, and PMMA in Fig. 3.2.[8,9]

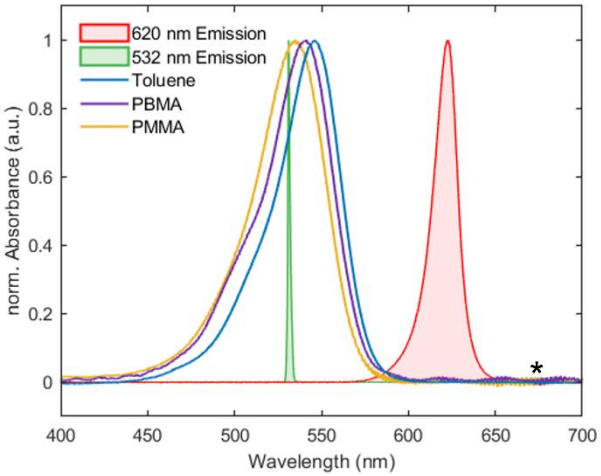

Fig. 3.2. Normalized absorbance profiles of for the **A** isomer pictured in Fig. 3.1 in toluene (blue), PBMA (violet), and PMMA (yellow), showing a modest blue shift in more polar environments according to their respective Hansen polar solubility parameters (δ_P = 1.4 (toluene), 5.5 (PBMA), and 10.5 (PMMA))[9]. This is in line with the negative solvatochromatic slope measured for first generation DASA in ref. 8. Etalon fringes (*) are observed in the PBMA and PMMA film absorbance spectra because of thin film interference.

Frequency modulated pump probe spectroscopy was performed according to the method outlined in Section 2.2 with the same 532 nm and 620 nm light sources used to pump and probe **A** and **B/B'**, respectively. To accomplish this, a glass slide was used to reflect a portion of the continuous wave (CW) 532 nm pump beam, which was mechanically chopped at 506 Hz and passed into an optical fiber. A third 620 nm LED, spectrally identical to the two 620 nm pump LEDs, was driven with a 2.3 kHz square wave (33120A 15 MHz Function Generator, Agilent Tech.) and coupled into the same fiber as the 532 nm probe beam. The resulting beam was passed through the sample, and the transmitted intensities of the 532 nm and 620 nm probe beams were measured according to Section 2.2. A schematic illustration of the FMPPS technique can be found in Fig. 2.1.

For both broadband and FMPPS UV-Vis measurements, film samples were cut to approximately 1 cm x 1 cm squares and adhered using double stick tape to a removable sample puck. The DASA-loaded layer was oriented normally facing the incident probe beam. The pump beams were introduced off normal by 10^{o}-45^{o}. Solution samples were prepared by pipetting 80 µL into a 1 cm wide glass cuvette with a path length of 1 mm. This volume was used to ensure the entire sample resided in the pump source exposure area and minimized diffusion effects in the observed photoswitching rates.

3.3. Results and discussion

3.3.1. Kinetic model of multistate photoswitching

To account for the fact that the intermediate isomers **B** and **B'** were spectroscopically indistinguishable from one another in the visible regime, a reduced form of the four-stage model illustrated in Fig. 3.1 was proposed, designed to account only for the three stages that were photochemically distinct: stage 1 (**A**), stage 2 (**B** and **B'**), and stage 3 (**C**). Stage 1 was assumed to exclusively contain the linear form, triene isomer, **A**, and could be converted to

stage 2 by actinic E/Z isomerization. Stage 2 contained both short-lived intermediates **B** and **B'** and could either thermally proceed through a 4π electrocyclization to stage 3 or decay back to stage 1. The reverse isomerization to regenerate stage 1 could be accelerated by leveraging a parallel actinic pathway promoted under the irradiation of stage 2. Stage 3 contained all non-absorbing, closed form isomers and could slowly reform stage 2 in solution or persist as a kinetically trapped state in polymer blends.

To ensure clarity while keeping consistent terminology with traditional 2-stage DASA models, photoisomerization must be differentiated from photoswitching, where the former refers to the single step actinic interconversions of **A** and **B**, while the latter refers to the loss of absorbance (as measured by the absorbance of stage 1) with the net conversion of stage 1 to stage 3 under irradiation. By this convention, photoswitching could occur either by "single wavelength" exposure to address stage 1 in isolation or by "dual wavelength" exposure to simultaneously address stages 1 and 2. Addressing stage 2 during photoswitching allowed for photokinetic control in the switching rate by promoting the reformation of stage 1 from stage 2 and slowing the production of stage 3 as a result. Throughout this work, stages 1 and 2 were excited with a 532 nm laser and a 620 nm LED, respectively. Emission profiles for these light sources are overlaid with the absorbance profiles of DASA in toluene, PBMA, and PMMA in Fig. 3.2 and were selected among those commercially available to maximize absorptivity of the desired stage while minimizing overlap with the opposing stage.

3.3.2. Dual wavelength multistate DASA control in polymer blends

To determine the degree of photokinetic control achievable in PBMA, PMMA, and toluene, the rate of photoswitching was measured by UV-Vis absorption spectroscopy and compared when optically pumping only stage 1 (532 nm, 9.2 mW/cm^2) and when pumping stages 1 and 2 simultaneously (532 nm: 9.2 mW/cm^2 and 620 nm: 78 mW/cm^2). Samples were

selected to limit variability in the initial absorbance at the stage 1 excitation wavelength (532 nm) to ensure the measured photoswitching rates depended only on the photochemical reactivity of DASA and not on the position of λ_{max} in the polymer/solvent. This approximation was considered to be valid if the photochemical isomerization efficiencies of **A** to **B** and **B** to **A** were wavelength independent, which was predicted on the basis of Kasha's rule (*cf.* Section 1.2). Based on the results of this study, presented in Fig. 3.3, it was determined that while addressing stage 2 with a secondary wavelength of light resulted in a marked deceleration in the rate of photoswitching in toluene, polymer blends of DASA in PBMA and PMMA were less receptive to photokinetic control. In fact, DASA in PMMA displayed no discernable kinetic effect induced by photochemically addressing stage 2 during photoswitching.

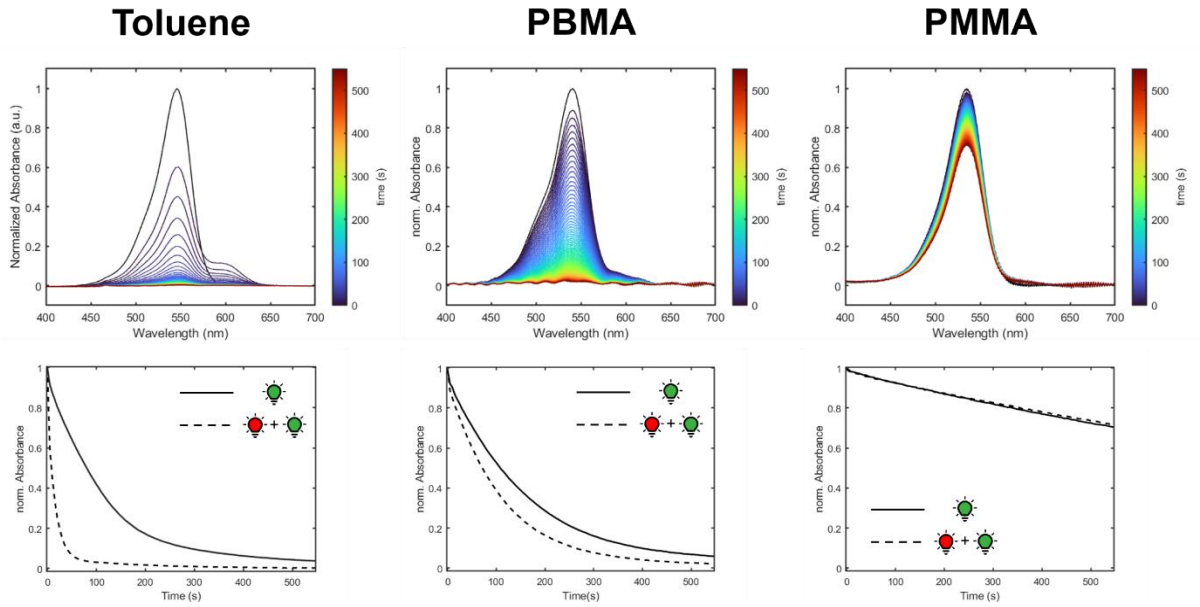

Fig. 3.3. Normalized spectra (top) and peak absorbance (bottom, dashed) measured during optical pumping of stage 1 alone in toluene (0.0179 mM, left), PBMA (1 wt%, center), and PMMA (1 wt%, right). Under simultaneous irradiation of stage 1 and stage 2, the rate of photoswitching (bottom, solid) slowed measurably in toluene and PBMA but not in PMMA.

Isolating the cause of the diminished photokinetic control demonstrated in PBMA and PMMA required a greater understanding of the stage 2 formation and decay kinetics in each host medium. To facilitate this exploration, FMPPS (described in Section 3.2.2) was performed

to track the rapid interchange of isomers in stages 1 and 2 that occurred to establish a dynamic equilibrium under irradiation of stage 1. This technique was well suited to measuring this process because the exposure times required to reach equilibrium, as indicated by the end of stage 2 accumulation, were between 0.1 and 1 s, depending on the DASA host environment. The shortened time scale for this process as compared to the several minutes required for photoswitching necessitated a spectroscopic method with greater temporal resolution than the traditional UV-Vis technique used in Fig. 3.3 to monitor photoswitching. In addition, the absorbance of stage 2 at pseudo-equilibrium with stage 1 during photoswitching was significantly reduced in PMMA and PBMA compared to toluene. These two constraints made the improved temporal resolution and sensitivity of FMPPS ideal for observing **B/B'** in all three environments.

The results of this experiment are provided in Fig. 3.4 and, when compared with photoswitching kinetics presented in Fig. 3.3, suggested an intuitive positive correlation between the amount of stage 2 accumulated during photoswitching and the ability to control the rate of photoswitching by optically pumping stages 1 and 2. As evidence of this, the sample of DASA in toluene accumulated the greatest population of stage 2 under irradiation and, as a result, displayed the greatest capacity for three state reactivity. In contrast, DASA in PBMA accumulated stage 2 to a lesser extent and showed only slight three-state reactivity. In PMMA, DASA behaved as a purely binary switch, presumably because the stage 2 population present during switching was too low to appreciably deplete photochemically without increasing the optical flux.

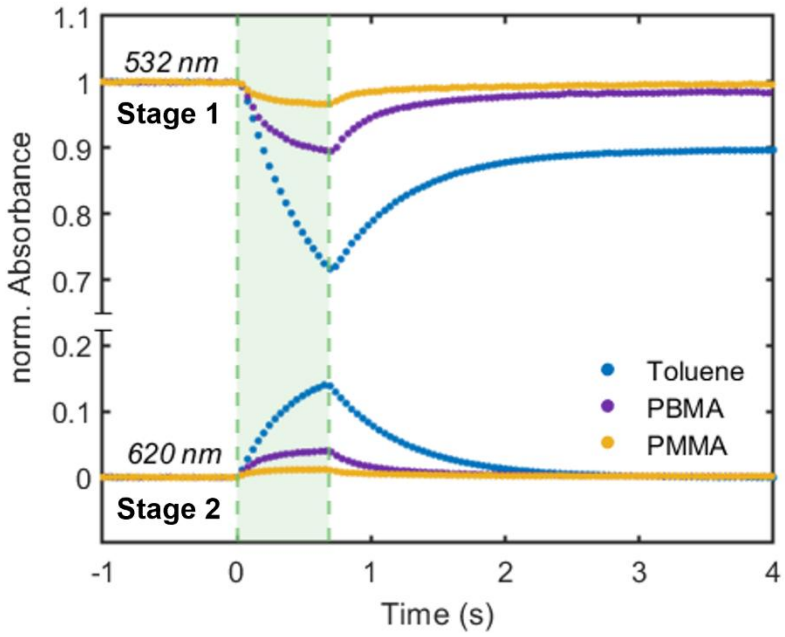

Fig. 3.4. Comparing photoisomerization rates in toluene (0.0179 mM, blue), PBMA (1 wt%, violet), and PMMA (1 wt%, orange) during 600 ms of pumping with 24 mW/cm^2 of 532 nm hv. Exposure time highlighted in green. The top three traces correspond to the stage 1 absorbances (532 nm) while the bottom three correspond to stage 2 (620 nm). For visualization, all three data sets were normalized to their initial stage 1 absorbances.

3.3.3. Thermal and photochemically accelerated stage 2 decay rates

The relationship between the pseudo-equilibrium population of stage 2 and the capacity for dual wavelength, multistate control was identified previously by Stricker and coworkers for two different DASA structures in solution.[10] They attributed the diminished capacity for three state reactivity in some DASAs to their comparatively shorter stage 2 thermal lifetimes. Applying this reasoning to the results observed in Fig. 3.4, the lower stage 2 concentrations sustained during photoswitching in PBMA and PMMA would have resulted from a destabilization of stage 2 in polymers compared to the native case in toluene. However, this explanation seems unlikely because it implies that the decay of stage 2 was accelerated in polymeric hosts, despite the relative lack of mobility in solids. More likely, the pseudo-equilibrium concentration of stage 2 was reduced in PBMA and PMMA because of a drop in the **A** to **B** photoisomerization efficiency that resulted in slower stage 2 formation kinetics. This

hypothesis is in line with the results of similar studies showing a drop in the photoisomerization efficiency of azobenzene[11–14] and indigo[15] photoswitches in amorphous polymers compared to the solution state. This hypothesis is also supported by Lerch et al., who saw a drop in the **A** to **B** isomerization efficiency for the same DASA used here in DMSO compared to methanol.[2] This drop was attributed to the increase in solvent viscosity.

To validate this hypothesis, FMPPS was used to quantify the thermal decay rates of stage 2 in PBMA, PMMA, and toluene. In this experiment, stage 2 was populated with a brief pulse of 532 nm light and the subsequent decay kinetics were fit to the rate law in equation 3.1 to determine the effective decay rate constant, k_{eff}. This rate constant was defined according to equation 3.2 and includes the combined rate constants associated with the reverse isomerization of **B/B'** back to **A** and the thermal isomerization forward to **C** (k_2). The **B/B'** to **A** isomerization rate constant is further broken down into thermal (k_{-1}) and photochemical components, where q_{620nm}, Φ, and ε_2 denote the photon flux, the reaction quantum efficiency, and the molar absorptivity of stage 2, respectively, associated with the 620 nm LED used to optically pump stage 2. The absorbance as a function of elapsed time, t, after the end of the 532 nm pump pulse is given as A_2 (t). This kinetic model was exclusively valid in the low absorbance limit of stage 2 ($A_2 < 0.04$ a.u.) and is derived in detail elsewhere†.

$$ln\left(\frac{A_2\,(t)}{A_2\,(t=0)}\right) = -k_{eff}t \tag{3.1}$$

$$k_{eff} = \epsilon_2 q_{620nm}\Phi + k_{-1} + k_2 \tag{3.2}$$

Thermal and photochemically accelerated stage 2 decay curves are provided in Fig. 3.5 for DASA in toluene, PBMA, and PMMA. All host media were observed to support a photochemical pathway to reform stage 1, indicated by accelerated stage 2 decay with

† The full derivation of equation 3.2 is provided in the supplemental file of ref. 1.

increasing fluxes of 620 nm light. However, this technique neglected to consider the effects of reflectance and scattering, making it challenging to extract and compare the isomerization quantum yields in each medium.

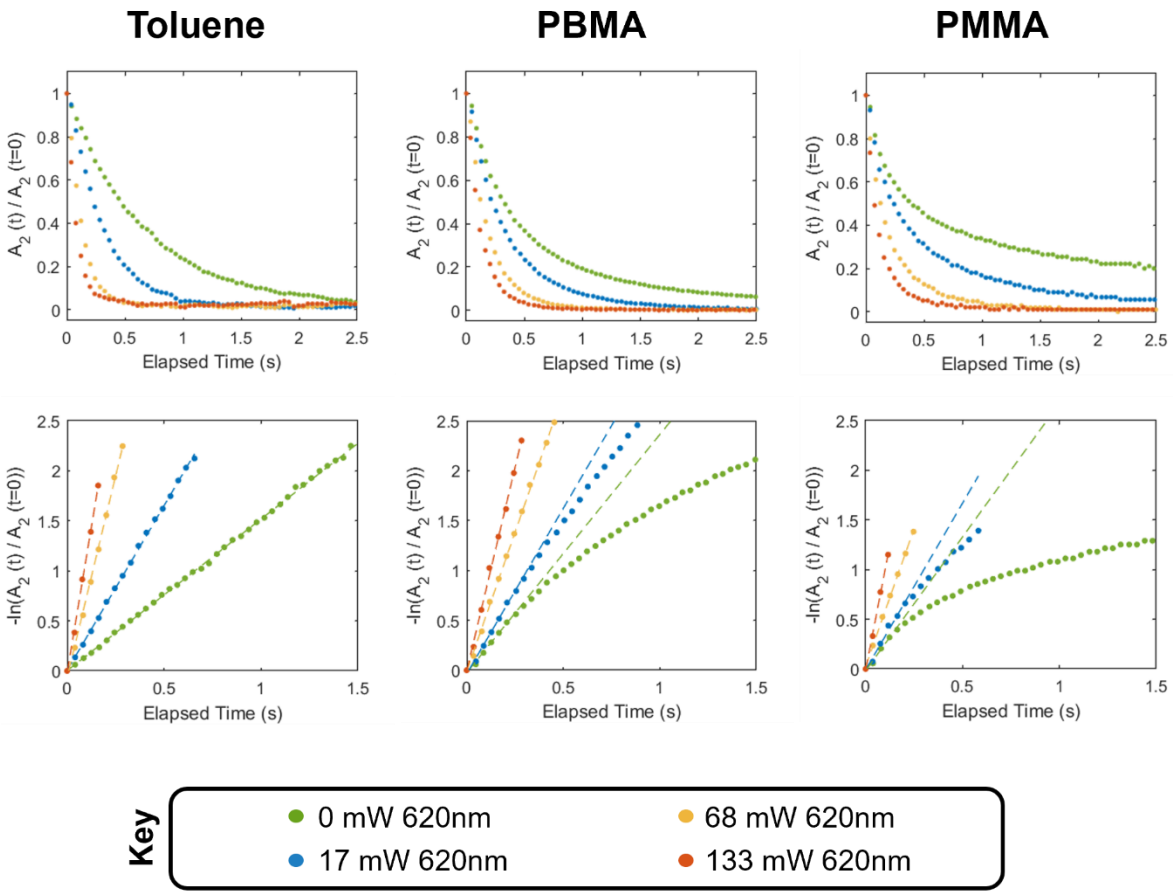

Fig. 3.5. Photochemical and thermal decay of DASA in stage 2 after a pulse of 532 nm light in toluene (left), PBMA (center), and PMMA (right). DASA loadings were the same as those indicated in Fig. 3.4. The normalized absorbance of the 620 nm probe source used as a proxy for the stage 2 absorbance (top) and the normalized absorbance was used to calculate first order linearized decay plots (bottom). The 620 nm pump intensity during stage 2 decay was varied according to the key and the pump exposure area was held constant at approximately 1.7 cm^2.

Effective decay rate constants were extracted from the stage 2 linearized decay curves by least squares regression and are presented as a function of the 620 nm pump power during decay in Fig. 3.6. For curves that deviated from linearity, specifically the thermally dominated decay plots in PBMA and PMMA, the effective rate constants were determined from a linear

fit applied in the short time, linear regime. This deviation from first order decay kinetics in PBMA and PMMA is interesting and may indicate the presence of the same biphasic kinetic regimes driven by diffusion-limited mechanical confinement of azobenzene in polycarbonate, PS, and various polymethacrylates.[13,14,16–18] However, the time scales associated with the thermal decay of **B/B'** (~ s) are significantly shorter than those observed for the thermal cis-to-trans isomerization of azobenzene (~ min). This suggests that the emergence of nonlinear kinetics, if it can be explained by microstructural heterogeneity, is not a direct consequence of the isomerization time scale relative to the time scale associated with the polymer chain dynamics. Instead, the polymers with greater chain mobility should result in a smoother transition from freely mobile to diffusion limited kinetics and overall faster isomerization in the diffusion limited regime. However, it is not immediately clear from this data whether the deviation from first order kinetics is associated with the thermal decay of **B/B'** to **A** or isomerization **C** because the effective decay rate constant, k_{eff}, is a combination of both. To separate these two rate constants, a way to measure the molar absorptivities of **A** and **B/B'** at their respective probe wavelengths would be required. Alternatively, the deviation from first order kinetics in PBMA and PMMA may have resulted from these environments favoring different thermal isomerization pathways to generate additional DASA isomers not accounted for in this 3-state model, including those reported by Zulfikri et al.[19] These isomers would have been spectroscopically indistinguishable from stages 1 and 2, making this hypothesis impossible to prove by visible absorbance measurements alone.

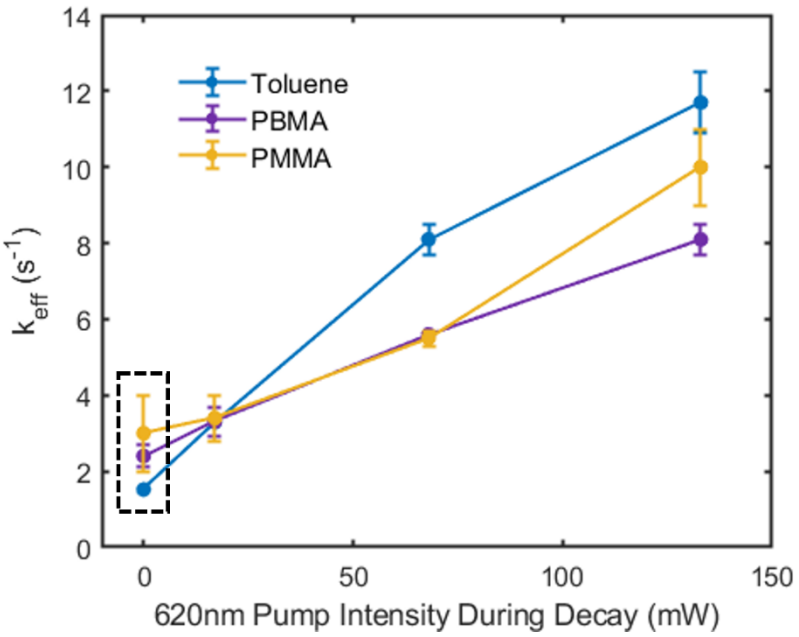

Fig 3.6. Stage 2 decay rate constant, k_{eff} (see equation 3.2), computed from the curves in Fig. 3.5 vs. incident pump power. Strictly thermal decay rate constants are indicated with a gray dashed box. The 620 nm pump exposure area was approx. 1.7 cm^2.

Comparing the extracted decay rate constants, the strictly thermal decay rates (boxed in Fig. 3.6) were found to be surprisingly similar in toluene, PBMA, and PMMA (1.52 ± 0.02 s^{-1}, 2.4 ± 0.3 s^{-1}, and 3 ± 1 s^{-1}, respectively). This result supported the initial hypothesis that the lower pseudo-equilibrium stage 2 populations in PBMA and PMMA were the result of slower **A** to **B** conversion, rather than accelerated thermal decay. While it seems likely that this reduction in quantum efficiency was the result of viscous forces opposing bond rotation in the polymer systems, specifically in glassy PMMA, the different molecular structures of toluene, PBMA, and PMMA make it challenging to disentangle mechanical factors from the effects of polarity. Coincidentally, any polarity-induced changes to the DASA PES are expected to result in a similar drop in the **B/B'** population during photoswitching, with PMMA being the most polar environment and toluene being the least.

In addition to slowing the actinic rate of stage 2 formation, polymeric hosts were found to prevent thermal regeneration of stage 2 from stage 3 after complete or partial

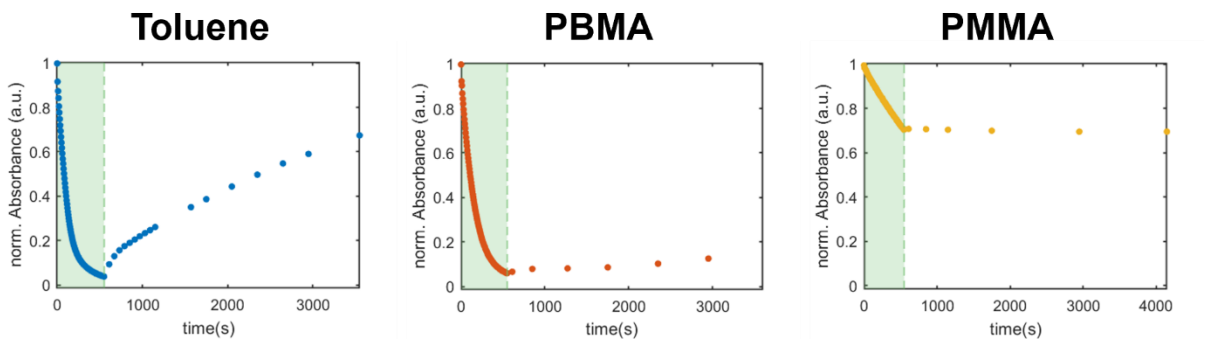

Fig. 3.7. Stage 1 photoswitching (shaded green) and thermal dark recovery kinetics for DASA in toluene (0.0179 mM, left), PBMA (1 wt%, center), and PMMA (1 wt%, right). Absorbances normalized to the initial absorbance of stage 1 at time = 0 s. Photoswitching data in the shaded region is identical to the single wavelength photoswitching data presented in Fig. 3.3.

photobleaching (Fig. 3.7). In contrast, DASA in toluene recovered to approximately 70% of its initial absorbance after 1 hour in the dark following near complete conversion to stage 3. This behavior has been widely reported for first generation DASA derivatives and may have further limited the degree of photokinetic control possible in PBMA and PMMA by ensuring that the formation of stage 3 was an irreversible process.

3.4. Conclusion

Three state photokinetic control of DASA was found to be inhibited in systems that do not favor the accumulation of the intermediate **B** and **B'** species that make up stage 2. This resulted from the high photon fluxes required to photochemically address these dilute species. This phenomenon was found to be directly responsible for the limited and negligible degrees of photokinetic control achievable in PBMA and PMMA, respectively, compared to a solution of DASA in toluene.

To determine the cause of the limited accumulation of stage 2 in these systems, a dynamic, phase-locked spectroscopic technique (FMPPS) was developed and implemented to provide higher sampling speeds and greater sensitivity than standard UV-Vis to probe the photochemical evolution and rapid decay of stage 2. Using FMPPS, polymeric hosts were

found to result in the emergence of nonlinear stage 2 thermal decay kinetics but had minimal effect on the thermal stability of stage 2, measured immediately after pausing optical pumping of stage 1, relative to a solution in toluene. This suggested that the reduction in stage 2 accumulation in PBMA and PMMA compared to toluene resulted primarily from slower actinic **A** to **B** conversion and could likely be attributed to viscous effects, which have been reported previously to influence DASA switching kinetics in polymers.[3,6,7]

One additional factor which may have contributed to the limited accumulation of stage 2 in PBMA and PMMA was the lack of a thermally accessible pathway to regenerate **B'** from **C** during photobleaching. Thermal open form recovery, which occurred slower relative to the preceding isomerizations in toluene, likely provided a small boost in the pseudo-equilibrium stage 2 population established during bleaching in toluene but not in the polymeric hosts. While this study did not consider the possibility of a photochemical pathway in the isomerization of **B'** to **C**, as was suggested by Bieske and coworkers, this may have also contributed slightly to efficacy of dual wavelength photokinetic control by simultaneously accelerating both competing stage 2 decay pathways with the same wavelength of light.[20] If this effect could primarily account for the reduced photokinetic control in PBMA and PMMA, the photochemical stage 2 decay rates constants in Fig. 3.6 would have been expected to increase faster with the intensity of 620 nm light in PBMA and PMMA. However, this was not observed.

While this study successfully identified crucial steps in the overall DASA photobleaching process that result in the observed matrix effects limiting the three-state reactivity in PBMA and PMMA, the underlying reasons for these effects require further study. To that end, additional work is necessary before one can implement a systematic approach to structurally modifying the DASA architectures or host polymers with the objective of offsetting

these kinetic matrix effects and enabling dynamic, three state photoswitching in polymeric hosts.

3.5. References

(1) Sandlass, S.; Stricker, F.; Fragoso, D.; de Alaniz, J. R.; Gordon, M. J. Effect of Polymer Host Matrix on Multi-Stage Isomerization Kinetics of DASA Photochromes. *J Photochem Photobiol A Chem* **2023**, *444*, 114964. https://doi.org/10.1016/j.jphotochem.2023.114964.

(2) Lerch, M. M.; Di Donato, M.; Laurent, A. D.; Medved', M.; Iagatti, A.; Bussotti, L.; Lapini, A.; Buma, W. J.; Foggi, P.; Szymański, W.; Feringa, B. L. Solvent Effects on the Actinic Step of Donor–Acceptor Stenhouse Adduct Photoswitching. *Angewandte Chemie* **2018**, *130* (27), 8195–8200. https://doi.org/10.1002/ange.201803058.

(3) Ulrich, S.; Hemmer, J. R.; Page, Z. A.; Dolinski, N. D.; Rifaie-Graham, O.; Bruns, N.; Hawker, C. J.; Boesel, L. F.; Read De Alaniz, J. Visible Light-Responsive DASA-Polymer Conjugates. *ACS Macro Lett* **2017**, *6* (7), 738–742. https://doi.org/10.1021/acsmacrolett.7b00350.

(4) Mao, L.; Wang, Z.; Duan, Y.; Xiong, C.; He, C.; Deng, X.; Zheng, Y.; Wang, D. Designing of Rewritable Paper by Hydrochromic Donor-Acceptor Stenhouse Adducts. *ACS Nano* **2021**, *15* (6), 10384–10392. https://doi.org/10.1021/acsnano.1c02629.

(5) Szalöki, G.; Sevez, G.; Berthet, J.; Pozzo, J. L.; Delbaere, S. A Simple Molecule-Based Octastate Switch. *J Am Chem Soc* **2014**, *136* (39), 13510–13513. https://doi.org/10.1021/ja506320j.

(6) Sroda, M. M.; Lee, J.; Kwon, Y.; Stricker, F.; Park, M.; Valentine, M. T.; Read de Alaniz, J. Role of Material Composition in Photothermal Actuation of DASA-Based Polymers. *ACS Appl Polym Mater* **2022**, *4* (1), 141–149. https://doi.org/10.1021/acsapm.1c01108.

(7) McDonough, R.; Rudgley, N.; Majewski, O.; Perkins, M. V.; Evans, R. A.; Lewis, D. A. Photochromic Performance of Donor-Acceptor Stenhouse Adducts in Polymer Binders and Solution. *ChemPhotoChem* **2022**, *6* (9). https://doi.org/10.1002/cptc.202200076.

(8) Sroda, M. M.; Stricker, F.; Peterson, J. A.; Bernal, A.; Read de Alaniz, J. Donor–Acceptor Stenhouse Adducts: Exploring the Effects of Ionic Character. *Chemistry - A European Journal* **2021**, *27* (12), 4183–4190. https://doi.org/10.1002/chem.202005110.

(9) Hansen, C. M. *Hansen Solubility Parameters: A User's Handbook*, 2nd ed.; CRC Press: Boca Raton, FL, 2007.

(10) Stricker, F.; Sanchez, D. M.; Raucci, U.; Dolinski, N. D.; Zayas, M. S.; Meisner, J.; Hawker, Craig. J.; Martínez, Todd. J.; Read de Alaniz, J. A Multi-Stage Single Photochrome System for Controlled Photoswitching Responses. *Nat Chem* **2022**. https://doi.org/10.1038/s41557-022-00947-8.

(11) Loucif-Saibi, R.; Nakatani, K.; Delaire, J. A.; Dumont, M.; Sekkat, Z. *Photoisomerization and Second Harmonic Generation in Disperse Red One-Doped and-Functionalized Poly (Methyl Methacrylate) Films*; 1993; Vol. 5. https://pubs.acs.org/sharingguidelines.

(12) Sekkat, Z.; Morichère, D.; Dumont, M.; Loucif-Saïbi, R.; Delaire, J. A. Photoisomerization of Azobenzene Derivatives in Polymeric Thin Films. *J Appl Phys* **1992**, *71* (3), 1543–1545. https://doi.org/10.1063/1.351228.

(13) Mita, I.; Horie, K.; Hirao, K. *Photochemistry in Polymer Solids. 9. Photoisomerization of Azobenzene in a Polycarbonate Film*; 1989; Vol. 22. https://pubs.acs.org/sharingguidelines.

(14) Ta-Li Chen, D.; Morawetz, H. Photoisomerization and Fluorescence of Chromophores Built into the Backbones of Flexible Polymer Chains. *Macromolecules* **1976**, *9* (3), 463–468.

(15) Kuntze, K.; Viljakka, J.; Virkki, M.; Huang, C. Y.; Hecht, S.; Priimagi, A. Red-Light Photoswitching of Indigos in Polymer Thin Films. *Chem Sci* **2023**, *14* (10), 2482–2488. https://doi.org/10.1039/d2sc06790k.

(16) Eisenbach, C. D. Effect of Polymer Matrix on the Cis - Trans Isomerization of Azobenzene Residues in Bulk Polymers . *Die Makromolekulare Chemie* **1978**, *179* (10), 2489–2506. https://doi.org/10.1002/macp.1978.021791014.

(17) Eisenbach, C. D. Relation between Photochromism of Chromophores and Free Volume Theory in Bulk Polymers. *Berichte der Bunsengesellschaft für physikalische Chemie* **1980**, *84* (7), 680–690. https://doi.org/10.1002/bbpc.19800840714.

(18) Victor, J. G.; Torkelson, J. M. On Measuring the Distribution of Local Free Volume in Glassy Polymers by Photochromic and Fluorescence Techniques. *Macromolecules* **1987**, *20*, 2241–2250.

(19) Zulfikri, H.; Koenis, M. A. J.; Lerch, M. M.; Di Donato, M.; Szymański, W.; Filippi, C.; Feringa, B. L.; Buma, W. J. Taming the Complexity of Donor-Acceptor Stenhouse Adducts: Infrared Motion Pictures of the Complete Switching Pathway. *J Am Chem Soc* **2019**, *141* (18), 7376–7384. https://doi.org/10.1021/jacs.9b00341.

(20) Bull, J. N.; Carrascosa, E.; Mallo, N.; Scholz, M. S.; Da Silva, G.; Beves, J. E.; Bieske, E. J. Photoswitching an Isolated Donor-Acceptor Stenhouse Adduct. *Journal of Physical Chemistry Letters* **2018**, *9* (3), 665–671. https://doi.org/10.1021/acs.jpclett.7b03402.

Chapter 4

Mechanical confinement-induced optical anisotropy in chromophore-functionalized liquid crystal polymers

Adapted from the following publications:

1. Guillen Campos, J.; Tobin, C.; **Sandlass, S.**; Park, M.; Wu, Y.; Gordon, M.J.; Read de Alaniz, J., Photoactivation of Millimeters Thick Liquid Crystal Elastomers with Broadband Visible light Using Donor-Acceptor Stenhouse Adducts. *Adv. Mater.*, **36**, 2404932 (2024).

2. Guillen Campos, J.; Park, M.; Wu, Y.; **Sandlass, S.**; Novikov, I.; Bailey, S.J.; Timofeeva, T.; Read de Alaniz, J.G. Synthesis of Photoresponsive Liquid Crystal Elastomers: A General Chemical Approach. *J. Mater. Chem. A.* (2025). (submitted)

This chapter explores the effect of mechanical confinement on DASA-functionalized polymers from a different perspective than was discussed in Chapter 3. Instead of focusing on the effect of confinement on the DASA PES, which controls the rate of isomerization, this chapter focuses on confinement-induced optical anisotropy of DASA and other chromophores when incorporated into liquid crystal elastomers using the novel late-stage functionalization technique introduced by Campos et al.[1,2] To facilitate this analysis, polarized light absorbance spectroscopy was performed both with and without frequency modulation. The former was used to measure the order parameters of different chromophores when incorporated in LCEs while the latter was based on a modified version of FMPPS compared to chapters 2 and 3 and used to dynamically measure the reorientation of DASA in LCEs subjected to compressive stress.

4.1. Introduction

Liquid crystal elastomers (LCEs/LCPs/LCNs) have garnered significant attention in recent years for their ability to convert work done on a molecular level during isomerization into bulk macroscopic strains for applications in actuation. This mechanism provides a route to converting energy from light into work using a photoswitch-functionalized LCE without requiring an intermediate step converting light into heat. This enables actuation with greater spatial control than would be possible via photothermal actuation and facilitates actuation in environments with non-ideal thermodynamic properties (e.g., underwater) (*cf.* Section 1.4.1.2).

Photoswitches in LCEs are subject to the effects of mechanical confinement (*cf.* Section 1.3.3), resulting in reduced photoisomerization quantum yields compared to the solution state and less efficient actuation as a result.[3] However, because the LCE has a high degree of structural anisotropy, the forces associated with mechanical confinement in these

systems tend to result in preferential alignment of the embedded photoswitches along the material alignment axis (i.e.. nematic director). The degree of photoswitch alignment is reflected in the material order parameter, S, which is defined in Song and Kim[4] and is reproduced in equation 4.1 below in terms of the sample absorbance measured when the polarization angle is aligned ($A_{\parallel}$) and normal ($A_{\perp}$) to the material alignment axis. The order parameter depends on the angle between the photoswitch's molecular alignment direction (M) and dipole transition moment (T) as well as the spatial distribution in M throughout the bulk material (see Fig. 4.1). Photoswitch-functionalized LCEs with an order parameter close to 1 or -0.5 preferentially absorb light that is parallel or perpendicular to the material alignment axis, respectively. As a result, the photochemical isomerization efficiency and the resulting actuation efficiency depends strongly on the polarization angle of the light used to drive actuation.

$$S = \frac{A_{\parallel} - A_{\perp}}{A_{\parallel} + 2A_{\perp}} \tag{4.1}$$

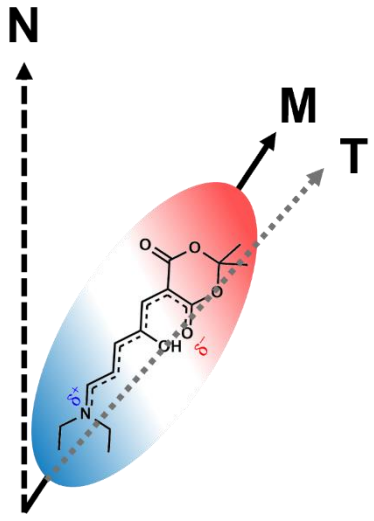

Fig. 4.1. Geometry of DASA showing the molecular alignment axis (M) and transition dipole moment (T) relative to the bulk material alignment axis (N).

4.2. Measuring the order parameter for chromophore-functionalized LCEs

Recently, Campos et al. developed a universal late-stage approach to functionalizing LCEs with photo-responsive molecules (PRMs) that would otherwise not survive the nucleophilic addition or free radical reaction conditions needed to crosslink the LCE.[1,2] Their approach was based on the incorporation of a furan click handle into LCEs synthesized by Finklemann's two-stage hydrosilylation method. After crosslinking, PRMs functionalized with maleimide click handles were incorporated into the LCE via a Diels-Alder cycloaddition reaction with the furan handles in the host polymer. Their synthetic approach is summarized schematically in Fig. 4.2.

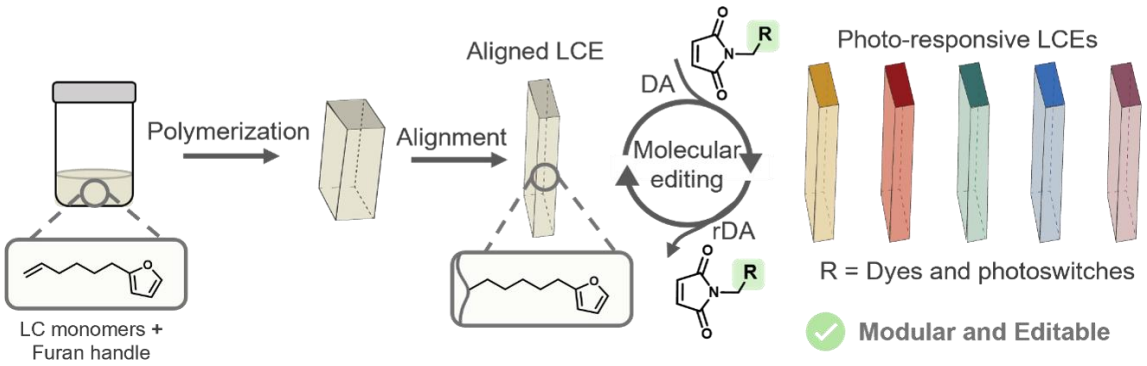

Fig. 4.2. Late-stage functionalization of LCEs with PRMs using Diels-Alder click chemistry. Reproduced from ref. 2.

Existing methods for fabricating PRM-functionalized LCEs, which involve incorporating the PRM before crosslinking, often lead to a significant anisotropy in the orientation of the embedded PRMs. This anisotropy is reflected by a non-zero order parameter (see equation 4.1). To determine whether this structural anisotropy is retained in the post-functionalization technique of Campos et al., the PRM absorbance was measured as a function of the angle formed between the polarization axis of the light and the LCE alignment axis. Five different LCEs were tested, each functionalized with a different PRM. These five PRMs included two UV active PRMs (UV azobenzene and spiropyran) and three visible light active PRMs (red

azobenzene, blue cyanine dye, and a third generation DASA). Their chemical structures along with their unpolarized UV-Vis absorbance spectra are provided in Fig. 4.3.

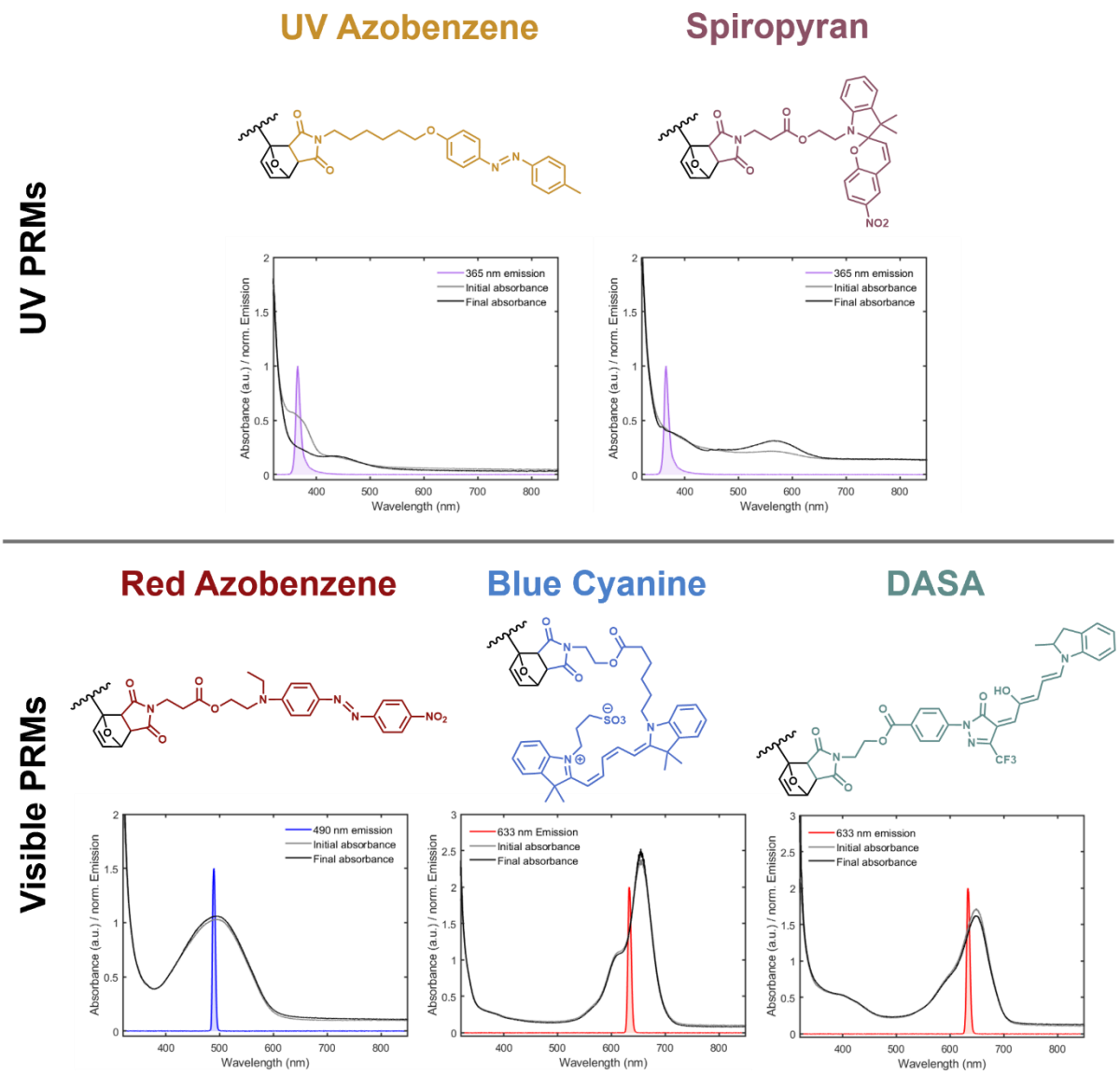

Fig. 4.3. PRM structures explored in this study along with their UV-Vis absorbance spectra before (grey) and after (black) measuring their order parameters to check for photoswitching. PRMs are separated into UV (top) and visible (bottom) absorbing. Emission profiles for the lights used to measure order parameter are overlaid on the corresponding absorbance spectra.

To measure the angle dependent absorbance of the visible absorbing PRMs (Fig. 4.3, bottom), a pulsed (78 MHz) unpolarized supercontiuum laser (SuperK Fianium, NKT

Photonics) was filtered with a tunable filter (SuperK Varia, NKT Photonics) to generate a narrow bandwidth unpolarized light source with significant spectral overlap with the PRM absorbance profile. For the UV absorbing PRMs (Fig. 4.3, top), an unpolarized 365 nm LED was used to measure absorbance. In both the UV and visible absorbing cases, the light used to measure the sample absorbance was linearly polarized and the sample transmittance was measured using a UV-enhanced amplified detector (Thorlabs, PDA36A). To measure absorbance as a function of angle, the sample was rotated on a custom-built motorized stage at a fixed speed of 1° per second and the absorbance as a function of time was measured and converted to a function of angle from the known rotation speed. These results are plotted in Fig. 4.4 for the five different PRMs tested. The emission profiles for the light sources used to perform these measurements are overlaid with the absorbance profiles of their associated PRM-functionalized LCEs in Fig. 4.3.

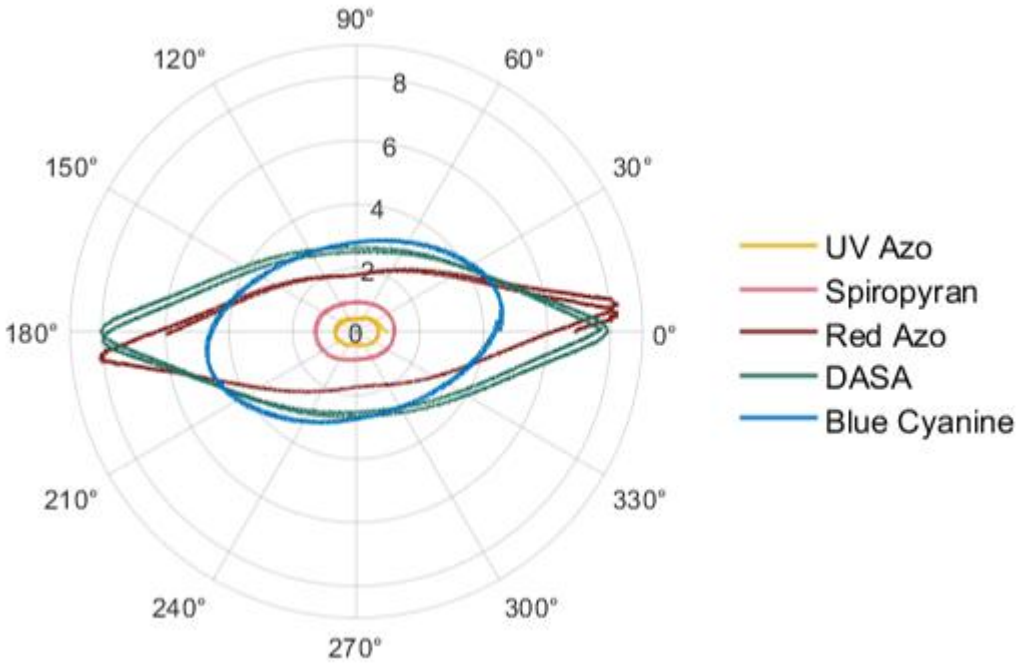

Fig. 4.4. Angle dependent PRM-LCE absorbances measured at the emission wavelengths plotted in Fig. 4.3 for each PRM. 0° and 180° correspond to the polarization axis aligned with the material alignment axis. Slight rotation in the red azo and blue cyanine traces results from imperfect estimates of their LCE alignment axes.

From the angle dependent absorbance profiles plotted in Fig. 4.4, the order parameter for each PRM-LCE was calculated according to equation 4.1. These order parameters are plotted against one another in Fig. 4.5 and showed at least a small degree of alignment for all five PRMs tested, indicated by S > 0. DASA and red azobenzene PRMs were associated with the highest degree of absorbance anisotropy, which intuitively agrees with their long rod-like structures that would pack well with adjacent LCE mesogens (see Fig. 4.3). These results indicate that the late-stage functionalization technique of Campos et al. is similar to existing in-situ functionalization techniques with respect to the anisotropic confinement of certain PRMs in the LCE.

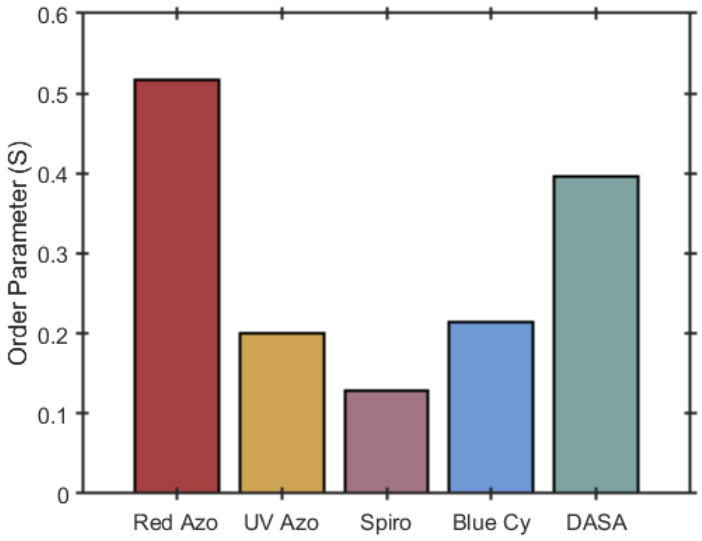

Fig. 4.5. Order parameters computed according to Equation 4.1 measured for LCEs functionalized with the five different PRMs illustrated in Fig. 4.3.

4.3. Effect of compressive stress on the order parameter of DASA-functionalized LCEs

As evidenced by the order parameters plotted for PRM functionalized LCEs in Fig. 4.5, organic dyes typically exhibit strongly dichroic optical properties on a molecular level. This behavior allows them to serve as optical indicators for stress-induced alignment in media that favor a particular molecular orientation.[5] Compared to mechanochromic dyes, which rely on

a mechanically activated isomerization or de-aggregation event to generate an optical response in the form of a color change[6], significantly less stress is required to illicit an optical response by aligning a dichroic dye along a local stress gradient. The increased force sensitivity of dichroism-based optomechanical detection is essential for detecting directed forces generated in dye-doped liquid crystals[7] or during Couette flow of fibers or oligomers in low-viscosity solutions[8].

To demonstrate how FMPPS can be used to measure the stress induced ordering of dichroic molecules, a DASA functionalized LCE prepared using the late-stage functionalization approach described in Section 4.2 was subjected to compressive stress and the change in order parameter was measured. This was achieved using a modified version of the FMPPS technique described in Section 2.2 and used chapters 2 and 3. In the approach used here, optical modulation was used to encode the polarization of two orthogonally polarized but spectrally identical 532 nm probe beams. This enabled the LCE absorbance parallel ($A_{||}$) and perpendicular ($A_{\perp}$) to the nematic director to be measured simultaneously, unlike the technique used to measure S in Section 4.2, which required the sample to be rotated to measure the angle dependent absorbance. The only other difference between this FMPPS technique and the one described in Section 2.2 was that the probe lights were not coupled into an optical fiber before passing through the sample to ensure their polarizations were retained. The DASA structure and the DASA-LCE absorbance spectrum overlaid with the 532 nm emission line are provided in Fig. 4.6.

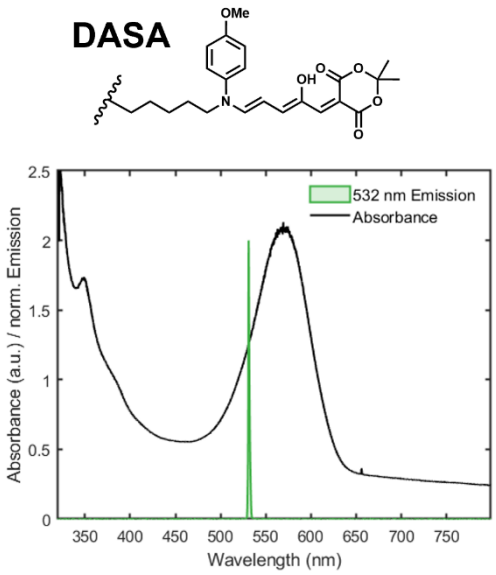

Fig. 4.6. Structure of the LCE-functionalized second generation DASA studied in Section 4.3 (top) and its corresponding absorbance spectrum overlaid with the 532 nm emission profile used to measure the DASA order parameter (bottom).

The LCE films were compressed normal to their alignment axis using a custom-built hydraulically loaded mechanical testing apparatus, schematically illustrated in Fig. 4.7. A standard manual hydraulic jack was used to compress the film between two glass slides and the resulting force was measured with a 50 kg S-type load cell (CALT DYLY-103-50kg), amplified with a Vishay model 2310 signal conditioning amplifier. To ensure the force was distributed evenly across the sample, the bottom translating compression plate was mounted on a vertical sliding rail system. This compression plate was hollow at the top to accommodate the probe beam, which was reflected off a 45° mirror through the plate and into the sample. The transmitted beam was passed through an opening in the top static compression plate and fiber coupled into the FMPPS detector, which is described in detail in Section 2.2. The film absorbance and loading force were measured in LabVIEW during manual loading until the glass slides shattered or the maximum loading force (50 kg) was reached.

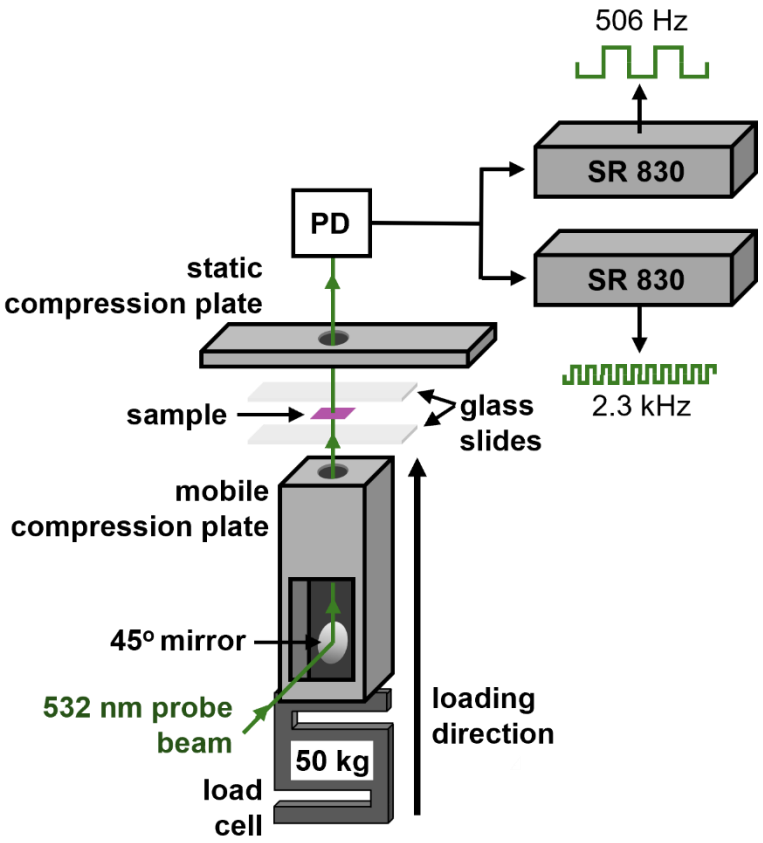

Fig. 4.7. Schematic diagram of the mechanical testing apparatus used in this work.

Interestingly, the results of this experiment, plotted in Fig. 4.8, indicated that the stress induced alignment of DASA in LCEs occurred in three distinct regimes. In the low stress regime (< 0.5 MPa), biaxial tension forces result in a net drop in the order parameter, likely because of a slight rotation in the nematic director in the compression plane due to shear forces experienced between the LCE film and the glass slides. At intermediate forces (0.5 - 4 MPa), the order parameter increases and exceeds the zero-force value. This can be attributed to the reorientation of DASA molecules away from the compression axis to lie in the measurement plane. As the force continues to increase, the order parameter plateaus, indicating that the LCE structure is mostly stable from roughly 4 MPa to 8 MPa — the failure point of the glass.

As the photoactive LCE research field continues to mature in the coming years, future efforts may be necessary to provide a more mechanistically descriptive rational for this non-monotonic change in the order parameter of DASA functionalized LCEs. In addition, it would be interesting to see if these results can be replicated with other PRMs and if a correlation can be found between the geometry and transition dipole moment of the PRM and the stress-induced change in order parameter.

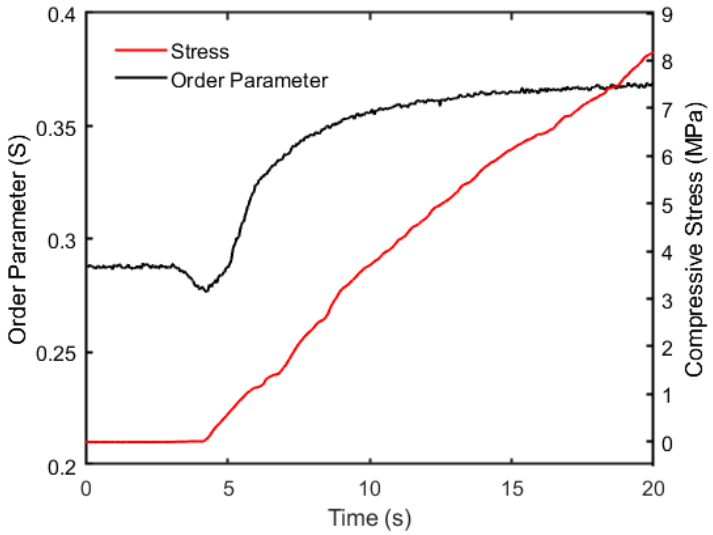

Fig. 4.8. Order parameter of a DASA functionalized LCE defined according to equation 4.1 (black, left axis) as a function of time during compressive loading (red, right axis).

4.4. References

(1) Guillen Campos, J.; Tobin, C.; Sandlass, S.; Park, M.; Wu, Y.; Gordon, M.; Read de Alaniz, J. Photoactivation of Millimeters Thick Liquid Crystal Elastomers with Broadband Visible Light Using Donor–Acceptor Stenhouse Adducts. *Advanced Materials* **2024**, *36* (35). https://doi.org/10.1002/adma.202404932.

(2) Guillen Campos, J.; Park, M.; Wu, Y.; Sandlass, S.; Novikov, I.; Bailey, S. J.; Timofeeva, T.; Read de Alaniz, J. G. *Synthesis of Photoresponsive Liquid Crystal Elastomers: A General Chemical Approach*; 2025.

(3) Kuenstler, A. S.; Hayward, R. C. Light-Induced Shape Morphing of Thin Films. *Current Opinion in Colloid and Interface Science*. Elsevier Ltd March 1, 2019, pp 70–86. https://doi.org/10.1016/j.cocis.2019.01.009.

(4) Song, D. H.; Kim, J. P. Effect of Transition Moments and Orientational Behavior of Dichroic Dyes on the Optical Anisotropy of Poly(Vinyl Alcohol) Polarizing Films. *Dyes and Pigments* **2009**, *80* (2), 219–225. https://doi.org/10.1016/j.dyepig.2008.07.007.

(5) Kurucsev, T.; Kubista, M. Linear Dichroism Spectroscopy of Nucleic Acids. *Q Rev Biophys* **1992**, *25* (1), 51–170. https://doi.org/10.1017/S0033583500004728.

(6) Jiang, Y. An Outlook Review: Mechanochromic Materials and Their Potential for Biological and Healthcare Applications. *Materials Science and Engineering C* **2015**, *45*, 682–689. https://doi.org/10.1016/j.msec.2014.08.027.

(7) Yasarawan, N.; Van Duijneveldt, J. S. Dichroism in Dye-Doped Colloidal Liquid Crystals. *Langmuir* **2008**, *24* (14), 7184–7192. https://doi.org/10.1021/la800849y.

(8) Marrington, R.; Dafforn, T. R.; Halsall, D. J.; Rodger, A. Micro-Volume Couette Flow Sample Orientation for Absorbance and Fluorescence Linear Dichroism. *Biophys J* **2004**, *87* (3), 2002–2012. https://doi.org/10.1529/biophysj.103.035022.

Chapter 5

Applications for photoactive polymers in light-powered actuation

Adapted from the following publication:

1. **Sandlass, S.**; Gordon, M.J., Design and dynamic characterization of a phototunable optofluidic lens. *Opt. Express*, **32**(15), 26445-26457 (2024).

5.1. Introduction

Among the diverse applications for photoresponsive polymers (*cf.* Section 1.1), photoactuation is particularly intriguing for a variety of reasons. For instance, light is easier to spatially program compared to other common means of driving actuation and allows for non-constant curvature deformation within a continuum structure. In addition, light can be delivered virtually instantaneously, is continuously variable in multiple dimensions (intensity, wavelength, polarization, etc.), and is abundant in nature as sunlight. However, designing photoactive materials that can convert light energy into mechanical work within a 3-dimensional structure efficiently and with high spatial fidelity is challenging. While the field of photomechanically active materials continues to develop in the coming decades, steps must be taken now to explore actuator designs that best leverage the advantages of light-based actuation while accommodating the efficiency, heat transfer, and geometric constraints inherent to these materials.

This chapter explores photothermal actuation in two different but complementary applications. In the first application, thermodynamically and mechanically informed design principles are used to guide the construction of a photothermally actuated optofluidic lens that requires 8.2 uJ of mechanical work to change the focal length from 124 mm to 90 mm in 30 s. By using low differential fluid pressures (< 800 Pa) to minimize power consumption during actuation, this lens can be driven with modest 405 nm light intensities (233 mW), despite having a light to work conversion efficiency of approximately 10^{-4}%, which is typical for photoactuation but low compared to other common means of actuation (1% - 99%).[2] The lens is also cyclable, recovering its initial focal length over 60 s in the dark, and can be controlled by modulating the 405 nm intensity during actuation. In the latter half of the chapter, photothermal actuation of a cantilevered DASA-based bilayer film is explored using forced vibration analysis to capture both the structural and material-level changes occurring during

actuation. Using this technique, a 10-40 Hz drop in the resonance frequency and an increase in the structural damping factor were observed under irradiation. These two structural-level changes directly reflected changes occurring on a material scale during actuation, with the former resulting from a decrease in the effective bilayer elastic modulus and the latter resulting from increased viscous dissipation as the DASA-loaded PBMA or PMMA photothermal layer was heated above its glass transition temperature. This ability to dynamically resolve both the structural and material level processes occurring during photothermal actuation using forced vibrational analysis is critical for developing effective strategies in the future for dynamically controlling actuation.

5.2. Design and dynamic characterization of a phototunable optofluidic lens

5.2.1. Introduction

While traditional glass or polycarbonate lenses are limited to a single focal depth, optofluidic lenses offer dynamically tunable optical power by varying the refractive index contrast and/or curvature at one or more fluid-fluid or fluid-elastomer interfaces. As a result, these lenses allow objects at vastly different depths to be imaged in focus at a fixed point without moving the lens. This allows high powered lenses to be manufactured in smaller packages than would be possible with fixed focus lenses without compromising the accessible focal range, making them well suited to applications that would otherwise prohibit or place severe limitations on the motorized movement of the lens (e.g. in medical devices or otherwise confined environments). Depending on the mode of actuation, focus tunable lenses can facilitate 3D imaging at higher speeds than fixed focus lenses[3] and have the potential to operate without electricity[4–7], facilitating their use in explosion-proof spaces and underwater. Furthermore, they can be easier to precision manufacture and more impact/wear resistant than their fixed focus counterparts. These advantages have resulted in the commercialization

of several focus-tunable optofluidic lenses based on various modes of action that include electrowetting (Corning® Varioptic®) and mechanical actuation (Optotune®, Holochip®, poLight®, Dynamic Optics®), which displace a fluid or elastomeric solid to modulate the shape of a lens interface, and gradient refractive index (GRIN) lenses (Mitutoyo® TAGLENS®), whereby the refractive index of the lens medium is controlled to tune the optical power.

Optofluidic lenses that dynamically respond to light stimulus have the potential to improve the performance of modern adaptive optics used in optical data storage[8] and communication, microscopy[9], ophthalmology[7,10] and telescopic imaging[11] by facilitating self-adaptive focusing[5,10], filtering, and attenuation[10,12]. In addition, light can be conveniently manipulated, remotely delivered, and interacts with a vast diversity of organic and inorganic materials, making phototunable lenses well suited for adaptive microlens arrays[3] and flexible optics. One drawback to photoactuation compared with alternative modes of lens actuation is the low efficiency associated with converting light energy into the chemical or mechanical work that is needed to drive a change in the optical and/or physical properties of the lens medium.[13–15] While the efficiency cost of photoactuation is prohibitive in applications requiring a substantial work output at high speed, phototunable lenses based on mechanical actuation can operate with low differential pressures across the lens interface(s), reducing the amount of work required to change focal length. In addition, the lens aperture can be reduced relative to the mass of fluid inside the lens to require less work per unit mass of the fluid. As a result, high energy conversion efficiency is not required as long as the lens is designed to operate successfully despite performing minimal work.

Three different phototunable lens prototypes have been reported to date. One such prototype is based on the photothermal actuation of a hydrogel and requires a substantial 1.4 W/cm^2 of infrared light to actuate a lens with a 1-2 mm aperture, presumably as a result of the high thermal inertia of water.[6] The other two phototunable lens designs are based on liquid

crystal elastomers (LCEs/LCPs/LCNs)[5,7], which undergo a nematic to isotropic phase transition upon photothermal heating to generate the forces required to change the shape of the lens interface (*cf.* Section 1.4).

While LCEs have garnered much attention in the photoactuation community because they allow for better control over the deflection profile and higher strains compared to non-phase change photothermal actuators[16], they can be especially challenging to fabricate because they require mechanical or field-induced alignment. Furthermore, while several different alignment protocols have been developed to date, only a few can achieve the axisymmetric circumferential or radial alignment required to actuate a spherical lens. For example, circumferential lens actuation was demonstrated in 2018 by López-Valdeolivas, et. al using their custom "4-D" extrusion printing technique that aligns the LCE along the print axis from the high shear forces incurred during extrusion.[17] While implementing this technology on a broad scale is appealing, "4-D" LCE printers are not currently commercially available. Conversely, radial lens actuation was demonstrated by Petsch, Schuhladen, and colleagues using eight radially oriented, linearly aligned LCE films arranged in an agonistic grouping around a PDMS lens.[10] In both of these examples, the lenses were thermally actuated using LCEs placed at the outer boundary of the lens, away from the optical axis. To adapt these designs for self-adaptive focusing using photoactuated LCEs, the lens must primarily absorb paraxial rays, which are rays that lie close to the lens optical axis, to drive actuation with minimal spherical aberration. Therefore, the LCE must be placed at the center of the lens without scattering or distorting the beam – requirements that are not yet compatible with the two aforementioned alignment techniques.

In addition to the challenges associated with alignment, LCEs are often more prone to thermal and mechanical damage than other types of elastomers that are typically used in pressure-actuated optofluidic lenses, like poly(dimethyl siloxane) (PDMS). With these

concerns in mind, we developed a phototunable lens design powered by the photothermal expansion of a gas to modulate the focal length instead of using LCEs or hydrogels. The proposed design was easier to manufacture, mechanically robust, and was compatible with on-axis absorption to drive actuation.

Similar thermo-pneumatic designs actuated by resistive heating have been shown to offset the energetic demands of actuation by leveraging a low thermal inertia gas to maximize the fluid displacement and a clear liquid to maximize the refractive index contrast at the lens interface.[18–22] In these designs, the significant density difference between the two phases typically requires that they be separated by a thin flexible membrane that allows the interface to translate or deform when the gas is pressurized while preventing the interface from rotating under the effects of gravity. However, the elasticity of the diaphragm increases the pressure required to actuate the lens and increases power consumption as a result. Despite the attractive simplicity of resistively heated thermo-pneumatic lenses, their optical response times (>1 s[23]) are typically slower than electromagnetically actuated lenses (0.1-10 ms[23]) and they require significant surface area for heating and cooling. As a result, thermo-pneumatic lenses typically are limited to narrow apertures (≤ 3 mm) relative to the area for heat transfer, which is typically 10-100 times larger than the lens aperture.[23] These spatial demands can be partially offset by using photothermal instead of resistive heating because the heating element can be placed within the lens aperture without distorting the light field. In addition, the thermal inertia of the resistive heating element can be reduced with the use of a thin, highly absorbing photothermal film to facilitate faster heating and cooling with high contact area.

In this work, a wide aperture (9.5 mm) photoresponsive lens powered by photothermal pneumatic actuation was developed, leveraging design principles drawn from resistively heated pneumatic lenses. The photothermal lens incorporated two fluid phases, air and water, as the working and optical fluids, respectively, and a 405 nm laser was used to actuate the

lens by inducing photothermal expansion of the air to displace water between two membrane-bound air-water interfaces. To capture the dynamic change in focal length during actuation, the diameter of a 532 nm probe beam was measured at a constant distance from the lens and experimentally validated models were used to calculate the corresponding focal length. By capturing the lens dynamics, including pressure, temperature, and focal length, this work demonstrates a novel approach to phototunable lens actuation and provides a methodological framework for future efforts aiming to dynamically measure and control the optical power of a tunable lens using light.

5.2.2. Methods

5.2.2.1. Optofluidic lens assembly

The optofluidic lenses used throughout this study were designed with a stackable structure as illustrated in Fig. 5.1. Depending on the experimental conditions, the lens could be assembled with either a single membrane bound interface or two stacked interfaces. Engineering diagrams for all of the lens parts illustrated in Fig. 5.1 are available for download (see ref. 24).

5.2.2.1.1. Pump-actuated single interface lens

In the single interface configuration, an aluminum base plate was screw mounted to a 6.3 mm-thick aluminum reservoir plate. A glass window was placed between the base and reservoir plates and sealed against the reservoir plate with a rubber o-ring (#30). The reservoir plate had a 17.5 mm hole in the center to accommodate the fluid along with two fluid inlet/outlet ports that were thread-mounted to barbed 1/16” ID tube adapters (McMaster Carr, part # 5454K74). A second o-ring was placed between the top of the reservoir plate and a 250 μm thick commercial PDMS film. The film was pre-tensioned and adhered using double-sided tape to the top of the reservoir plate. Pre-tensioning of the membrane was critical to limiting

the effects of gravitational sag, which are known to cause coma aberrations in fluid lenses. An aperture plate was then screw mounted on top of the reservoir plate. The diameter of the hole drilled through the center of the aperture plate was less than the diameter of the fluid reservoir and therefore determined the aperture of the lens. A syringe pump was used to change the fluid volume, and a 3-way valve was placed at the fluid outlet to seal and drain the reservoir. A pressure sensor (Pendotech PRESS-S-000) was also placed at the fluid outlet and an Arduino Uno with an HX711 digital amplifier chip was used to measure the lens pressure. Unless otherwise noted, Luer lock fittings were used for all adaptors and valves. The single interface pump-actuated lens assembly is illustrated schematically in Fig. 5.1.a and 5.1.c.i. Aperture diameters of 9.5 mm and 15.9 mm were studied in this work.

5.2.2.1.2. Photothermally actuated double interface lens

To assemble the photothermally actuated fluid lens, an aluminum base plate was screw mounted to a reservoir plate with a glass window, 76 μm thick Kapton polyimide (PI) film (DuPont), and rubber sealing o-ring placed between. Apart from a thermocouple port, which was added to the reservoir plate in the photothermal lens to measure the fluid temperature, the part dimensions were identical to those used in the pump-actuated lens (Sec. 5.2.2.1.1). Unlike the pump actuated lens, however, this reservoir was filled with air instead of water. A 250 μm thick PDMS membrane was pre-tensioned on top of this air reservoir plate as in the pump actuated lens and the water reservoir assembly was screwed to on top to seal the fluid interface. The water reservoir assembly was constructed by screwing a 9.5 mm diameter aperture plate to the top of a second reservoir plate, equal in dimension to the air reservoir plate, with a second 250 μm thick pre-tensioned PDMS membrane sealed between. A thermocouple port was not added to the water reservoir because the amount of heat transfer between the two reservoirs was expected to be insufficient for appreciably changing the

temperature of the water. This lens assembly is illustrated schematically in Fig. 5.1.b and 5.1.c.ii and photographs of the lens are provided elsewhere†.

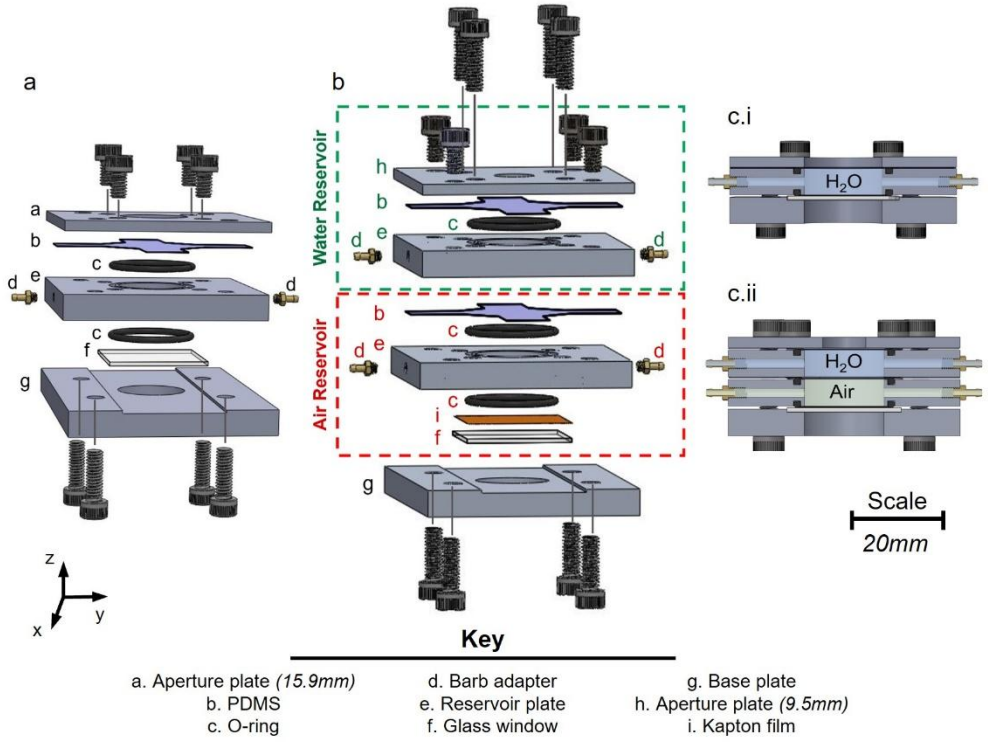

Fig. 5.1. Optofluidic lens construction. (a) Pump actuated single interface water lens with components labelled (see key). (b) Photothermal double interface water-air lens with components labelled (see key). (c.i) Side view of wide aperture (15.9 mm diameter) pump actuated water lens. (c.ii) Side view of 9.5 mm aperture photothermal lens. All lens assemblies drawn according to the scale in bottom right. For convention, lens axes correspond to the coordinate system in the lower left where z is the optical axis.

To control the unactuated lens pressure, a syringe pump was used to manipulate the headspace pressure in a secondary water reservoir that was pressure equilibrated with the water-filled lens cavity. This approach allowed the unactuated lens focal length to be controlled with greater precision than was possible by directly pumping water into the lens. Throughout this work, the unactuated gauge pressure in the air reservoir was set to zero for consistency. As a result, the unactuated pressure differentials across the two PDMS-bound lens interfaces were equal. During actuation, the air pressure was measured using a pressure

† Photographs of the lens can be found in the supplemental file of ref. 1.

sensor as described previously for the single interface lens. The air temperature was measured with an Arduino using a K-type thermocouple and a MAX6675 digital converter.

5.2.2.2. Surface profiling

A Texture Technologies Texture Analyzer was used to profile the pressure-driven deformation of the membrane-bound lens interface. To probe the surface, a 2 mm diameter cylindrical steel force probe was lowered at a rate of 0.1 mm/s until a compressive force of 10 mN was measured and subsequently raised back to its initial position at the same rate. The position of the interface was determined from the height of the probe where the measured force exceeded the noise threshold (1 mN). The lens volume was controlled using a syringe pump and an x-y stage was used to position the lens relative to the force probe. This method was selected over standard profilometry because the walls of the aperture plate limited the range of radial positions that could be profiled without the sensor contacting the plate walls.

5.2.2.3. Focal length measurement

An unpolarized 532 nm Nd:YAG laser (Q-BAIHE) was used to measure the focal length of the fluid lenses described in Sections 5.2.2.1. The collimated 532 nm beam was expanded and subsequently reduced using an iris to adjust the diameter to 1.75 mm, which was used throughout this work. The beam was reflected at 90^{o} using a 50/50 non-polarizing beam splitter (Thorlabs CCM1-BS013) and passed through the center of the lens aperture. For pump actuated lens, the incident beam passed normally through the flat glass face of the lens. The 532 nm beam intensity was maintained below 1 mW/cm^{2}.

The diameter of the 532 nm beam was measured as a function of distance from the lens using a 20-megapixel Basler Ace camera (acA5472-17uc) mounted on a motorized linear stage. Compared to the methods used to measure the focal lengths of other published thermo-pneumatic lenses, which have 1-2 mm diameter apertures, the significantly wider lens

apertures used in this work (9.5 mm and 15.9 mm) allowed the beam profile to be imaged at the focal point without the use of a microscope objective. In all other respects, the measurement techniques were identical to those described in refs. 21 and 22. The image acquisition and camera position were controlled using LabVIEW. In addition, LabVIEW was used for real time image processing. A 15% intensity threshold was used to binarize the beam profile and the camera exposure time was manually adjusted to maintain a maximum intensity within the dynamic range of the CMOS sensor. The minimum measurable focal length was 17.5 mm based on the depth of the sensor inside the camera casing. The translational range of the camera stage was approximately 130 mm. Accurate focal length measurements were confirmed using a series of calibrated glass lenses.‡ To measure the sensitivity of the fluid lens to rotation, the camera stage could be rotated to align with the optical axis of the lens and a mirror was used to adjust the propagation direction of the beam accordingly.

To measure the focal length of the double interface phototunable lens during actuation, a collimated unpolarized 405 nm laser beam (Rui Diao) was expanded to 6 mm in diameter and passed through the beamsplitter such that both the 532 nm and 405 nm beams propagated along the same axis. The photothermal lens was placed in the beam path with its optical axis aligned with the center of both beams and oriented to intersect the incident beam at the PI surface. The laser current was metered using the onboard power supply module to control the 405 nm intensity. Photothermal actuation of the lens was only performed with the optical axis normal to gravity (vertical configuration in Fig. 5.2) because of safety concerns associated with directing the high intensity 405 nm beam vertically upwards. LabVIEW was used for data acquisition and to control the timing of the irradiation cycles by triggering a beam

‡ Calibration data can be found in the supplemental file of ref. 1.

flag. A schematic illustration of the phototunable focal length measurement apparatus is provided in Fig. 5.2.

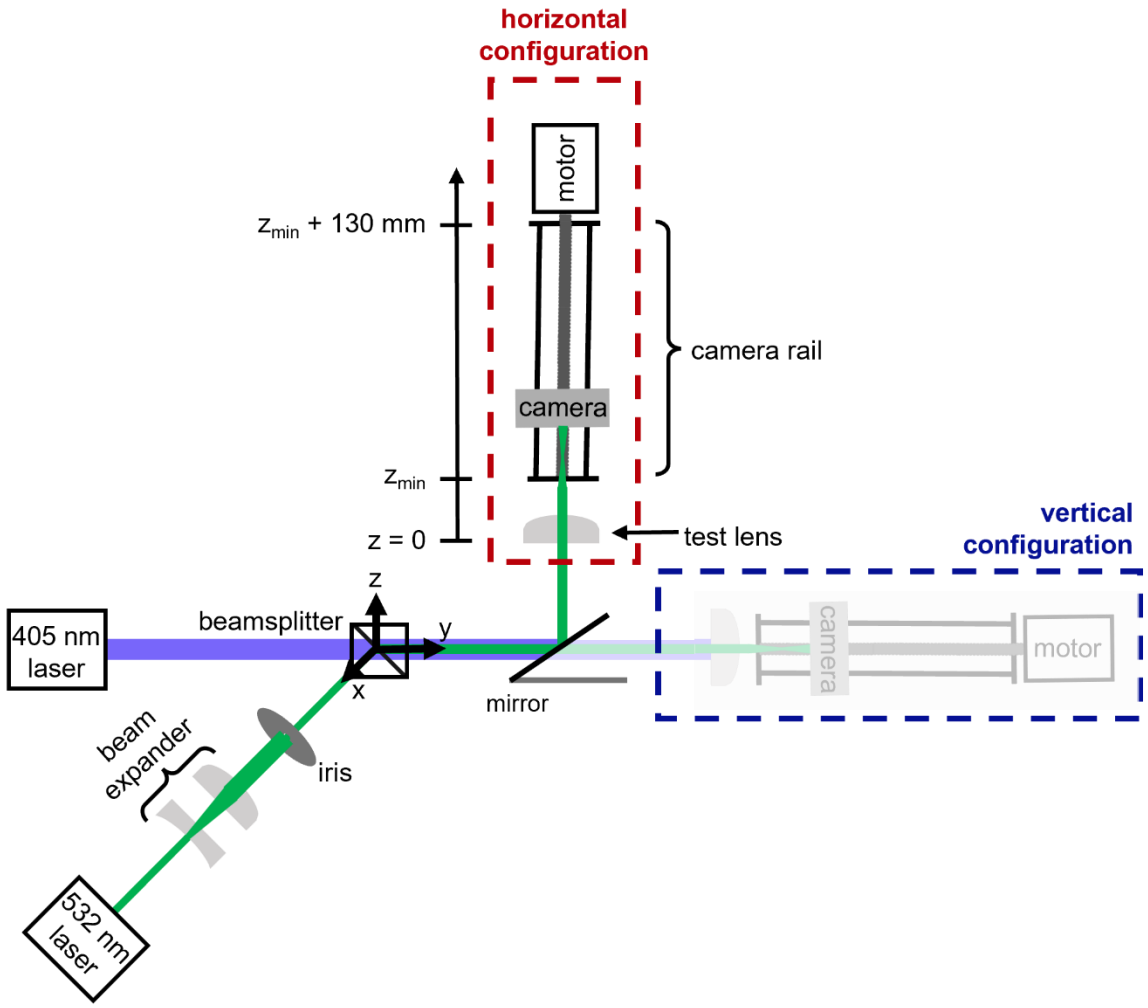

Fig. 5.2. Schematic diagram of lens testing apparatus. The 532 nm beam was used to measure focal length, and the 405 nm beam was used to actuate the lens. A removable mirror served to reflect the 532 nm beam 90° upwards for testing the lens in a horizontal position with its optical axis aligned with gravity (red). The lens was also tested in a vertical orientation (blue) with the 532 nm and 405 nm beams propagating in the x-y plane. To accommodate testing the lens in different configurations, the motorized camera rail system could also be rotated to align with the propagation axis of the 532 nm beam. For safety reasons, photoactuation with 405 nm light was only tested in the vertical configuration.

5.2.3. Results and discussion

5.2.3.1. Mechanical and optical characterization of the fluid lens interface

Unlike fixed focus lenses, the curvature of an optofluidic lens cannot be directly controlled but is a consequence of minimizing the interfacial free energy. This makes it challenging to design variable focus spherical lenses that obey the fundamental definition of focal length, f, used for fixed focus lenses in air under the paraxial approximation (equation 5.1). This definition assumes a uniform radius of curvature for each lens interface i, R_i, and refractive index, n, where Δn refers to difference in refractive index between the lens and its surroundings, typically assumed to be n = 1 for air. When the lens radii of curvature are similar or less than the thickness of the lens, the calculation of focal length must also account for the thickness of the lens, d. Specifically in the case of a pressure actuated lens bound by an elastic membrane, the necessary boundary conditions for a mechanically stable interface result in a parabolic deformation profile that can be approximated as constant curvature only in the limit of small deformation. This limit, derived by Ren et al.[25], does not consider inelastic strain, which may also result in non-constant curvature deformation of the interface despite being in the "low deformation" limit. Therefore, it is crucial to measure the membrane-bound lens interface during actuation to determine whether the constant curvature approximation, and Equation 4.1 as a result, are valid.

$$\frac{1}{f} = (\Delta n)\left(\frac{1}{R_1} + \frac{1}{R_2} + \frac{\Delta n d}{n R_1 R_2}\right) \tag{5.1}$$

To accomplish this, the deflection profile of the 15.9 mm aperture single interface lens described in Section 5.2.2.1 was measured using the method outlined in Section 5.2.2.2. The interface position was probed at a number of evenly spaced distances from the center of the lens (r) while using a syringe pump to increase the volume of water inside the lens cavity. To

ensure continuity about the center of the lens, the interface was probed along a single radial path away from the midpoint and mirrored over r = 0 for all volumes tested except 0.55 mL, for which all nine plotted points were measured directly. To avoid contact between the probe and the aluminum aperture plate, the interface was not profiled within 1.5 mm of the aperture boundary. Consequently, a volume-dependent vertical offset was included as an additional free parameter in the constant curvature fittings used to determine the volume-dependent radius of curvature. All fittings had R squared values greater than 0.94, indicating that the interface could be described accurately with a single radius of curvature within range of radial distances measured. With increasing fluid volume, the radius of curvature was found to decrease with an empirical power law dependence.[§] The measured interface heights and constant curvature fittings for each volume tested are plotted in Fig. 5.3.b.

After mechanically confirming that the PDMS-bound air-water interface deformed with constant curvature when pressurized, the focusing properties of the deformed interface were measured using the focal length measurement apparatus described in Section 5.2.2.3. The effect of aperture size on the optical properties of the lens was evaluated by testing two different diameters, 15.9 mm and 9.5 mm. At each data point, the beam profile was measured as a function of distance from the lens and the nominal (spatially averaged) beam diameter was used to determine the focal length of the lens. The results are plotted in Fig. 5.3.c.i and 5.3.c.ii for the larger and smaller aperture lenses, respectively. The measured beam dimensions in the x and y lens axes (labelled in Fig. 5.1) yielded the focal error bars, where the size of the error bars indicates the amount of convergence anisotropy in the beam.

[§] The lens radius of curvature and pressure plotted a function of fluid volume can be found in the supplemental file of ref. 1.

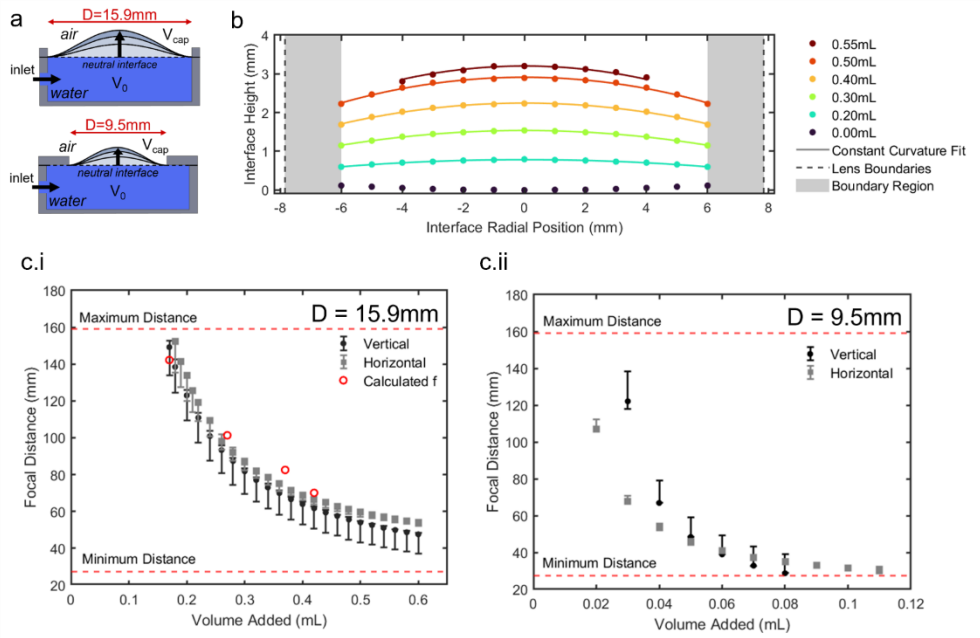

Fig. 5.3. (a) Illustration of fluid lens pumping actuation for 15.9 mm (top) and 9.5 mm (bottom) diameter apertures. (b) Deflection profile of the 15.9 mm diameter lens illustrated in (a) as a function of added water volume. Constant curvature fittings provided (solid lines). The lens boundary is indicated with dashed lines at a radial position of ± 7.95 mm. The boundary region (gray) could not be profiled. (c.i) Focal length vs. added volume for the lens profiled in (b). Measurements were performed with the membrane interface orientated normal (horizontal, gray squares) and aligned (vertical, black circles) with gravity. Theoretical focal lengths (red open circles) calculated from constant curvature fits in (a). Dashed lines denote range of measurable focal lengths. (c.ii) Focal length vs. water volume added for the 9.5 mm diameter lens illustrated in (a). For (c.i) and (c.ii), vertical error bars indicate the degree of convergence anisotropy as defined in the text.

Overlaid on the data in Fig. 5.3.c.i are the theoretical focal lengths calculated using equation 5.1 from the curvatures measured by surface profiling (Fig. 5.3.b) assuming a refractive index for water of 1.33 (for single interface lens, $1/R_1 = 0$). A manual x-offset was introduced in the theoretical data to account for the fact that the absolute starting volume of the lens, V_0, was difficult to control. The theoretical and measured focal lengths trended closely with one another, further indicating that the 15.9 mm aperture lens could be described accurately with the traditional paraxial spherical lens equation. However, the smaller aperture lens could not be mechanically profiled because the surface probe was too large relative to the lens aperture. As a result, no theoretical focal lengths were calculated.

Coma aberrations are known to affect the focusing properties of fluid lenses when the optical axis of the lens is aligned perpendicular to gravity (blue vertical configuration in Fig. 5.2). In this orientation, hydrostatic pressure causes the lens interface to sag, resulting in anisotropy in the beam convergence profile. The magnitude of this effect was assessed by testing each lens in a horizontal configuration, where the lens optical axis was aligned with gravity, and in a vertical configuration, where the optical axis was perpendicular to gravity. These results are plotted in Fig. 5.3.c.i and 5.3.c.ii in gray and black, respectively. A larger difference between the focal lengths measured along the lens x and y axes (indicated by the size of the vertical error bars) was observed for both apertures in the vertical configuration, indicating the presence of coma. Additionally, a steeper drop in focal length with added volume was observed in the vertical orientation for the 9.5 mm lens. This effect was less marked in the larger aperture lens, likely because the wider aperture helped to offset distortion caused by axially asymmetric tensioning of the PDMS membrane. Theoretical focal lengths were only calculated in the horizontal configuration because the surface profiling probe could not be rotated to measure a vertical lens interface.

5.2.3.2. Photothermal lens actuation

To photothermally actuate the two-phase fluid lens described in Section 5.2.2.1.2, a high intensity 405 nm laser was introduced to heat the lens while the focal length was determined from the convergence of a 532 nm low intensity probe beam. The 405 nm light was absorbed by the photothermal PI film in excess of 99.9% and converted into heat while the 532 nm beam passed through the PI film, attenuated by approximately 90%. Heat transfer between the PI film and the air inside the lens resulted in thermo-pneumatic expansion, which was leveraged to drive the displacement of water between two membrane-bound deformable air-water interfaces. Approximating air as an ideal gas around room temperature (295 K) and atmospheric pressure, the air reservoir was expected to expand at a rate of 0.3% per degree

Celsius based on the ideal gas law. Water was used as the optical fluid in this design because it was low viscosity, non-toxic, chemically inert, and had significant refractive index contrast with air (Δn = 0.33). The high thermal inertia of water, however, made this design only suitable for relatively low-temperature, low-pressure actuation. The mechanism of actuation is described schematically in Fig. 5.4.

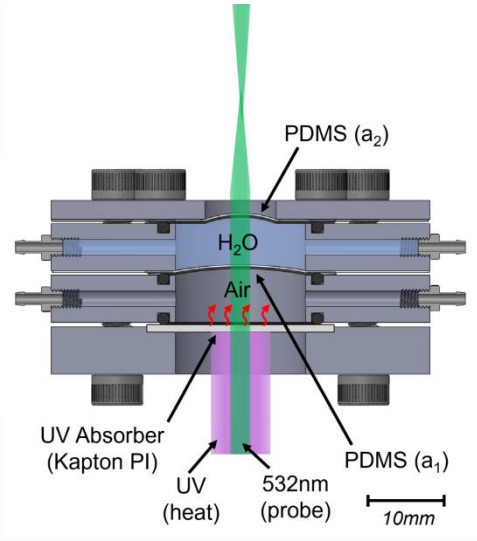

Fig. 5.4. Schematic illustration of photothermal lens actuation. Scale bar inset. Interface diameters are labelled as a_1 (active interface) and a_2 (passive interface) where a_1/a_2 = 1.8.

In this design, the two fluid interfaces were placed in series along the optical axis to minimize the lens size relative to the aperture area while allowing the lens to be operated with a constant total water volume. By changing the two interface diameters relative to one another, the amount of work required to achieve a specified change in focusing power could be controlled. To quantify this effect, the ratio of the "active" interface diameter (a_1 in Fig. 5.4) relative to the "passive" interface diameter (a_2 in Fig. 5.4) was defined in this work as the mechano-optical advantage, or MOA, and was inversely related to the aperture size relative to the total lens area. An MOA greater than 1 ensured that optical power strictly increased during actuation, provided that the unactuated focal length was positive. Throughout this work, an MOA of 1.8 was used.

The unactuated focal length of the lens was controlled by changing the amount of water inside the lens. Throughout this study, the unactuated gauge pressure of the air reservoir was maintained at 0 in-H_2O for simplicity and because the effect of changing the unactuated air pressure was expected to be minimal for the range of focal lens studied in this work (see derivation in the supplemental file of ref. 1).

During actuation, the focal length of the lens changed faster than the camera stage could be moved. As a result, a new approach to quantifying the dynamically changing focal length was required. In this approach, the time dependent beam diameter, $D(t)$, was measured at a single distance from the lens, z_i, and related that to the focal length, $f(t)$, using equation 5.2. This equation assumed a collimated Gaussian beam that converged to a minimum spot size (SS) at the focal point with a constant convergence/divergence angle (θ). To limit diffraction effects, z_i was assumed to be sufficiently outside the lens depth of field (DOF), which became narrower as the focal length decreased. Therefore, an accurate estimate of $f(t)$ from $D(t)$ required that z_i never approach $f(t)$. Equation 5.2 also does not account for aberrations induced by non-constant curvature of the lens interface. Errors introduced by modelling the photothermal lens as spherical were not expected to be significant based on the results of Section 5.2.3.1, provided that the diameter of the beam used to measure focal length (1.75 mm) was sufficiently small relative to the lens aperture (9.5 mm).

$$f(t) = \frac{z_i}{\left[1 - \left(\frac{D(t, z_i)}{D_i(z_i)}\right)\left(1 - \frac{z_i}{f_i}\right)\right]} \tag{5.2}$$

Before actuation, a focal length of 124 mm ± 5 mm was measured by tracking the beam diameter as a function of distance from the lens. These results are plotted in Fig. 5.5.b. Small jumps in the measured beam diameter were observed upon changing the camera

exposure time (black asterisks in Fig. 5.5.b), indicating a slightly non-linear response in the camera sensor.

Close agreement between the beam diameters measured along the lens x (red) and y (blue) axes indicated a lack of significant coma distortion in the photothermal fluid lens. The nominal beam diameter was slightly less than the beam diameter measured along the x and y axes, likely because of transverse mode patterns in the 532 nm beam profile. However, the beam profile measured by all three methods converged linearly with distance from the lens to within a few millimeters of the same focal point, in agreement with equation 5.2.

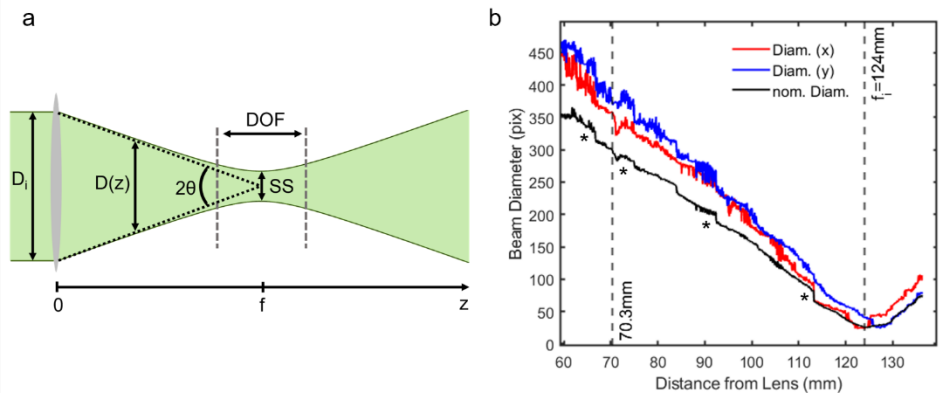

Fig. 5.5. Convergence profile of a collimated Gaussian beam passing through a spherical lens and propagating to the right. (a) Simulated using Snell's law. Variables are defined in the text. (b) Beam diameter vs. distance from the lens measured from spatial averaging (nominal, black) and along the lens x (red) and y (blue) axes. The focal length (f) is identified as 124 ± 5 mm. Changing the camera exposure time to capture more diffuse beams resulted in small jumps in the measured diameter, indicated with black asterisks (*).

To demonstrate photothermal actuation of the lens, three irradiation cycles of 30 s on and 60 s off were performed at a 405 nm intensity of 233 mW. The lens focal length and the air reservoir pressure/temperature are plotted over the three actuation cycles in Fig. 5.6.a and 5.6.b, respectively. The beam diameter was measured in real time at z_i = 70.3 mm (indicated with a dashed line in Fig. 5.5.b) and converted to focal length using equation 45.2. Before actuation, the focal distance was measured as 124 ± 5 mm based on the beam profiling results plotted in Fig. 5.5. During actuation, the focal length was observed to drop by 27 % from 124 mm to 90 mm and recovered to 124 mm after cooling. At the same time, the air pressure and

temperature rose by 2.3 in-H_2O (approximately 0.6 %) and 1.5 ^oC, respectively. The measured temperature rise was likely an underestimation of the true air temperature at the photothermal interface because the size of the thermocouple junction was significant relative to the width of the thermal gradients established under irradiation. The image performance of the double interface fluid lens is provided elsewhere[**].

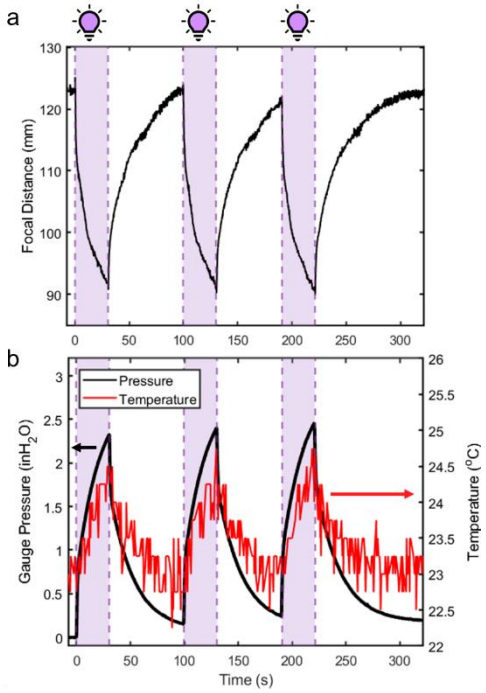

Fig. 5.6. Photoactuation of two-phase fluid lens. (a) Lens focal length vs. time for 3 irradiation cycles (30 s on/60 s off) with 233 mW of 405 nm light. Focal length was calculated from the starting focal length (124 ± 5 mm in Fig. 5.5.b) and the beam diameter measured 70.3 mm from lens (labelled in Fig. 5.5.b) using equation 5.2. Exposure time was fixed during actuation. (b) Air pressure and temperature measured during actuation. Time axes in (a) and (b) are coincident.

The change in optical power over 30 s of irradiation was measured for five different light intensities between 56 mW and 233 mW and is plotted in Fig. 5.7.a. Optical power, defined as the reciprocal of focal length, strictly increased with irradiation time for all light intensities tested, indicating a corresponding increase in the effective lens curvature (equation

[**] Imaging performance of the double interface fluid lens is provided in the supplemental file of ref. 1.

5.1). In addition, higher light intensities resulted in greater photothermal heating and longer thermal equilibrium times, indicated by a plateau in optical power observed during 30s of irradiation with 56 mW and the lack of a plateau after 30 s of irradiation with 233 mW.

The maximum increase in air pressure and the relative change in optical power after 30 s of irradiation are plotted in Fig. 5.7.b for the same 405 nm light intensities that are plotted in Fig. 5.7.a. Intuitively, a greater input of light energy was expected to result in increased work done displacing the lens interface. This was supported by the positive correlations observed between the light intensity and the actuation induced change in optical power (reflecting the interface deformation) and air pressure (reflecting the elastic energy stored across this interface).

To estimate the energy efficiency of the lens, a pressure-volume calibration was performed using a syringe pump to control the volume of the air reservoir and the resulting change in pressure was measured. Using this calibration and the measured pressure change during actuation, the increase in air volume after 30 s of irradiation at 233 mW was estimated to be 0.023 mL, or roughly 1.8 % of the neutral interface air reservoir volume (V_0 in Fig 5.2). This expansion required 8.2 uJ of mechanical work to displace the membrane-bound lens interfaces against the elastic restoring force of the PDMS and the hydrostatic pressure of water. Assuming total absorption of the 405 nm pump light, the light to work conversion efficiency was calculated as 10^{-4} %. Interestingly, the energy conversion efficiency strictly increased with increasing 405 nm light intensity (see Table 5.1). This was likely the result of improved heat transfer between the photothermal interface and air as the temperature difference increased. The calculation of energy efficiency is performed in greater detail in the supplemental of ref. 1.

Table 5.1. Photomechanical energy efficiencies at different light powers for the photothermally actuated fluid lens designed and tested in this work.

405 nm Power (mW)	E_{in} (J)	W (μJ)	Efficiency (%)
56	1.7	0.7	4.0×10^{-5}
93	2.8	1.8	6.3×10^{-5}
129	3.9	3.1	8.0×10^{-5}
168	5.0	4.8	9.5×10^{-5}
233	7.0	8.2	1.2×10^{-4}

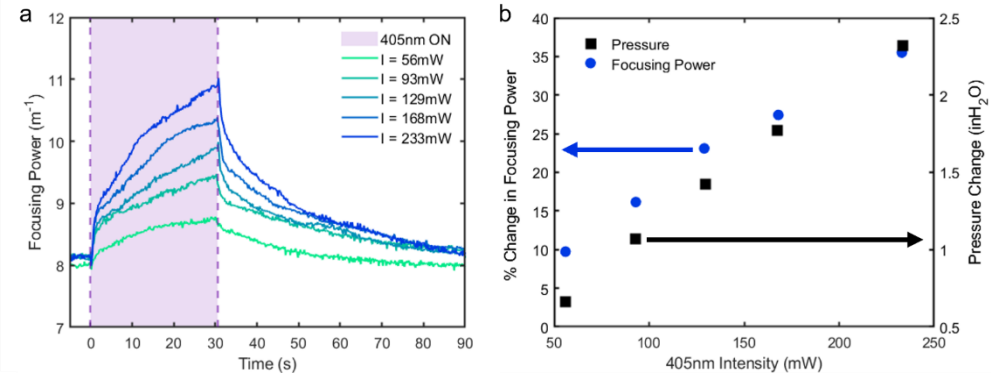

Fig. 5.6. Intensity dependent lens actuation. (a) Optical power (reciprocal of focal length) measured during and after 30 s of irradiation with varying light intensity. Exposure time indicated in purple. (b) Air pressure increase (black squares, right axis) and relative percent change in optical power (blue dots, left axis) measured between the start and end of irradiation versus the 405 nm intensity.

5.2.4. Conclusion

This work described the design and characterization of a two phase optofluidic lens that increased in focal length when exposed to light as a result of photothermal heating. Compared to alternative mechanically driven phototunable lens designs based on LCEs or hydrogels, this design combined simplicity with mechanical robustness while allowing for on-axis absorption to power the lens, thereby limiting spherical aberration. Using thermodynamically and mechanically informed design principles developed for resistively heated thermopneumatic lenses, a 27 % drop in the focal length, from 124 mm to 90 mm, was

achieved in 30 s with a light intensity of 233 mW. This corresponded to a 10^{-4} % light to work conversion efficiency, which was low compared to other common actuation styles (1 % - 99 %)[2], but typical for photoactuation (10^{-6} % - 0.1 %)[13,14,26,27]. Bearing in mind the low efficiency associated with converting light into mechanical work, tunable lenses are particularly well suited to photoactuation because the differential pressure across the lens interface only needs to exceed the force of hydrostatic pressure and the elastic restoring force of the elastomeric membrane used to stabilize the interface. As a result, the mechanical work that must be done displacing the lens interface is minimal. In the lens design outlined in this work, the pressure increase required to decrease the focal length from 124 mm to 90 mm was a modest 0.6 %, corresponding to 8.2 μJ of work, and the lack of coma in the beam convergence profile (Fig. 5.5.a) indicated that the restoring force of the thin (250 μm) PDMS support layer was sufficient to prevent sagging from hydrostatic pressure.

In the future, modifications to the lens design that affect the energy efficiency, actuation speed, and the wavelengths of light suitable for absorption and transmission may be necessary to optimize the lens performance for a particular application. For example, this work demonstrated user-controlled actuation, where different light sources were used for actuation and focusing. However, self-adaptive focusing and defocusing would also be possible using a wider bandwidth light source to actuate the lens, provided it has sufficient intensity above and below 480 nm, which is the absorption cutoff for Kapton PI. To increase the energy efficiency of the lens, modifications can be made to the lens design that minimize heat loss and promote more effective heat transfer between the photothermal surface and air. This could be accomplished by switching from a thermally conducting aluminum lens casing to a better insulating but still machinable material, like polycarbonate, or by using an optical fluid with lower thermal inertia than water, like castor or silicon oil. However, minimizing heat loss inevitably increases the cooling time of the lens, so an optimization study is necessary to

determine the necessary conditions for maximizing the thermodynamic efficiency of the lens while minimizing its response time. Alternatively, using a microporous photothermal material instead of a PI film could improve heat transfer between the photothermal surface and air by increasing their contact area.

Additional modifications to the lens design could be made to increase the accessible focal range and reduce the lens response time without directly affecting energy efficiency. However, such modifications also have their respective drawbacks. For example, changing the optical fluid from water (n = 1.3) to a liquid with a larger refractive index, like silicon oil (n = 1.4) would reduce the change in curvature required to achieve a desired change in focal length. From a practical perspective, these oil-based fluids are not as ideal because they're more likely to diffuse through the PDMS membrane over time and have a higher viscosity, requiring more pressure to displace the fluid and increasing the likelihood of entraining air bubbles.[20] Changing the MOA of the lens could also help to reduce the work required to achieve a desired shift in focal length but would require reducing the size of the aperture relative to the total lens size. However, this is undesirable for the design of phototunable lens arrays because it lowers the maximum attainable packing fraction of the array. Lastly, switching to a thinner PDMS membrane could reduce the amount of work required to displace the lens interfaces by lowering the operating pressure of the lens. Unfortunately, this would also make the lens more susceptible to coma when rotated.

One final area that should be explored in the future is how to design optofluidic lenses that adopt alternative (nonspherical) lens geometries when actuated (e. g., cylindrical, meniscus, parabolic, etc.). This is one objective that is likely better suited to photochemical actuation than photothermal actuation because the former allows for better spatial resolution in the actuated geometry. Despite this great potential, the use of photochemical actuation for controlling the focal distance of a tunable lens remains largely unexplored.

5.3. Photothermal actuation of DASA-based bilayer cantilevers under forced vibration

5.3.1. Introduction

While actuation is fundamentally a dynamic process, photoactuators are typically analyzed as static, where a light stimulus X results in a change from static conformation Y to static conformation Z over some specified time interval. This is because photoactuation is often too mechanistically complex to dynamically model, with multiple time and space dependent subprocesses (heat transfer, photoisomerization kinetics, phase change, etc.). In the specific case of a photothermal bilayer bending actuator that is an isotropic thin film with a temperature independent modulus, the dynamic actuator deformation is simple enough to map directly to temperature, stress, work, and energy efficiency using Timoshenko's bimetal thermostat model (*cf.* Section 1.4.1.1). However, more complicated systems incorporating non-uniform irradiation, actuation dependent heat transfer kinetics, and/or thermally induced phase changes require a different, dynamical approach to measuring and modelling the mechanical response during actuation.

Vibrational analysis is a well-established method for assessing the elasticity and strain state of cantilevered mechanical sensors.[28–32] In this technique, the cantilever is driven at one end with an oscillatory force ($F_0 sin(\omega t)$) and the periodic amplitude (A) and phase (ϕ) are measured as a function of the drive frequency (ω). The vibrational dynamics of cantilevered beams are typically modelled as a bead spring system where a bead of mass m^* (i.e. a point mass) is placed on the tip of a massless spring with force constant k. At the resonance frequency, ω_0, the inertial and spring forces in the cantilever or bead spring system perfectly cancel one another out and the vibrational amplitude diverges to infinity. This condition occurs when the drive frequency is equal to the square root of k over m^* (equation 5.3). In practice,

however, vibrational damping forces are present from fluid resistance and internal anelasticity in the cantilever/spring that result in a finite valued amplitude at resonance. The strength of the damping force is described by the damping coefficient, γ. Solutions for the tip amplitude and phase offset are provided as functions of frequency in equations 5.4 and 5.5.

$$\omega_0 = \sqrt{\frac{k}{m^*}} \tag{5.3}$$

$$A(\omega) = \frac{F_0}{m^*} \frac{1}{\sqrt{(\omega_0^2 - \omega^2)^2 + 4\gamma^2\omega^2}} \tag{5.4}$$

$$\Phi(\omega) = \operatorname{atan}\left(\frac{2\gamma\omega}{\omega_0^2 - \omega^2}\right) \tag{5.5}$$

In this model, m^* is referred to as the effective mass and is related to the cantilever mass and the vibrational mode shape. For frequencies at and below the fundamental harmonic, the effective mass is typically estimated to be 24 % of the total cantilever mass by assuming that the vibrational mode shape is well approximated by the deflection profile of a cantilever under static endpoint loading. The spring constant in the bead-spring model is related to the cantilever's elastic modulus (E), which represents its material properties, and its moment of inertia (I), which reflects its geometry. A general form for the relationship between the resonance frequency of a driven cantilever and its relevant structural/material parameters is provided in equation 5.6, where w, t, L, and ρ are the cantilever width, thickness, length and density. λ_n is the beam eigenvalue for resonance mode n that satisfies the condition for resonance by balancing the inertial and bending stiffness forces. For the fundamental harmonic ($n = 0$), λ_n = 1.8751.

$$\omega_n^2 = \frac{\lambda_n^4 \left(\frac{EI}{w}\right)}{\rho t} \frac{1}{L^4} \tag{5.6}$$

For a monolayer film, the quantity EI/w is defined in terms of the cantilever thickness and elastic modulus in equation 5.6.a. For bilayer film, the definition of EI/w is more complicated and is provided in equation 5.7.b. The derivation of this expression can be found in full detail in ref. 33.

$$\left(\frac{E^*I}{w}\right)_{monolayer} = \frac{Et^3}{12} \tag{5.7.a}$$

$$\left(\frac{E^*I}{w}\right)_{bilayer} = E_1\left(\frac{t_1^3}{3} + t_1^2\xi + t_1\xi^2\right) + E_2\left(\frac{t_2^3}{3} - t_2^2\xi + t_2\xi^2\right); \xi = \frac{1}{2}\frac{E_1t_1^2 - E_2t_2^2}{E_1t_1 + E_2t_2} \tag{5.7.b}$$

5.3.2. Results and discussion

To demonstrate how vibrational analysis can provide insight into the mechanical properties of bilayer films, the technique was used to measure the elastic modulus of a commercial bilayer of fluorinated ethylene propylene (FEP) on Kapton PI. To achieve this, the film was cut into a 10 mm x 1 mm cantilever and mounted onto a vibration exciter that was custom built from a subwoofer (Skar Audio SVR-12) driven with a variable frequency sine wave. A tunable amplifier was used to control the drive amplitude. This system was used in place of piezoelectric drivers because it had fewer internal mechanical resonances. The cantilever was swept through a range of frequencies, pausing briefly at each sampled frequency to ensure steady state dynamics before photographing the cantilever with a high-speed camera (Basler acA720-520um) at periodic instances under constant oscillation. The camera and drive frequency were controlled using LabVIEW. Post processing of the images was performed in MATLAB to determine the frequency-dependent amplitude and phase relative to a reference position at the cantilever's pinned edge. From this analysis, the fundamental harmonic frequency (ω_0) was calculated by fitting the amplitude and phase to their functional forms presented in equations 5.4 and 5.5.

Based on the scaling between ω_0 and L^2 predicted by equation 5.6, the plot of ω_0^2 against $1/L^4$ was expected to be linear with a slope that reflected the film elastic modulus. This was confirmed for a PI film and a bilayer of FEP on PI in Fig 5.7. Their corresponding moduli were determined to be 2.56 GPa and 1.88 GPa, which were within experimental error of their tensile moduli measured by the ASTM standard method. To obtain the bilayer modulus, which is a weighted average of the FEP and PI moduli based on their respective thicknesses, the PI modulus measured for a monolayer film was used to calculate the FEP modulus based on equation 5.7.b. Interestingly, the effective bilayer modulus computed from vibrational analysis closely agreed with the tensile modulus, indicating that the presence of interfacial stress did not significantly affect the resonance frequency. This was likely due to the cantilever geometry, which allowed the film to relax internal stress by bending. This can be observed in the cantilever cross section image inset in Fig 5.7.b. To confirm that the results measured by vibrational analysis were reproducible, three replicate FEP-PI bilayers were tested and are plotted together in Fig. 5.7.b.

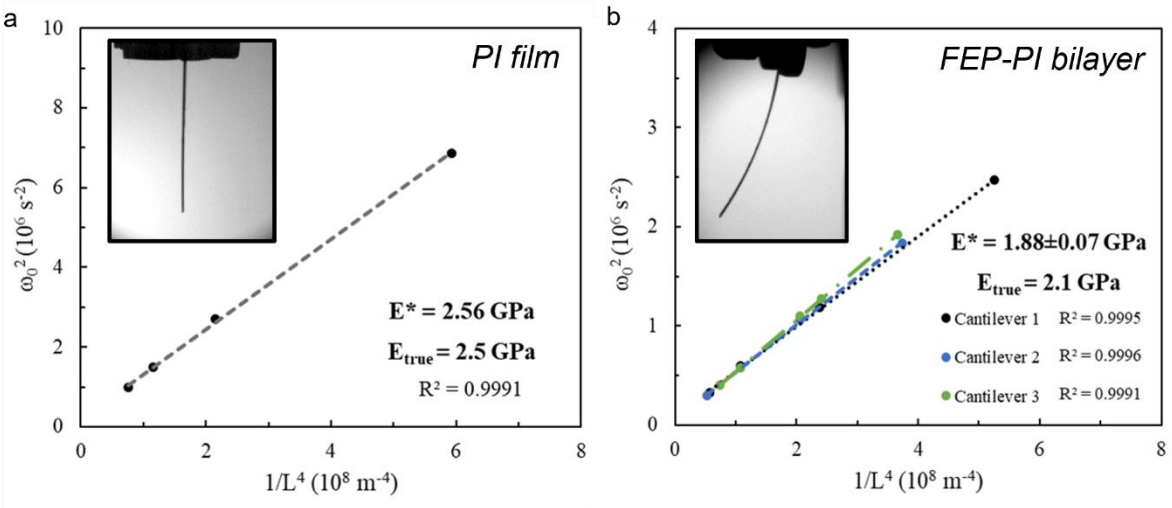

Fig. 5.7. Linear plots for the resonance frequency versus inverse length for commercial (a) Kapton PI and (b) PI-FEP bilayer films. Elastic moduli (E*) computed from the linear fits are provided. Photographs of the cantilevers are provided as insets with the fixed end at the top and free end at the bottom.

To expand this analysis to a photothermally actuated bilayer, a film was prepared by drop casting a solution of DASA and PBMA in DCM (15 mg PBMA per mL solvent) onto a 25 μm thick PI substrate. This was analogous to the bilayer preparation procedure outlined in Section 3.2.1 using PI instead of PET and increasing the DASA loading to 3 wt. % in PBMA instead of 1 wt. %. The bilayers were cut into cantilevers 10 mm long by 1 mm wide and were swept through a range of frequencies, measuring the frequency dependent amplitude and phase by the same method as outlined above for the commercial films. During photothermal actuation, the DASA-PBMA surface was uniformly irradiated at 110 mW/cm^2 with a 640 nm laser at a single vibration frequency and 2.5 s were allowed for thermal equilibration before the cantilever was subjected to a frequency sweep at 8 Hz/s. The surface temperature of the sample was recorded with an infrared camera during the initial thermal equilibration period and the subsequent frequency sweep. The results of three consecutive heating and cooling cycles are provided in Fig. 5.8.a. Between each actuation cycle, the sample was gently heated to approximately 50 °C to speed up the recovery from **C** to **A**.

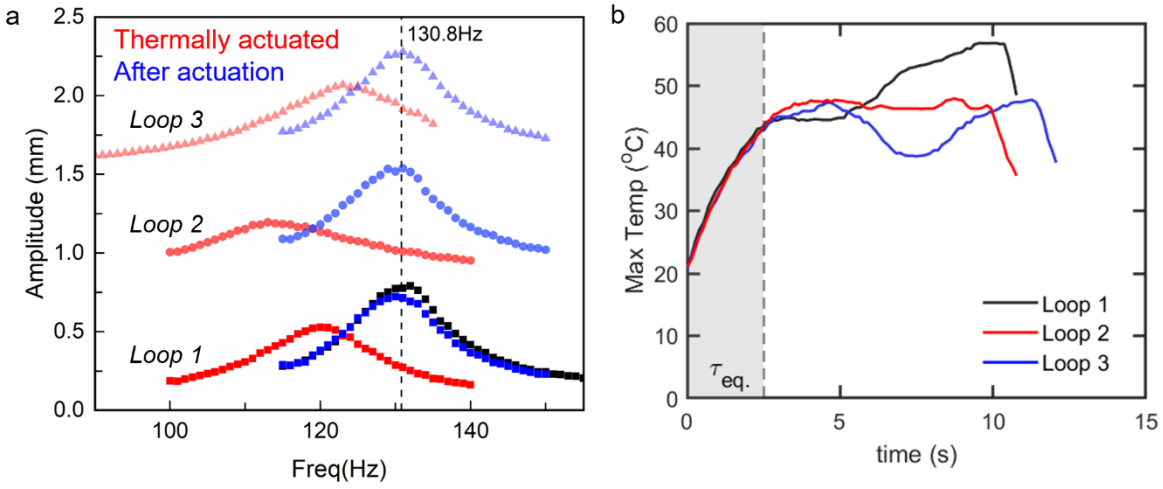

Fig. 5.8. (a) Frequency-dependent amplitude measured at the cantilever tip over three identical actuation cycles. A vertical offset is added manually to loops 2 (circles) and 3 (triangles) for the purpose of visualization. Colors indicate the frequency sweeps performed during (red) and after (blue) actuation. The frequency sweep performed before the first actuation cycle (squares) is plotted in black. (b) Surface temperature measured by IR camera during each actuation step plotted in red in (a). The shaded region corresponds to the 2.5 s thermal equilibration time.

In this experiment, photothermal heat generation was assumed to be isolated at the surface of the film because the starting transmittance at the excitation wavelength was less than 10^{-4} %. While absorption was assumed to be localized to the film surface, thermal gradients over bilayer thickness could be neglected based on an approximation of the film Biot number (Bi = 0.002-0.014). To accurately determine the temperature dependent elastic modulus by the same method that was used for the commercial PI and PI-FEP films, a uniform and constant surface temperature during the frequency sweep was required. However, the accumulation of the non-absorbing **C** isomer and the increased rate of convective heat loss as the cantilever approached resonance prevented the cantilever from maintaining a constant surface temperature over the course of the measurement. Variability in the bilayer surface temperature is clearly visible in Fig. 5.8.b, where the temperature is plotted for the same actuation cycles plotted in Fig. 5.8.a.

While the lack of a constant temperature over the measurement time scale prevented a quantitative assessment of the change in elastic modulus during actuation, all samples showed a drop in the resonance frequency and an increase in the structural damping factor upon photothermal actuation. Both observations are consistent with the effects of thermally softening the PBMA layer by heating above its T_g. Additionally, the resonance curves measured at ambient temperature before and after each actuation cycle were reproducible, indicating the sample was not experiencing plastic deformation from the forces incurred in vibration and photothermal actuation.

To address the shortcomings of this method, a new approach was developed that eliminated the need for a frequency sweep during actuation. In this technique, the actuator was subjected to an initial sweep before actuation to determine the starting resonance frequency and effective mass. Subsequently, the amplitude and phase were measured during actuation at a constant drive frequency and used to calculate the resonance frequency and

damping coefficient as a function of irradiation time using equations 5.4 and 5.5. A necessary assumption in this analysis was that the cantilever effective mass remained constant during actuation. This was likely a valid simplification because previous experiments performed with commercial FEP-PI bilayers (Fig. 5.7.b) had confirmed that the mode shape of a driven cantilever was not significantly affected by the amount of static bending deformation in the film.

This method was applied to a photothermal bilayer actuator fabricated by drop casting a solution of DASA (3 wt. %) and PMMA in DCM (13 mg PMMA per mL DCM) on a 75 μm thick Kapton substrate. In this experiment, PMMA was used in place of PBMA as the DASA host polymer to allow for more sustained and efficient photothermal heating because the higher glass transition temperature of PMMA is known result in slower DASA photoswitching (*cf.* Section 3.3). In addition, a thicker Kapton substrate was used to prevent the increased rigidity of PMMA from causing the bilayer to curl up from the interfacial stress generated during solvent evaporation. The results of this experiment are plotted in Fig. 5.9.

In panel a of Fig. 5.9, the amplitude and phase measured during the initial frequency sweep are plotted to indicate the position of the resonance frequency at room temperature. Panel b of Fig. 5.9 shows the temperature dependent amplitude and phase at a constant excitation frequency of 186 Hz (indicated with a red dashed line in Fig. 5.9.a). This frequency was selected because it was below the initial resonance frequency and the resonance frequency was expected to shift to lower frequencies during actuation based on the data plotted in Fig. 5.8. During actuation, the constant drive frequency of 186 Hz corresponded to the resonance frequency at a surface temperature of 59.5 °C. This was indicated by a maximum in the cantilever amplitude and a phase offset of 3π/2. Above this temperature, the resonance frequency shifted below 186 Hz, indicated by a decrease in the amplitude and a phase offset approaching π. This is supported by the calculated resonance frequencies and

damping coefficients plotted in panel c of Fig. 5.9. Interestingly, the resonance frequency and damping coefficients do not appear to plateau as the cantilever approaches thermal equilibrium during actuation. This behavior may have been due to a drop in the rate of convective heat loss, which occurred as the vibration amplitude decreased at higher temperatures.

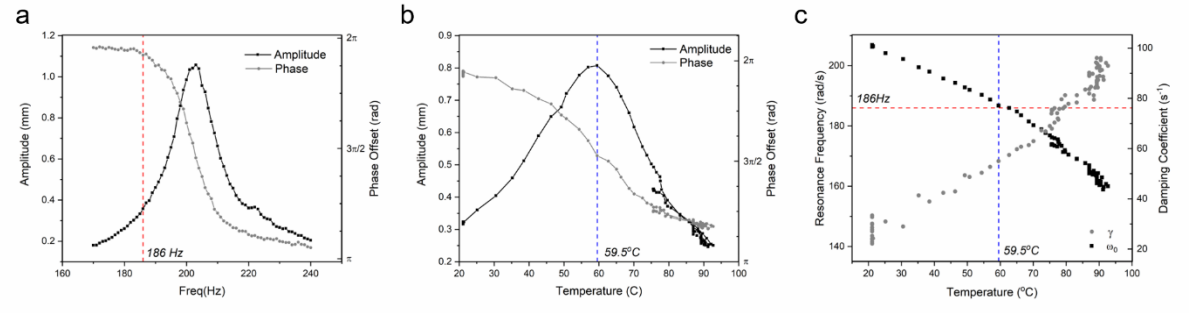

Fig. 5.9. (a) Initial frequency sweep measured before actuation. (b) Amplitude (black) and phase (grey) versus temperature measured during actuation at an excitation frequency of 186 Hz (labelled in red in (a)). (c) Resonance frequency and damping coefficient versus temperature calculated from the temperature dependent amplitude and phase in (b) and the effective mass computed from the fit in (a).

5.3.3. Conclusion

While the vibrational analysis presented here provides an interesting approach to dynamically measuring the actuation-induced changes in the elastic properties of a photothermal bilayer, this technique is minimally sensitive to the forces generated at the interface during actuation. This is because a change in resonance frequency of a polymer film does not necessarily reflect the ability of that material to perform macroscopic work. As a result, it fails to serve as a robust tool for dynamically modelling the process of photothermal bilayer bending actuation.

To redesign this technique for better capturing the dynamics of actuation, an approach similar to the one presented in White et al. would be ideal, where the forces generated during actuation are used to drive oscillation instead of relying on an externally powered vibrational exciter.[27,34] In the former example, a photochemically actuated cantilever made from a

monodomain LCE functionalized with azobenzene resonated at 28.4 Hz when continuously irradiated with a multiwavelength (457 nm, 488 nm, and 514 nm) Ar^+ laser beam. The resonance condition was a composite result of multiple factors, including the rates of trans to cis and cis to trans isomerization simultaneously occurring at the excitation wavelengths, the polarization angle of the laser relative to the alignment direction of the LCE monodomain, the mechanical properties of the LCE film, and the cantilever dynamics. Unlike static deflection analysis, which is only sensitive to the structural changes occurring during actuation (i.e. deformation), and the externally driven forced vibrational analysis described in this work, which was only sensitive to material-level changes, the vibrational analysis described by White et al. driven directly by photomechanical conversion was capable of characterizing actuation on both a structural and material scale. As a result, their technique is better equipped to inform future strategies for dynamically controlling actuation.

5.4. References

(1) Sandlass, S.; Gordon, M. J. Design and Dynamic Characterization of a Phototunable Optofluidic Lens. *Opt Express* **2024**, *32* (15), 26445. https://doi.org/10.1364/oe.527369.

(2) Zupan, M.; Ashby, M. F.; Fleck, N. A. Actuator Classification and Selection - The Development of a Database. *Adv Eng Mater* **2002**, *4* (12), 933–940. https://doi.org/10.1002/adem.200290009.

(3) Liu, C.; Zheng, Y.; Yuan, R. Y.; Jiang, Z.; Xu, J. B.; Zhao, Y. R.; Wang, X.; Li, X. W.; Xing, Y.; Wang, Q. H. Tunable Liquid Lenses: Emerging Technologies and Future Perspectives. *Laser and Photonics Reviews*. John Wiley and Sons Inc November 1, 2023. https://doi.org/10.1002/lpor.202300274.

(4) Dong, L.; Agarwal, A. K.; Beebe, D. J.; Jiang, H. Adaptive Liquid Microlenses Activated by Stimuli-Responsive Hydrogels. *Nature* **2006**, *442* (7102), 551–554. https://doi.org/10.1038/nature05024.

(5) Xu, S.; Ren, H.; Lin, Y.-J.; Jim Moharam, M. G.; Wu, S.-T.; Tabiryan, N.; Dong, L.; Agarwal, A. K.; Beebe, D. J.; Jiang, H. *Adaptive Liquid Lens Actuated by Photo-Polymer*; 2009; Vol. 17.

(6) Zeng, X.; Jiang, H. Tunable Liquid Microlens Actuated by Infrared Light-Responsive Hydrogel. *Appl Phys Lett* **2008**, *93* (15). https://doi.org/10.1063/1.2996271.

(7) Song, C.; Lan, R.; Shen, C.; Bao, J.; Huang, R.; Wang, Z.; Zhang, L.; Yu, M.; Zhu, S. Self-Adaptive Accommodative Intraocular Lens Enabled by Sunlight-Driven Highly Transparent Liquid Crystalline Polymers. *ACS Appl Polym Mater* **2022**. https://doi.org/10.1021/acsapm.2c00091.

(8) Booth, M. J.; Schwertner, M.; Wilson, T.; Nakano, M.; Kawata, Y.; Nakabayashi, M.; Miyata, S. Predictive Aberration Correction for Multilayer Optical Data Storage. *Appl Phys Lett* **2006**, *88* (3), 1–3. https://doi.org/10.1063/1.2166684.

(9) Marx, V. Microscopy: Hello, Adaptive Optics. *Nat Methods* **2017**, *14* (12), 1133–1136. https://doi.org/10.1038/nmeth.4508.

(10) Petsch, S.; Schuhladen, S.; Dreesen, L.; Zappe, H. The Engineered Eyeball, a Tunable Imaging System Using Soft-Matter Micro-Optics. *Light Sci Appl* **2016**, *5* (7). https://doi.org/10.1038/LSA.2016.68.

(11) Tokunaga, A. T. New Generation Ground-Based Optical/Infrared Telescopes. In *Encyclopedia of the Solar System*; Elsevier, 2014; pp 1089–1105. https://doi.org/10.1016/B978-0-12-415845-0.00051-7.

(12) Zeng, H.; Wani, O. M.; Wasylczyk, P.; Kaczmarek, R.; Priimagi, A. Self-Regulating Iris Based on Light-Actuated Liquid Crystal Elastomer. *Advanced Materials* **2017**, *29* (30). https://doi.org/10.1002/adma.201701814.

(13) Xu, W.; Sanchez, D. M.; Raucci, U.; Zhou, H.; Dong, X.; Hu, M.; Bardeen, C. J.; Martinez, T. J.; Hayward, R. C. Photo-Actuators via Epitaxial Growth of Microcrystal Arrays in Polymer Membranes. *Nat Mater* **2023**, *22* (9), 1152–1159. https://doi.org/10.1038/s41563-023-01610-4.

(14) Svanidze, A.; Guo, T.; Zheng, X.; Palffy-Muhoray, P. Light-Induced Stress and Work in Photomechanical Materials. *Phys Rev E* **2021**, *103* (5). https://doi.org/10.1103/PhysRevE.103.L051002.

(15) Kuenstler, A. S.; Hayward, R. C. Light-Induced Shape Morphing of Thin Films. *Current Opinion in Colloid and Interface Science*. Elsevier Ltd March 1, 2019, pp 70–86. https://doi.org/10.1016/j.cocis.2019.01.009.

(16) Qin, L.; Liu, X.; Yu, Y. Soft Actuators of Liquid Crystal Polymers Fueled by Light from Ultraviolet to Near Infrared. *Advanced Optical Materials*. John Wiley and Sons Inc April 1, 2021. https://doi.org/10.1002/adom.202001743.

(17) López-Valdeolivas, M.; Liu, D.; Broer, D. J.; Sánchez-Somolinos, C. 4D Printed Actuators with Soft-Robotic Functions. *Macromol Rapid Commun* **2018**, *39* (5). https://doi.org/10.1002/marc.201700710.

(18) Zhang, W.; Li, H.; Zou, Y. C.; Xu, F.; Li, Z. R. A Bidirectionally Focus-Tunable Optofluidic Microlens with Miniature Thermoelectric Coolers. *IEEE Photonics Technology Letters* **2023**, *35* (17), 919–922. https://doi.org/10.1109/LPT.2023.3279285.

(19) Lee, J. K.; Park, K. W.; Lim, G.; Kim, H. R.; Kong, S. H. Variable-Focus Liquid Lens Based on a Laterally-Integrated Thermopneumatic Actuator. *J Opt Soc Korea* **2012**, *16* (1), 22–28. https://doi.org/10.3807/JOSK.2012.16.1.022.

(20) Zhang, W.; Zappe, H.; Seifert, A. Wafer-Scale Fabricated Thermo-Pneumatically Tunable Microlenses. *Light Sci Appl* **2014**, *3*. https://doi.org/10.1038/lsa.2014.26.

(21) Zhang, W.; Li, H.; Zou, Y.; Zhao, P.; Li, Z. Design and Fabrication of a Tunable Optofluidic Microlens Driven by an Encircled Thermo-Pneumatic Actuator. *Micromachines (Basel)* **2022**, *13* (8). https://doi.org/10.3390/mi13081189.

(22) Zhang, W.; Aljasem, K.; Zappe, H.; Seifert, A. Completely Integrated, Thermo-Pneumatically Tunable Microlens. *Opt Express* **2011**, *19*, 2347–2362.

(23) Chen, L.; Ghilardi, M.; Busfield, J. J. C.; Carpi, F. Electrically Tunable Lenses: A Review. *Frontiers in Robotics and AI*. Frontiers Media S.A. June 9, 2021. https://doi.org/10.3389/frobt.2021.678046.

(24) Sandlass, S. Pump Actuated and Photothermal-Thermopneumatic Tunable Lens Design Files. *figshare*. 2024. https://doi.org/10.6084/m9.figshare.25569858.v2.

(25) Ren, H.; Fox, D.; Anderson, P. A.; Wu, B.; Wu, S.-T. *Tunable-Focus Liquid Lens Controlled Using a Servo Motor*; 2006.

(26) Yang, X.; Chen, Y.; Zhang, X.; Xue, P.; Lv, P.; Yang, Y.; Wang, L.; Feng, W. Bioinspired Light-Fueled Water-Walking Soft Robots Based on Liquid Crystal Network Actuators with Polymerizable Miniaturized Gold Nanorods. *Nano Today* **2022**, *43*. https://doi.org/10.1016/j.nantod.2022.101419.

(27) Serak, S.; Tabiryan, N.; Vergara, R.; White, T. J.; Vaia, R. A.; Bunning, T. J. Liquid Crystalline Polymer Cantilever Oscillators Fueled by Light. *Soft Matter* **2010**, *6* (4), 779–783. https://doi.org/10.1039/b916831a.

(28) Li, M.; Myers, E. B.; Tang, H. X.; Aldridge, S. J.; McCaig, H. C.; Whiting, J. J.; Simonson, R. J.; Lewis, N. S.; Roukes, M. L. Nanoelectromechanical Resonator Arrays for Ultrafast, Gas-Phase Chromatographic Chemical Analysis. *Nano Lett* **2010**, *10* (10), 3899–3903. https://doi.org/10.1021/nl101586s.

(29) Thundat, M. T.; Chen, G. Y.; Warmack, R. J.; Allison, D. P.; Wachter, E. A. *Vapor Detection Using Resonating*; UTC, 1995; Vol. 67. https://pubs.acs.org/sharingguidelines.

(30) Shiraishi, N.; Ikehara, T.; Dao, D. v.; Sugiyama, S.; Ando, Y. Fabrication and Testing of Polymer Cantilevers for VOC Sensors. *Sens Actuators A Phys* **2013**, *202*, 233–239. https://doi.org/10.1016/j.sna.2013.01.011.

(31) Betts, T. A.; Tipple, C. A.; Sepaniak, M. J.; Datskos, P. G. *Selectivity of Chemical Sensors Based on Micro-Cantilevers Coated with Thin Polymer Films*; 2000; Vol. 422.

(32) Tamayo, J.; Ramos, D.; Mertens, J.; Calleja, M. Effect of the Adsorbate Stiffness on the Resonance Response of Microcantilever Sensors. *Appl Phys Lett* **2006**, *89* (22). https://doi.org/10.1063/1.2388925.

(33) Finot, E.; Passian, A.; Thundat, T. Measurement of Mechanical Properties of Cantilever Shaped Materials. *Sensors* **2008**, *8* (5), 3497–3541. https://doi.org/10.3390/s8053497.

(34) White, T. J.; Tabiryan, N. V.; Serak, S. V.; Hrozhyk, U. A.; Tondiglia, V. P.; Koerner, H.; Vaia, R. A.; Bunning, T. J. A High Frequency Photodriven Polymer Oscillator. *Soft Matter* **2008**, *4* (9), 1796–1798. https://doi.org/10.1039/b805434g.

Chapter 6

Conclusion

Throughout this thesis, polymers that respond to light as a stimulus or that undergo a change in their optical properties in response to any number of other stimuli have been broadly classified as photoactive functional materials. While this terminology is in line with the definition used in the field, the label fails to acknowledge that stimuli responsive materials often are not inherently functional but are imparted with a function when incorporated into what is often a highly engineered multi-component assembly. As a result, research into these so-called photoactive functional materials cannot solely focus on developing stimuli-responsive materials without also considering the higher-level engineering required to integrate these materials into a real-world application. With this philosophy in mind, the work presented in this thesis approached the challenge of developing photoactive functional materials both from a fundamental molecular level perspective and an applied engineering perspective.

The first area of study, discussed in chapters 2, 3, and 4, was largely fundamental in nature and focused on developing new spectroscopic techniques in cooperation existing methods to better understand the unique and complex photochemistry of DASA when incorporated into different polymers. Discovered in 2014 at UCSB, DASAs are a class of organic photoswitches that are promising candidates for the future of advanced stimuli responsive polymers because they are negatively photochromic, sensitive to many different stimuli (e.g., pH, polarity, heat, mechanical stress, etc.), and isomerize between three stable or metastable photochemically distinct states. While these abilities are unmatched among the library of organic photoswitches developed to date, they are underutilized in DASA-based photoactive polymer applications because of interactions between DASA and the host polymer that affect the photoswitching energy landscape in a way that isn't well understood. To address this gap in knowledge, improved spectroscopic techniques were needed that provide the enhanced temporal resolution and sensitivity needed to measure DASA

photoswitching in polymers and in other complex structures/assemblies (colloids, vesicles, nanoreactors, etc.).

One such technique developed in the course of this thesis was called frequency modulated pump probe spectroscopy, or FMPPS, and was designed specifically to provide the sensitivity and temporal resolution needed to measure the isomerization kinetics of DASA, specifically the metastable **B/B'** isomer. In addition to improving the sensitivity and resolution of traditional UV-Vis absorption spectroscopy, the FMPPS detection scheme was highly selective towards optical signals modulated at the specific frequencies that the instrument was locked in to. As a result, signal delays arising from mechanical beam flags or shutters could be eliminated because the detector filtered out any light that was scattered or reflected by the sample from ambient light and/or the pump light used for optical excitation. Furthermore, the sensitivity of the phase locked detection scheme to the frequencies of interest permitted lower light intensities to be used for probing the sample absorbance, allowing thermal isomerizations of photochemically active molecules to be measured as passively as possible.

In chapter 2, FMPPS was introduced and used to measure the minute absorbance of **B/B'** (< 0.05 a.u.) generated during photoswitching to understand the effect of solvent polarity on PES of first, second, and third generation DASAs with different amounts of charge separation. The results of this study showed that DASAs with greater amounts of charge separation, specifically first and third generation DASAs, were more susceptible to the effects of polarity and that these effects could be accurately predicted by considering the effect of polarity on the positions of single and double bonds along the conjugated triene backbone. However, second-generation DASAs, which exhibited less charge separation along the backbone, displayed a notable polarity-driven effect in the accumulation of **B/B'** during photoswitching. This polarity sensitivity was not reflected in the rate of photoswitching for second generation DASAs, underscoring the importance of using FMPPS to measure **B/B'**

during photoswitching instead of only measuring the disappearance of **A**. At the conclusion of chapter 2, these differences in polarity sensitivity between first, second and third generation DASAs were leveraged to demonstrate the use of polarity as a non-selective stimulus for selectively controlling the absorbance of these three different DASAs when co-dissolved in toluene.

Unlike organic solvents, that vary minimally in viscosity, polymers that are based on chemically analogous repeat units can differ dramatically in their mechanical properties as a function of their temperature, molecular weight, and crosslink density. As a result, polymer-bound photoswitches are often subject to a complex interplay of polarizing interactions and mechanical confinement forces that modify the photoswitch energy landscape. Instead of distinguishing these two matrix-driven effects by controlling for one while measuring the other, a more efficient approach uses heuristic arguments to isolate the effect of mechanical confinement by approximating the effect of polarity using measurements made in chemically similar solvents.

In the specific case of DASA, the analysis provided in chapter 2 regarding the effect of polarity on the PES of DASA provided the foundation necessary to accurately interpret the results of the study described in chapter 3, which aimed to better understanding the impact of mechanical confinement on the PES of DASA in amorphous polymers. In this study, FMPPS was used to measure the isomerization kinetics of first generation DASA, specifically the **B/B'** isomer, in toluene, PBMA, and PMMA to understand why the rate of photoswitching couldn't be controlled as effectively by optically pumping **B/B'** as the rigidity of the host environment increased. In the course of this analysis, an interesting deviation from first order kinetics was observed for the thermal isomerization of **B/B'** that has also been observed in the trans-to-cis isomerization of azobenzene in glassy polymers and viscous liquids. This observation seemed to suggest that the forces arising from mechanical confinement of the photoswitch were not

uniform but instead had a local degree of heterogeneity, resulting in different kinetic regimes depending on the local environment. To further explore this result, a time resolved optical microscopy technique like Raman spectroscopy may be an interesting area to pursue for spatially mapping the **B/B'** isomerization kinetics in glassy polymers vitrified at different rates to control the local heterogeneity.

To conclude the fundamental research portion of this thesis, chapter 4 delved into the unique anisotropic optical properties of DASA and other chromophores when these molecules were incorporated into nematic-phase LCEs. In this chapter, polarized light absorbance spectroscopy was performed to assess the chromophore's degree of linear dichroism by measuring its static polarization dependent absorbance. In addition, a similar version of the technique using FMPPS was developed and used to measure the dynamic reorientation of one such chromophore (DASA) in an LCE subject to compressive stress. Both of these techniques indicated that the chromophores preferentially aligned along the LCE alignment axis, resulting in them displaying polarization dependent absorbances. This result was significant because it implied that the rate of photoswitching in these systems must depend on the polarization angle of the light used to excite the transition. With photoactuation being the primary application for these chromophore-functionalized LCEs, polarization-dependent photoisomerization and photothermal conversion efficiencies will likely have a significant impact on the light to work conversion efficiency and additional studies are needed to quantify the significance of this effect.

The application-focused portion of this study was explored in chapter 5 of this thesis and related to the application of photoactive materials in soft photoactuation. Unlike other common energy sources for soft actuators, which are primarily pneumatic and electrostatic, energy from light does not exert a direct force when interacting with matter. As a result, designing materials that efficiently convert light energy into work with high spatial fidelity

remains a significant challenge, despite unique opportunities afforded by using light to power actuation, including the ability to spatially program light down to the diffraction limit for unmatched control over actuator shape. However, this does not necessarily imply that the drawbacks associated with photoactuation exceed the possible advantages of this technology but instead underscores the importance of rational design to target applications that are best suited to actuation using light.

Chapter 5 outlines the design and characterization of two different but complementary applications, the first being a photothermally actuated fluid lens and the second being a DASA-based photothermally actuated bilayer cantilever. In the former example, thermodynamically and mechanically informed design principles were applied to overcome the efficiency cost associated with photoactuation by limiting the power consumption of the fluid lens (8.2 μJ) required to change the focal length by 27 %. This technology has the potential to revolutionize the field of optical engineering by allowing individual lenses in an array to be controlled independently using light but requires lowering the mechano-optical advantage to allow closer packing of the lenses. This could potentially be achieved by using a photoactuated LCE as the lens medium instead of a fluid but requires more advanced LCE alignment techniques than currently exist.

In the latter example of photothermal actuation described in chapter 5, forced vibrational analysis was used to measure the change in the mechanical properties of a bilayer cantilever during photothermal actuation. In this example, thermal softening of the DASA functionalized PHMA photothermal layer resulted in a 10-40 Hz drop in the resonance frequency and an increase in the structural damping factor under irradiation. However, these observations only related changes occurred on a material scale and did not necessarily reflect the stresses generated on a structural level during actuation. To redesign this technique for capturing the dynamics of actuation, the conversion of light to work should be used directly to

drive oscillation of the cantilever instead of relying on an externally powered vibrational exciter. In practice, however, this alternative approach has only been successfully demonstrated using an azobenzene-functionalized monodomain LCE.[*]

[**] This work was published by Timothy Bunning's group at the Air Force Research Academy: White, T.; et al., *Soft Matter* **4**, 1796-1798. (2008), Serak, S.; et al., *Soft Matter* **6**, 779-783. (2010)